UNIVERSITY OF CALIFORNIA
RIVERSIDE

Astrophysics and Cosmology with Spectroscopic and Photometric Intensity Mapping

A Dissertation submitted in partial satisfaction
of the requirements for the degree of

Doctor of Philosophy

in

Physics

by

Bryan Richard Scott

September 2022

Dissertation Committee:

Dr. Simeon Bird, Chairperson
Dr. Anson D'Aloisio
Dr. Brian Siana

The Dissertation of Bryan Richard Scott is approved:

Committee Chairperson

University of California, Riverside

Acknowledgments

I am deeply grateful to my advisor, Simeon Bird, for his trust, support, mentorship, and the freedom he gave me to chart my own course at every step. Working with Simeon has made me a better person and a better scientist.

I am also grateful for the mentorship of Brian Siana and Flip Tanedo, who helped me figure out what is important in life and career, how to advocate for others, and how to give back to my community.

I would like to especially recognize the contributions of Anson D'Aloisio, Naveen Reddy, and James Flegal. Dr D'Aloisio has served on my candidacy and dissertation committees, providing invaluable feedback on my work at these crucial milestones. I am thankful for helpful comments during my candidacy exam from Dr Reddy and Dr Flegal.

The teaching and mentorship of undergraduates has been among my most meaningful experiences at UCR. I am extraordinarily grateful for the mentorship of Hillary Jenks and Michael Anderson, whose invaluable guidance has made me a better teacher.

My success would not have been possible without the support and inspiration of so many UCR graduate students and postdocs. I am thankful for many late night conversations with Jeremy Alexander. Fellow graduate students, Jessica Doppel, AJ Bassill, Garett Lopez, Amanda Pagul, and Liz Finney have helped me to grow as a scholar and as a person. I would not have succeeded without the guidance and support of Tara Fetherolf. Christina Manzano-King's tireless commitment to making our world just and equitable challenged me to think more deeply and critically about what is important and about the impact that I want to have on the world. I could not have asked for a kinder, smarter, or more supportive

first year cohort, Daniel Hogue, Ethan Jahn, Jarred Gillette, Stephen Hannon, and Ian McConachie, I am so excited to see what you achieve!

My fellow students in Dr Bird's group, Ming-Feng Ho, Mahdi Qezlou, Reza Monadi, Martin Fernandez, and postdoc Phoebe Upton-Sanderbeck inspire me everyday with their cleverness and kindness. I am immensely grateful for the friendship of Nicholas Manganelli, after meeting during the prospective student visit day, he has supported and encouraged me through every twist, curve, and inversion of this wild ride.

Finally, words can not express my gratitude for my family's love, kindness, and warmth. My father is and will always be my role model, for his kindness, his commitment, and for the sacrifices he has made so that I could succeed.

The text of this dissertation, in part (Chapter 3) is a reprint of the material as it appears in the Monthly Notices of the Royal Astronomical Society (April 2022). The co-author, Simeon Bird, listed in that publication directed and supervised the research which forms the basis for this part of the dissertation. Phoebe Upton-Sanderbeck contributed expertise in the theory of diffuse extragalactic emission and interpretation of our results.

This dissertation also contains a draft of an article (Chapter 4) that will be submitted for publication by Oxford University Press in the Monthly Notices of the Royal Astronomical Society. The co-authors, Simeon Bird and Kirit Karkare, will be listed in that publication. They directed and supervised the research which forms the basis for this part of the dissertation. The results of this chapter are preliminary and the published version should take precedence over the work as presented and described here.

To my Mother. I miss you everyday.

To my Brother and Father, for their love and support.

ABSTRACT OF THE DISSERTATION

Astrophysics and Cosmology with Spectroscopic and Photometric Intensity Mapping

by

Bryan Richard Scott

Doctor of Philosophy, Graduate Program in Physics
University of California, Riverside, September 2022
Dr. Simeon Bird, Chairperson

Spectroscopic and photometric intensity mapping are emerging techniques for observing large cosmological volumes with a high frequency but low spatial resolution survey. We apply this technique to study large scale structure as both a tool for inference and for constraining theories of gravity. In particular, we make forecasts for the performance of future all-sky UV experiments with a technique that extracts the redshift distribution of UV-optical background photon emission. We consider the Cosmological Advanced Survey Telescope for Optical-UV Research (CASTOR) and the Spectro-Photometer for the History of the Universe, Epoch of Reionization, and Ices Explorer (SPHEREx). We show that under reasonable error models, CASTOR measures the UV background SED 2-10 times better than existing data.

We then study the detectability of deviations from General Relativity through mm-wave spectroscopic line intensity mapping of galaxies that trace large scale structure. We specifically consider measurements of the matter power spectrum and redshift space distortion multipole moments including the effects of foregrounds and emission from inter-

loping lines. In the context of Horndeski theories, we calculate the sensitivity that future experiments would need in order to produce constraints on linear theory parameters that are comparable to or better than the best existing constraints from galaxy surveys and the Cosmic Microwave Background.

Contents

List of Figures

List of Tables

Chapter 1

Introduction

Cosmology, derived from the Greek *kosmos*, is the study of order in the universe[1]. It is poetic, then, that contemporary observational cosmology is mainly concerned with techniques for turning the positions of galaxies, and the structures they form, into insight into fundamental physics and the history of the universe. This dissertation has two main goals related to the study of correlations in the universe, leading to two sets of new results, presented in Chapters 3 and 4. In the first case, it will be shown that knowledge of large scale structure can be used to achieve order of magnitude improvements in our understanding of astrophysics over cosmic time. In the second case, we will study the feasibility of measuring large scale structure and our ability to turn those measurements into an understanding of gravity beyond Einstein's theory. As this thesis covers a diverse set of physical phenomena while applying a new set of experimental methodologies, we begin with an introduction to astrophysics and cosmology in the era of intensity mapping and large surveys.

[1]The word Cosmology was likely coined by the philosopher Christian Wolff in the title of a 1731 book, *Cosmologia Generalis*. [5]

Chapter 1 reviews intensity mapping and differences between the photometric and spectroscopic (or line) intensity mapping cases, concluding with a brief review of current and future analysis methods. Chapter 2 presents the scientific background for the later chapters, in particular introducing the observational and theoretical status of the extra-galactic background light (EBL) across the electromagnetic spectrum. Finally, the latter half of Chapter 2 introduces the current status of contemporary cosmology, the theory of large scale structure, and current puzzles surrounding the existence of dark energy and the need for modifications to Einstein Gravity. Chapter 3 then presents a forecast of EBL measurements with the Cosmological Advanced Survey Telescope for Optical-UV Research (CASTOR), while Chapter 4 forecasts Large Scale Structure constraints on the linear theory parameters of Horndeski Gravity theories. Finally, Chapter 5 concludes this dissertation with a survey of future measurement and analysis strategies.

1.1 What is Intensity Mapping?

Intensity Mapping (IM) is a technique for measuring the integrated emission of stars and galaxies over cosmic time [6]. The distinguishing features of this technique can best be understood through comparison to a traditional galaxy survey. In a galaxy survey, a telescope observes for a long period of time to produce deep images that are then thresholded. Pixels with counts above some level, relative to some estimate of the background noise, are labelled as significant (and interpreted as belonging to a star or galaxy), while pixels below the thresholded are disregarded. Intensity Mapping experiments do away with the requirement to "detect" individual sources and instead simply catalog every photon on

the sky. Rather than a catalog of detected sources, the fundamental data products of an IM experiment are continuous maps over the sky.

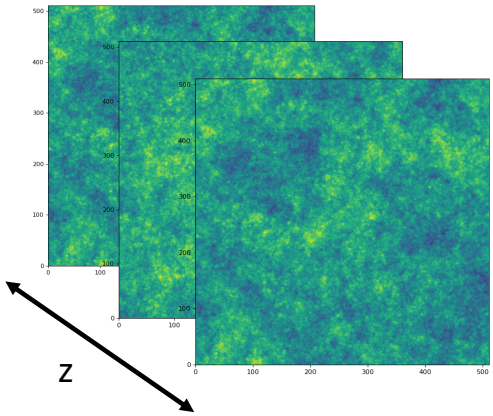

Figure 1.1: Visual depiction of the Line Intensity Mapping data products. 2D slices the full 3D volume with each slice labelled by its measured redshift. Fluctuations in the distribution of numerous discrete astrophysical are observed as continuous temperature fluctuations on the sky.The number of slices in a cosmological volume is a function of the frequency resolution of the instrument, and places a limit on the statistical information that can be extracted from the map.

Intensity Mapping experiments can be divided into two categories. In a photometric intensity mapping experiment, a telescope scans the sky through a set of discrete filters, producing continuous measurements of photometric magnitudes, recorded in angular coordinates. A significant challenge is to turn these band averaged angular measurements into 3D resolved information by adding a distance measure for the photons detected in any given pixel of the map. By contrast, Spectroscopic or Line Intensity Mapping (LIM), produces frequency resolved maps that target specific emission features. Frequency resolved maps can be straightforwardly turned into a full 3D map of the emitting structures via the relation $\nu_{obs} = (1 + z)\nu_{rest}$.

Table 1.1: Table of current and near future sub-mm LIM experiments.

Experiment	Target Lines	Redshifts	Bandwidth	Aperature
COMAP I & II	CO(1-0), CO(2-1)	2.4-3.4, 6-8	26-34 GHz	10.4 m
COMAP III	CO(1-0), CO(2-1)	5.8-7.9, 2.4-3.4, 6-8	13-17 GHz, 26-34 GHz	10.4 m
Fred Young/CCAT-Prime	[CII]	6-8	210-275 GHz	6 m
TIME	[CII]	5-9	199-305 GHz	10.4 m
CONCERTO	[CII]	5-8	125-310 GHz	12 m
YTLA	CO	1.2-3	86-102 GHz	Interferometer
mmIME	CO, [CII]	0.2-6	30, 90, 300 GHz	Multiple
SPT-SLIM	CO	0.5-2	120-180 GHz	10 m
Evolved Future LIM*	CO	0.3-3	75-300 GHz	$\sim$10 m

One key advantage of LIM, as compared to galaxy surveys, is that they quickly survey large cosmological volumes and therefore allow for very large scales to be measured. Further, the survey depth is no longer a function of detection threshold but is instead driven by instrumental bandwidth [7]. As a consequence, emission lines are measured over a very wide range in redshift, which allows for detailed studies of the redshift evolution of both stellar/galactic astrophysics and large scale structure. The combination of large survey volumes and deep redshift coverage makes LIM a uniquely powerful tool for both astrophysics and cosmology [6], [8], [9], [10], [11]. Table 1.1 lists current and near future IM experiments.

The Future LIM experiment is speculative and represents the experiment we consider in detail in Chapter 4. In this section, we discuss results from photometric intensity mapping experiments and introduce the spectroscopic intensity mapping formalism. We conclude with a brief discussion of analysis methods and potential challenges for future experiments.

1.2 Photometric Intensity Mapping

Despite the long history of low surface brightness and diffuse sky measurements [12], the association of these measurements with the notion of "intensity mapping" is a recent development, arising primarily in comparison with spectroscopic or line intensity mapping. The concept is a straightforward one: observe the sky in some set of discrete but finite filters chosen to target specific emission features at a given target redshift. Paradigmatic examples of recent and contemporary photometric intensity mapping experiments are the Cosmic Microwave Background satellites; *Cosmic Background Explorer* (COBE), *Wilkinson Microwave Anisotropy Probe* (WMAP), and the *Planck* spacecraft. Although the primary data products of these experiments are all sky temperature maps of the Cosmic Microwave Background, a wealth of information about the the low redshift Comic Infrared Background (CIB) is also obtained as significant CMB foreground.

The first detections of the CIB come from the FIRAS and DIRBE instruments on the COBE spacecraft [13]. Follow-up observations of the CIB were made with the IRAS mission and the *Spitzer* space telescope, both of which produced infrared intensity/temperature maps [14, 15]. Over the last decade, the *Planck* High Frequency Instrument (HFI) has become an instrument of choice for measuring both the average brightness of the CIB (the "monopole"), and for detecting anisotropies in the CIB that can be connected to large scale structure. *Planck* HFI measurements of the CIB are a demonstrative example of the challenges and methods used in photometric IM, both at the mapmaking and analysis/inference to astrophysics and cosmology levels [16] The band-averaged magnitude of the CIB (or extragalactic background light, total source + diffuse map at any wavelength) is

given by,

$$I_\nu(\nu_0) = \int \frac{d\nu}{\nu_0} R(\nu) j_\nu \tag{1.1}$$

which is the band averaged specific intensity at an observed frame frequency ν_0. We can contrast this expression with the expressions given in Chapter 3 in terms of specific models for the UV-optical EBL. R represents the filter response function, and the width of the filter response function relative to the shape of the function j_ν can be used to distinguish the spectroscopic and photometric IM cases. In a photometric experiment, the width of R $>> j_\nu$, making the frequency response of the band-averaged quantity smoothed in observed frame frequency, or equivalently, in apparent redshift space.

In this sense, SPHEREx (Spectro-Photometer for the History of the Universe, Epoch of Reionization, and Ices Explorer) All Sky Spectral Survey represents a middle ground between photometric and spectroscopic IM experiments. SPHEREx uses a linear variable filter which scans the instrument across the sky to observe each field with an instrument whose response varies in frequency [17]. Rather than a photometric experiment with a small number of broadband filters, or a spectroscopic experiment with a nearly delta function like instrumental response, SPHEREx can be approximated as consisting of 96 gaussian narrowband filters. Performance for redshift estimation of sources therefore lies somewhere between that of a broadband experiment, where only "drop-out" techniques are typically used to yield uncertain redshift estimates, and a true spectroscopic experiment where the emission redshift is known up to the instrument resolution, and usually approximated as a delta function in redshift space. This makes SPHEREx an attractive target for

improved redshift estimation techniques based on clustering with large scale structure, a concept that has been explored in [18], and in the context of the high redshift UV-optical EBL, in Chapter 3.

While SPHEREx can observe the UV-optical EBL at high redshift, observations at lower redshift require a near-UV (NUV) or far-UV (FUV) instrument, like those on the Galaxy Evolution Explorer (GALEX) and the uv, u, and g filters on the proposed Cosmological Advanced Survey Telescope for Optical UV Research (CASTOR). GALEX produced NUV and FUV intensity maps over much of the sky [1]. While primarily envisioned as a traditional survey satellite targeting the optical and near-uv, filling in a gap in the filter coverage of large ground based surveys such as the *Legacy Survey of Space and Time/Vera C. Rubin Observatory* and space-based *Euclid* and *Nancy Grace Roman* infrared surveys, CASTOR operating in an intensity mapping mode can extend existing constraints from GALEX intensity mapping to $z \sim 3$.

From the band averaged quantities, connections to astrophysics and cosmology are made through the power spectrum. While in a line intensity mapping experiment, it is conventional to work in the full 3D averaged real or Fourier space, results for photometric experiments are typically expressed in terms of the angular auto- or cross- power spectra. Formal introductions to the foundations of the correlation function and power spectra formalism is included in [19], [20], and [21]. [22] provides expressions for auto- and cross-power with a galaxy survey. This formalism can be contrasted with the phenomenological approach we take in Chapter 3, but provides a model for forecasts of photometric map - galaxy survey cross observables expressed in angular coordinates.

$$C_l = \int dz \frac{H(z)}{c} \frac{1}{\Delta z^2 \chi^2(z)} b^2(z) P_m(k,z) \frac{dI_\nu}{dz} \tag{1.2}$$

where C_l is the angular power spectrum of the field, H(z) is the Hubble rate at redshift z, c is the speed of light, $\chi(z)$ is the comoving distance, b is the map bias, $P_m(k,z)$ is the matter power spectrum, and $\frac{dI_\nu}{dz}$ is the intensity redshift distribution. $\Delta(z)$ is the redshift distribution of the galaxy catalog. Under the assumption of Gaussianity, which is known to hold on large scales, uncertainties in estimates of the angular power spectrum include contributions from Poisson or "shot noise", and instrumental systematics. On smaller scales, one can include nonlinear correction terms including the bi and tri-spectrum [7]. Equation 1.2 easily generalizes to the cross spectrum by replacing factors of the map bias. Information about the full posterior of the redshift distribution can be obtained by replacing Δz with, for example, the full posterior of a photometric redshift PDF.

1.3 Line Intensity Mapping

Line Intensity Mapping produces a full spectroscopic map of the sky by targeting individual emission lines and observing at a range of frequencies. A wide range of lines are being considered for current and near future experiments. These are summarized in table 1.2. A major target for LIM experiments is the 21 cm spin flip transition of neutral hydrogen, which is a powerful probe of reionization and the cosmic dark ages. For a thorough review of the state of 21 cm LIM, see [23].

In Chapter 4, we forecast for an experiment targeting the rotational CO ladder over the redshift range $\approx 0 - 3$ and focus the discussion here accordingly . While the

Table 1.2: Table of target emission lines and observable wavelengths.

Line	Wavelengths	"Band"	Comments
HI	50 - 350 MHz	cm	21 cm spin flip transition
Lyα	$\sim$350-550 nm	Optical	
OIII	350-2500 nm	Optical/Near-IR	Doublet
Hα	$\sim$500-3000 nm	Optical/Near-IR	
Hβ	$\sim$500-3000 nm	Optical/Near-IR	
CII	$\sim$200-1000 μm	far-IR	
OI	$\sim$100-1000 μm	far-IR	145 μm line
OIII	100-500 μm	far-IR	188 μm line
OI	100-500 μm	far-IR	63 μm line
OIII	50-300 μm	far-IR	52 μm line
NIII	50-300 μm	far-IR	58 μm line
NII	120-800 μm	far-IR	122 μm line
CO(J $\rightarrow$ J-1)	0.1 - 10 μm	far-IR/mm	Rotation Ladder from J=1-7

formalism for 21 cm experiments is similar, differences in expected systematic uncertainties and the underlying physics of line emission motivate new analysis methods for sub-mm LIM experiments targeting CO transitions.

CO is a major target for LIM experiments because it is a bright transition over a large range in redshift and is thought to probe the interstellar medium in galaxies [24]. CO line intensities are a strong function of local star formation rate, which allows LIM experiments to place tight constraints on the cosmic star formation history at low and intermediate redshift [25] and the source of ionizing photons during the epoch of reionization [26]. From a CO intensity map, statistical information about large scale structure is extracted in the form of the observed line power spectra, $\mathrm{P}_{obs}(k)$,

$$P_{obs}(k) = (b(z)I(z)\,)^2 P_m(k)^2 + P_{shot} + P_n \tag{1.3}$$

where b(z) is the map bias at redshift z, $I(z)$ is the (average) line intensity at that red-

Table 1.3: Leading order noise terms in LIM experiments, origin, and mitigation strategies.

Noise	Origin	Mitigation/comments
1/f (kolgomorov)	atmospheric fluctuations above the instrument	measurements of atmospheric lines low frequency and large scale
galactic continuum	thermal dust emission in the milky way	low order polynomial fitting to observed temperature fluctuations
cosmic variance	finite volume of real surveys	ultimate limit on any finite survey
small scale smoothing	finite angular resolution finite spectral resolution of telescope/instrument	small scale limit on resolved structures
shot noise	poisson sampling of the LSS distribution variance of the luminosity function	diagonal of the covariance matrix
line decorrelation	correlated emission within halos	arises because line emission in halos is correlated
interloper emission	emission from lines that appear to be at the same redshift	geometric tests, cross-correlations, deep learning, sparse matrix reconstruction

shift, P_{shot} is a scale independent term arising from the non-zero variance of the luminosity distribution, and P_n is a scale independent white noise term due to instrumental or atmospheric noise. The average line intensity $I(z)$ is computed from the first moment of the line luminosity function $\Phi(L, z)$, itself a function of underlying star formation rate,

$$\langle I(z) \rangle = \int_0^\infty L\Phi(L, z) dL. \tag{1.4}$$

Measurements of the line statistics, including the power spectrum, therefore probe degenerate combinations of cosmology dependent terms (bias factors, reflecting structure formation history, and the matter power spectrum), and astrophysics dependent terms encoded by the average line intensities [6]. The line power spectrum is also only measured as a noisy realization of the underlying matter power spectrum, subject to both frequency independent and dependent noise sources, the latter of which is translated into k-dependent noise during map construction. In addition to the Large Scale Structure fluctuations, this signal also includes the effect of contamination by galactic thermal dust. Table 1.3 lists this and other leading order noise terms in LIM experiments. See Chapter 4 for a more

thorough discussion of each noise term and mitigation strategies.

There is a now an active community producing forecasts and interpreting early results from this early generation of line intensity mapping experiments. Some notable recent results include the first tentative measurement of clustering power by the CO Mapping Array Project (COMAP) as well as forecasts for the Tomographic Ionized-carbon Mapping Experiment (TIME) and the CarbON CII line in post-rEionisation and ReionisaTiOn epoch (CONCERTO) experiment. One of the earliest measurements of the clustering component of the power spectrum based on COMAP measurements is presented in [27]. Their estimate of the CO clustering power $P_{CO}(k) = 2.7 \pm 1.7 \times 10^4\ \mu K^2\ \mathrm{Mpc}^3$ for $k \approx 0.051 - 0.62\ \mathrm{Mpc}^{-1}$ at z=2.4-3.4 [28] and is used to update forecasts for the full COMAP survey in [29] and for the future COMAP Epoch of Reionization (EOR) experiment in [26]. In addition to these promising early results, detailed forecasts for a range of astrophysical observables related to star formation and reionization, as well as auto and cross power spectra have been completed for TIME in [30] based on parameterized astrophysics. Simulated maps based on semi-analytic models have been used to produce similar forecasts for CONCERTO in [31].

1.4 Analysis Methods

While sophisticated analysis frameworks for large galaxy surveys and CMB experiments have been developed to enable scientific inference, analysis methods for LIM experiments remain in their infancy and depend on strong modeling assumptions. Although higher-order statistics are of long term interest for studying small scale structure and primordial non-Gaussianity, most existing analyses and forecasts restrict themselves to

considering the 1- and 2-point statistics of the map.

In particular, the 1-point voxel intensity distribution has been extensively studied for constraining the line luminosity functions. These P(D) or VID analyses are intended to help break degeneracies in analysis of the 2-pt function, where identical power spectra can be obtained for very different redshift dependent luminosity functions [6], [32]. The key to breaking the degeneracies that complicate analysis of the 2-pt function is accurate distance information that allows the line intensity to be localized to the 3D voxels rather than 2D pixels in the sky. VID and P(D) methods have been widely adopted for LIM forecasts, for example [33] applies a generalized VID "cross spectrum" in the context of 21 cm measurements, [34] forecasts CO VIDs for COMAP, [35] considers joint analysis of VIDs between CO and Lyα surveys, and [36] forecasts cosmological constraints on neutrino decays from the VID.

Equation 1.3 is only valid on intermediate and large scales in real space (see section 2.2.4for a discussion of redshift space correlations). Including information from smaller scales, the 1-halo and shot noise terms, as well as accounting for effect of making measurements in redshift space, allows for the individual terms in the degenerate combination $(b(z)I(z))^2 P_m(k)$ to be individually constrained [7] by taking ratios of auto- and cross-power, for example, with the CMB or a galaxy tracer survey. To make this concrete, consider the ratio of the 2-halo auto and cross-power with a galaxy survey. This measures the ratio

$$\frac{P_{IM,IM}}{P_{IM\times g}} = \frac{(bI)^2 P(k)}{bIb_g P(k)} \tag{1.5}$$

that constrains the quantity $\frac{bI}{b_g}$ and breaks the degeneracy between astrophysics and cos-

mology present in the LIM map, assuming the galaxy bias b_g can be modeled or measured. Then the 2-halo term can be used to estimate P(k), while the ratio of the full shape auto and cross power in redshift space can then be used to estimate the product of structure growth and the amplitude normalization of the power spectra, $f\sigma_8$. Because the observed power spectrum is a sum over the shot noise, 1-halo, and 2-halo terms, and making use of real and redshift space information requires a noisy reconstruction of the density field from redshift space measurements, the feasibility of reliably measuring the auto and cross power simultaneously is an open question that depends on modeling assumptions and the development of new analysis techniques. An analysis strategy using the information from all scales, including redshift space distortions, is presented in [7]. A feed-feed pseudo cross spectrum analysis is used for the tentative clustering signal detection in [27]. This involves constructing an estimator of the clustering power based on a split data set and including information about the noise in the map.

Breaking degeneracies between astrophysics and cosmology requires the use of internal or external LIM cross correlations, a prospect that is complicated by the existence of frequency dependent foregrounds and other systematics in both LIM experiments and auxiliary galaxy surveys. Thermal radiation from dust in the milky way, for example, adds broad continuum noise across the wavelengths targeted in sub-mm LIM [37]. Although thermal dust emission can be bright compared to the high redshift target emission lines, the smoothly varying continuum spectra can be fit by a low order polynomial and removed. At the level of current analyses techniques, the effect on the power spectra at observable scales is limited. A similar source of noise is due to incoherent temperature fluctuations

of the atmosphere. This 1/f or Kolgomorov noise term affects the largest accessible noise scales. As these noise terms primarily effect the largest scales, their impact on LIM recovery of the auto-power is expected to be small (see Chapter 4). Their impact on the LIM-CMB cross-power may be larger, as the most constraining CMB modes are at scales impacted by low-l foregrounds in both CMB and LIM temperature measurements.

Of more concern for current experiments and those targeting intermediate scales are the presence of bright interloper emission [38], [39]. An experiment targeting an emission line at fixed frequency will observe both the target line at a given target redshift as well as additional lines at a range of other distances that are redshifted to overlap with the target line. The emission at the observed frequency is then a superposition of the emission that one hoped to constrain, say because it probes the star formation rate at a given redshift, as well as an unknown contribution from potentially many interloping lines. Several mitigation strategies have been studied, including,

1. *Bright voxel masking* - A simple and common strategy is simply to mask out the brightest voxels in the map. Because a bright voxel is likely produced by massive galaxies, and structure formation implies that the most massive galaxies are at low redshift, this can effectively mask out many low redshift interlopers leaving only the high redshift target emission. Cf. [30]

2. *Targeted masking* - A slightly improved version of the bright voxel masking technique is to develop catalogs of likely interloping sources at low redshift [40]. These sources are then followed up with high resolution spectroscopy to confirm the redshift. Identification of targets is based on synergistic sub-mm observations, for example with

ALMA, or based on scaling relations between optical lines that are observable with multi-object spectrographs and interloper lines. Scatter in these scaling relationships complicates inference. Both bright voxel and targeted masking techniques also introduce selection effects into the interpretation of LIM experiments.

3. *Anisotropic Map Distortions* - This class of techniques depends on an incorrect mapping between distances and angles if the underlying cosmology or emission redshift is incorrect [38]. A significant advantage of this approach is that it does not depend on any assumption about the emission lines, their correlation with the matter distribution, or their redshift evolution. We discuss this technique further in Chapter 4.

4. *Map-level techniques* - Map level techniques have recently begun to attract more attention. Some map techniques are based on deep learning approaches, while others depend on strong assumptions about the distribution of sources and the line intensities. These assumptions act, essentially, as an informal prior on the deconfusion algorithm. As a particular example, the technique of [22] attempts to invert a sparse matrix problem defined by $I(\nu_i) = \Sigma_{j=1}^{N} \tilde{A}_{ij} N(z_j) + n_i$. Because the line intensity is primarily due to sources at a small number of redshifts, $A_{ij]}$ is a sparse matrix and the inverse problem is well posed. Sparsity, however, depends on the interloper emission being well confined to a small number of voxels.

5. *Cross Correlations* - Cross correlations, both between LIM experiments and auxiliary surveys are expected to be a key technique in the analysis of intensity maps. A thorough overview of cross-correlations in the multi-line case, including small scale

physics, is found in [41]. Although subject to the already mentioned degeneracies, these external cross correlations can produce measurements that are free of systematics not shared in a correlated fashion between multiple experiments. Additionally, as LIM experiments with larger bandwidths are considered and fielded, this has opened up the possibility of internal cross correlations. For example, current and future experiments will observe multiple rotational transitions of CO at a range of redshifts. By cross correlating each CO line and assuming that the matter power spectra is independently known, ratios of the cross correlations yield direct constraints on the mean line intensities that are free of interloper contamination.

Following confirmed detections of LIM shot and clustering power, high SNR detections of each with future experiments will likely make use of all of the above strategies. Rather than inferring only the line power for a given target emission feature and redshift, such future experiments will instead jointly infer the line intensity distributions across all observed lines and redshifts. Estimates of the matter power spectrum will then be based on an analysis that fully marginalizes over the line emission distributions for all of the observed targets. As mentioned above, development of simulation, measurement, and analysis strategies remains in its infancy, and the exact methods used in future astrophysics and cosmology results are likely to evolve significantly from the simplified methods discussed above.

Chapter 2

Scientific Background

One theme of this dissertation is that knowledge of large scale structure can be used both to enable measurements of redshift dependent astrophysics and as a powerful source of information about cosmology and fundamental physics. In this Chapter, we introduce the scientific questions that motivate both applications of intensity mapping to Large Scale Structure that are presented in Chapters 3 and 4. We begin with the extragalactic background light in Chapter 2.1.1, reviewing the EBL across the spectrum in 2.1.2, the theory of the UV-optical EBL in 2.2.2, and review observational techniques in 2.1.3. This concludes by introducing Broadband Tomography as a state of the art technique for UV EBL measurement. Then, in the latter part of the Chapter, we discuss the status of Einstein Gravity. The theory and its assumptions are detailed in 2.2.1, the formalism of contemporary cosmology in 2.2.2, and the theory and observation of Large Scale Structure in 2.2.3 and 2.2.4, respectively. Finally, we introduce reasons for suspecting the Einstein Gravity is incomplete in 2.2.5.

2.1 Extragalactic Background Light

It is somewhat of a surprise that the concept of an Extragalactic Background Light, or mean surface brightness of the sky, has a physical meaning and in fact plays an important role in both understanding the history of galaxies and in the physics of the intergalactic medium (IGM) [12]. The deep significance of the EBL is found in the near homogeneity and isotropy of the universe that makes it possible to sum over all systems and structures in redshift to produce meaningful integrated quantities. The measurement of the average EBL brightness represents a contemporary response to one of the first puzzles in modern astronomy - Olbers' paradox[1] - which asks why we observe a dark night sky in a universe of emitting stellar populations that should sum to produce an infinite brightness. While the finite age of stellar populations solves the apparent paradox, the remaining question of how bright the universe is and, in turn, how those populations have evolved, remains open. In the UV, this background sets the ionization state of the IGM and, because it depends on integrated stellar formation histories, acts as a direct probe of structure formation and the cosmic star formation history. Comparing theoretical predictions to the observed total inventory of EBL photons serves as an important consistency test for models of photon production in stars and galaxies in the universe. A discrepancy between the two could be an indication of new physics.

[1] Olbers' paradox may be the oldest puzzle in modern cosmology. It is not in fact due to Olbers, who thought it was strong evidence for a finite cosmos, but rather most probably originates with Johannes Kepler's 1610 argument for a finite universe. Writing in 1823, Olbers probably learned of it from an earlier 1720 paper by Edmund Halley that argued to the contrary that the universe is infinite in spatial extent. Eighteenth and nineteenth century solutions took many forms that prefigure contemporary ideas in cosmology, including speculation about interstellar/intergalactic absorption, non-trivial topologies, and modified gravity theories. A fascinating history of these accounts and their connection to the then new sciences of spectroscopy and thermodynamics is found in [5]

This section begins with a review of cosmic backgrounds across the electromagnetic spectrum. As the new results of this dissertation are confined to future measurements of the UV-optical background, the theory of the UV-optical background will then be presented before a short review of UV-optical background observations is presented in the final subsection.

2.1.1 Cosmic Backgrounds Across the Spectrum

The EBL extends from the γ-ray to the radio and contains a wealth of information about both astrophysics and cosmology. Measurements at the highest energies constrain the physics of compact objects and may probe the physics of dark matter interactions. Lower energy measurements reveal the history of star and galaxy formation as integrated over the populations of galaxies and active galactic nuclei. Finally, the Cosmic Microwave Background places strong constraints on cosmology and the physics of the early universe. Reviews of EBL measurements across the spectrum are found in [42] and [43].

Starting at the highest energies, the γ-ray background is understood to be primarily driven by emission from active galactic nuclei (AGN) and star forming galaxies, with smaller contributions from pulsars, Type Ia supernovae, and from cluster gas. Constraints on the γ-ray background primarily come from the *Compton* and *Fermi* telescopes (cf [44]). Searches for new physics in the form of an EBL excess that cannot be attributed to other sources of photons are common. An exciting possibility at γ-ray energies is the potential contribution of dark matter annihilations to the background [45].

Modeling of the UV and X-ray background is typically treated together using the formalism introduced in the next section. However, as we do not treat the X-ray

background in detail, here we summarize the key differences. While the UV background is typically treated in terms of near and far-UV components, the x-ray background is instead distinguished into *hard* and *soft* components, with the hard component attributed to low luminosity Seyfert galaxies and the soft component including both an AGN part and larger contributions from galaxy clusters and starbursts.

Moving down in energy, the near-ultraviolet (UV) and optical are, perhaps counterintuitively, the most poorly constrained parts of the EBL. This is because of the existence of bright (relative to the EBL brightness at these wavelengths) local foregrounds that are thought to arise primarily from scattering of sunlight by the interplanetary medium and scattering by the Earth's atmosphere. These components exceed the total EBL brightness at these wavelengths by as much as 1-2 orders of magnitude depending on the observed wavelength. Motivated by this problem, we study a new approach for observing the UV-EBL in Chapter 3 and discuss theoretical modeling and observations of the EBL in the following sections.

The UV-optical backgrounds are closely related to the behavior of the infrared background as photons originally emitted in the UV-optical and near-IR will be reprocessed by dust into far-IR emission. As discussed in Chapter 1, the cosmic infrared background has been well studied, primarily by CMB experiments operating at similar wavelengths such as COBE, WMAP, and Planck.

The Cosmic Microwave Background (CMB) is both the brightest and most well studied component of the the EBL. Its discovery by Penzias and Wilson [46] is often referred to as the first definitive detection of EBL photons at any wavelength. Unlike the other

components of the EBL that are produced by cosmic structures such as stars, galaxies, and AGN, the CMB is produced by the scattering of photons as the universe expands and cools from an optically thick to optically thin state. A detailed accounts of the coupled Einstein-Boltzmann physics governing the CMB is given in [47]

While the study of diffuse backgrounds has been a paradigmatic example of photometric intensity mapping, the radio component of the EBL, produced by synchotron emission in galaxies, AGN, and the lowest CMB energies, is also a dominant systematic for line intensity mapping at 21 cm of the spin-flip transition of neutral hydrogen. Characterization of the diffuse radio background will therefore be important for mitigating systematics in attempts to measure the distribution of neutral hydrogen that will probe cosmology and astrophysics.

2.1.2 Theory of the UV-Optical Background

A useful starting point for understanding the theory of the UV-optical background is the equation of cosmological radiative transfer [48], [49],

$$\left(\frac{\partial}{\partial t} - \nu H \frac{\partial}{\partial \nu}\right) J_\nu + 3HJ_\nu = -c\kappa_\nu J_\nu + \frac{c}{4\pi}\epsilon_\nu, \tag{2.1}$$

that relates an observed frame specific intensity J_ν to the comoving volume emissivity ϵ_ν. The theoretical task is to develop a model prediction for ϵ_ν in terms of recombination emission, galaxy and star formation histories, as well as AGN contributions that matches observations. Our starting point for models of the UV-Optical background are those of [50], that have also been studied in numerous works, but especially [51] and [52]. The evolution

of this model with redshift is given in Figure 2.1.

Here, we summarize the salient features of this model,

1. Recombination Emissivity: Photons absorbed through a Lyman series resonance will cause a radiative cascade that terminates in Lyα or continuum decay. Haardt and Madau's model accounts for this by determining the relevant recombination coefficients relative to the ionization rate. The integral of the resulting emission coefficients with the number density of absorbers gives the total comoving reconombination emissivity.

2. Quasar UV Emissivity: the quasar UV SED is given by a broken powerlaw, with pivot point at 1300 Angstroms and normalized by a redshift dependent fitting function for the 1 Ryd emissivity.

3. Galaxy Emissivity: Baryonic physics leads to significant evolution with redshift and variability in the galaxy emissivity. The aggregate UV luminosity density at low redshift is computed from a Schechter function and corrected for dust absorption.

Recombination emissivity contributes a smaller fraction of the UV EBL than quasar and galaxy emissivity, as photoionization equilibrium requires the output flux to be less than the input flux onto photoionized gas. While shock-heating or collisional exciton can also produce recombination photons, the magnitude of this effect is small as the neutral HI fraction in the IGM is small. We constrain a piecewise parameterization of this model in Chapter 3, following its use in the context of GALEX observations by [1].

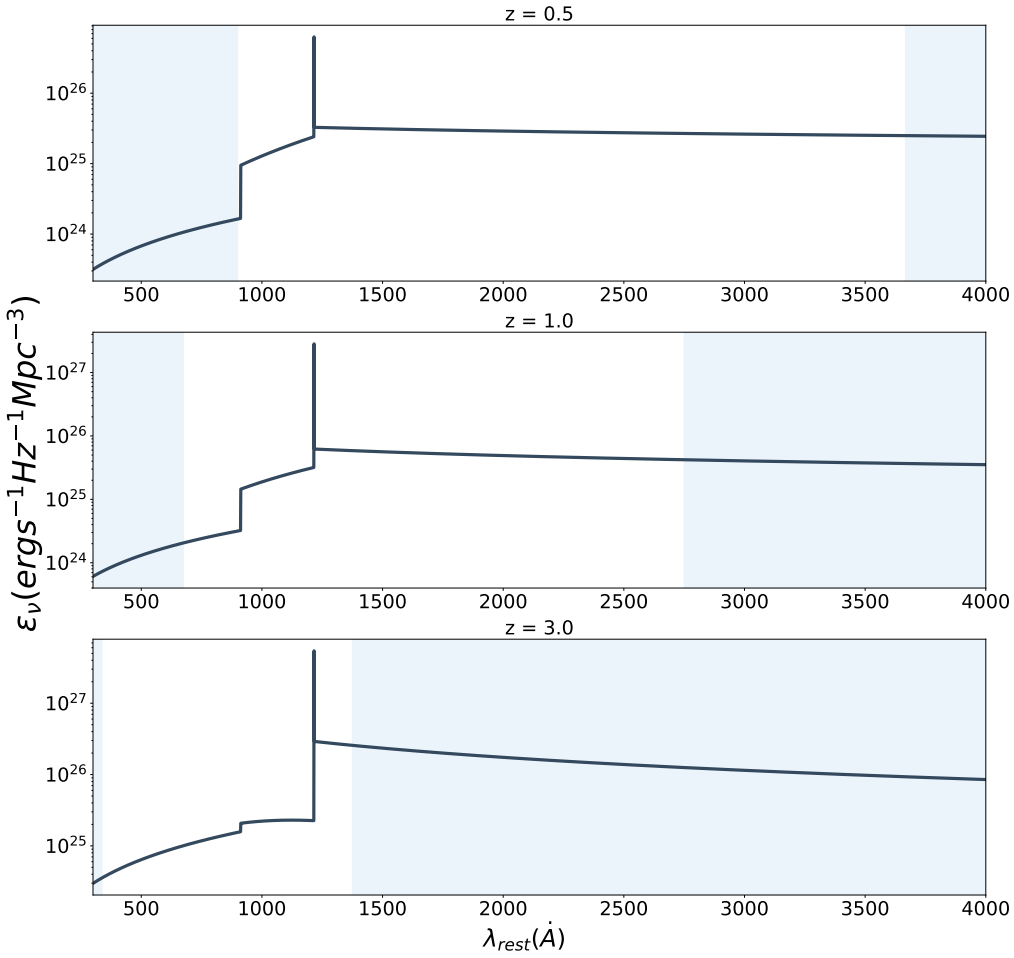

Figure 2.1: Evolution of the UV-EBL Spectral Energy Distribution (SED) in our piecewise-model at redshifts z=0.5, 1, and 3, corresponding to CASTOR's filter coverage. Shaded blue regions indicate regions outside the filter coverage at the stated redshift.

Table 2.1: Direct and indirect techniques for measuring the UV-optical EBL.

Technique	Type	Description	References
Differential Variability	Direct	Spatial or frequency variability in the foregrounds is used to isolate them from the EBL.	[53]
"Dark Cloud"	Direct	A "dark cloud" between the observer and the EBL allows for an estimate of the foreground amplitude. The difference between "on sky" and "dark cloud" measurements then gives an estimate of the EBL.	[43]
Outer Solar System	Direct/Indirect	Solar system foregrounds are largest in the inner solar system and near the ecliptic plane. Observations with outer solar system missions, including Voyager, Pioneer, and New Horizons are less subject to these foregrounds.	[54]
Number Counts	Indirect	Counting galaxies, for example with deep HST observations, and assigning a flux contribution to the EBL to each galaxy can provide an estimate of the amplitude.	[2]
γ-ray Attenuation	Indirect	Interactions between high energy γ-rays and EBL photons lead to pari-production and lower energy photons. Attenuation of high energy γ-rays therefore constrains the number of EBL photons available to interact.	[55]
Broadband Tomography	Direct	Foregrounds cancel in cross-correlation as they do not correlate with the large scale structure distribution.	[1], This Work

2.1.3 Observations of the UV-Optical Background

Measurements of the UV-Optical background can be broken up into two distinct categories. Direct measurement techniques attempt to measure the UV background by constructing estimators of the background that are insensitive to the bright local or galactic foregrounds. Indirect measurement techniques take a different approach by instead constraining quantities that isolate the galactic and extra-galactic components from the foregrounds. Dark cloud measurements, for example, measure the difference between the EBL and the EBL + foregrounds, taking the difference as an estimate of the EBL only term. Examples of direct and indirect measurement techniques are given in table 2.1.

Because direct measurement techniques have historically relied on the ability to isolate portions of the sky where foregrounds and systematics are expected to be minimized, this limits their utility for true all sky intensity mapping experiments. As a result, poten-

tially large amounts of information about the correlation properties of the UV background, including its spatial variability, are lost. Further, an increase in the sky area available can greatly minimize the statistical uncertainties and effects of cosmic variance. On the other hand, the indirect measurement techniques all rely on strong modeling assumptions about the emitting population and on the absence of potentially important selection effects. In the context of GALEX all sky UV photometric intensity maps, based on [56] and [57], [1] introduced a direct estimator of the UV background that is largely free of assumptions about and insensitive to the presence of foregrounds that do not correlate with large scale structure. As it is difficult to imagine a non-instrumental effect that would produce a foreground correlated with large scale structure, this technique offers a potentially powerful probe of the UV EBL.

Called Broadband Tomography, the elements of the approach attempted with GALEX and extended here for CASTOR, are as follows:

1. Estimate the angular cross-correlation between a photometric intensity map and a reference catalog of objects that carries redshift information

2. Forward model the cross-correlation by estimating the observed specific intensity on the sky for a set of emissivity models and estimate the expected angular cross-correlation.

3. Produce a maximum a posteriori estimate of the emissivity model parameters conditioned on the observed cross-correlation.

The elements of this technique are illustrated in Figure 2.2. The MAP estimate

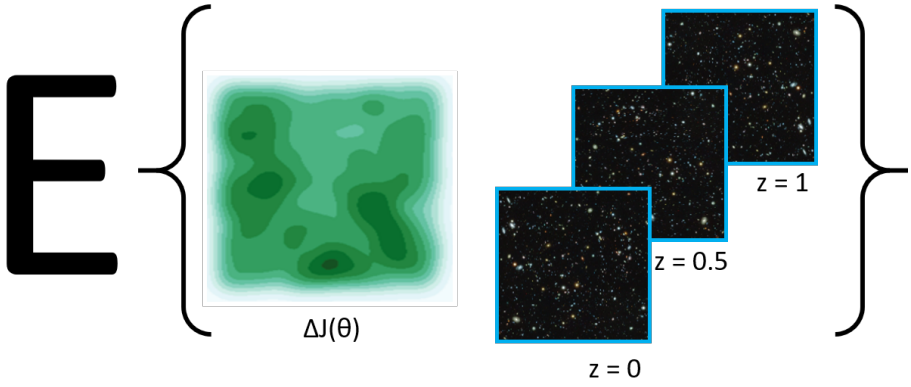

Figure 2.2: Intuitive description of the Broadband Tomographic technique. The cross-correlation between a 2D photometric intensity map in angular coordinates and a series of 3D resolved galaxy survey slices in redshift + angular coordinates is measured. The evolution of this quantity between redshift slices is used to infer the redshift distribution of photon emission in the 2D intensity map.

of the EBL parameters is taken as the best fit model for the EBL, and under additional assumptions to break degeneracies in the correlation function measurement, can be used to predict the total extragalactic only contribution to the observed diffuse background signal. An additional advantage of this technique is that it unambiguously breaks the observed signal into galactic and extragalactic components, an important consideration for consistency checks that match the observed photon intensity to theoretical models of extragalactic emission or that posit new physics present in either the galactic or extragalactic signal. This motivates the work of Chapter 3.

2.2 Gravity and Cosmology

2.2.1 Einstein Gravity

The reputation of Einstein Gravity as an intractably difficult theory obscures the intuitive premises upon which it is based and the close connection between it and a contemporary understanding of Newtonian physics and classical mechanics. In this sense, Einstein gravity is a particular theory of spacetime structure, while special relativity and Newtonian physics are alternative models that can be formulated on a similar mathematical basis[2]. Following [59], we can think of Einstein gravity as motivated by two principles that constrain the space of possible theories, but do not uniquely imply the form of the Einstein equation.

[2]See [58] for a thorough interpretation of Newtonian mechanics in geometric terms.

These are,

1. The principle of general covariance[3] that states that the metric, g_{ab} and quantities derivable from it, are the only spacetime quantities that appear in the laws of physics.

2. The equations of Einstein Gravity reduce to Special Relativity in the case that $g_{ab} = \eta_{ab}$.

to move from the above principles to a specific theory of gravity, one adds the Equivalence principle[4],

Equivalence Principle: The world lines of freely falling bodies in a gravitational field are simply the geodesics of the curved spacetime metric.

Once the equivalence principle is assumed, one looks for a relationship between nearby geodesics and a potential like term, that is, the equivalent of the Poisson equation $\nabla^2\phi = 4\pi\rho$. If one identifies the Riemann tensor with one upper index, R^a_{cbd}, with $\partial_b\partial^a\phi$ and $T_{ab}v^a v^b$ with ρ and looks for a nontrivial equation relating these terms, one arrives at the Einstein equation,

$$G_{ab} = R_{ab} - \frac{1}{2}Rg_{ab} = 8\pi T_{ab}. \tag{2.2}$$

Equation 2.2 is typically motivated through geometric arguments - considering the behavior of particles moving on curved manifolds and through consistency with Newtonian Gravity. An alternative and more generalizable approach is to posit the action of the theory

[3]The conceptual meaning and role of the principle of general covariance is unclear and has been the subject of debate since it was first proposed by Einstein in 1915. See [60] for a review.

[4]This section follows the treatment in [59], but similar to the principle of general covariance, there is debate about the historical role of the equivalence principle. [61] argues that Einstein was primarily motivated by generalizations of energy-momentum conservation as late as 1913.

of gravity and derive the Einstein equation by varying the action with respect to the metric. The appropriate choice of action that leads to the Einstein field equation is,

$$S_{E-H} = \int \sqrt{g} R. \tag{2.3}$$

Once the action is specified, the equation of motion, Equation 2.2 is obtained through variation with respect to the metric. The preceding conditions are necessary but not sufficient for a consistent theory of gravity. As such, the Einstein Hilbert action of Equation 2.3 can be modified to yield alternative theories of gravity, as we will discuss further in Section 2.5 and study observational consequences in Chapter 4. In order to introduce those observational consequences, it is necessary to discuss the connection between Einstein Gravity and cosmology.

2.2.2 Cosmology and FLRW Models

The central question of relativistic cosmology is to determine which solution of the Einstein equation corresponds to our observed universe. The apparent difficulty of this question is owed to the complexity of the Einstein equation, but reduced significantly under the potentially strong idealization of homogeneity and isotropy. Under these the assumptions, the Friedmann-Lemaître-Robertson-Walker (FLRW) solutions to the Einstein equation possess maximal symmetry and a simple topology ($\Sigma \times \mathbb{R}$), that is a stack of three-dimensional spatial surfaces labelled by values of a cosmic time coordinate [59]. These requirements lead to a particular form for the metric:

$$ds^2 = g_{\mu\nu}dx^\mu dx^\nu = -c^2dt^2 + a^2(t)(d\omega^2 + S_k^2(\omega)(d\theta^2 + sin^2\theta d\phi) \tag{2.4}$$

where ω is a radial coordinate and θ and ϕ take their usual meaning in spherical coordinates. S_k is a term that encodes the curvature of the spatial 3-surface. It takes values,

$$S_k(\omega) \begin{cases} \sin\omega & k = -1 \\ \omega & k = 0 \\ \sinh\omega & k = 1 \end{cases}$$

.

Here k is a parameter encoding whether the universe has positive (k=1), negative (k=-1), or flat (k=0) curvature. Measurements of the cosmic microwave background, baryon acoustic oscillations, and other geometric probes [62], have shown that the spatial curvature is consistent with the k=0 (flat) case. As such, in this dissertation we assume a fiducial background cosmology with zero curvature. In section 2.4, we will discuss the meaning of this assumption in the context of perturbations away from perfect homogeneity and isotropy that give rise to structure in the universe.

The preceeding description has left open the question of whether the spatial surfaces are identical or whether they evolve with respect to the temporal foliation. In fact, observations of the recession velocities of distant galaxies ("Hubble's law") suggest that it is necessary to endow our description with dynamics[5]. These are furnished by the Einstein

[5]Einstein was the first to recognize the role of his theory of gravity for cosmology. As discussed in [63], Einstein believed that a role for Mach's principle would be found in cosmology and this led him to reject dynamical solutions that were then being studied by De Sitter and others. These dynamic proposals would anticipate the discovery of the distance-redshift relationship by Hubble in 1929 and by the mid-1930s would represent the consensus view.

equation, which relates the evolution of Equation 2.4 to the energy-momentum tensor, $T_{\mu\nu}$. The result is a set of dynamical equations for the scale factor $a^2(t)$ known as the Friedmann equations [59], [64], [65],

$$\begin{aligned} \left(\frac{\dot{a}(t)}{a(t)}\right)^2 &= \frac{8\pi G}{3}\rho(t) + \frac{\Lambda}{3} - \frac{1}{K^2 a^2(t)} \\ \frac{\ddot{a}(t)}{a(t)} &= -\frac{4\pi G}{3}(\rho(t) + 3p) + \frac{\Lambda}{3}. \end{aligned} \tag{2.5}$$

With expressions[6] for the dynamics of the metric in hand, it is clear from inspection that the spatial slices evolve over time based on the values of $\rho(t)$, p, and Λ that describe the constituents of the universe. What does the universe consist of? Under the assumptions of homogeneity and isotropy, we have a particularly simple and general form for the stress-energy tensor,

$$T_{ab} = \rho u_a u_b + P(g_{ab} + u_a u_b). \tag{2.6}$$

One consequence of Equation 2.6 is that evolution in the background metric will also lead to evolution in the matter sector. In particularly, for pressureless dust ("normal or dark matter") with P = 0, the energy density, ρ, evolves with a^{-3}, while for relativistic matter ("radiation"), with $P = \rho/3$, ρ_r evolves with a^{-4}. A term that does not experience evolution with the background metric is known as a cosmological constant, Λ, and represents the simplest dark energy model.

The above results answer our initial question about the range of solutions to the Einstein equation that are consistent with observations. Some observations about these results, however, are germane. First, as the energy densities ρ_m and ρ_r are not static,

[6] Λ is included here for completeness. The significance of this term is discussed in Section 2.2.5.

but evolve with the underlying dynamics of the spacetime they inhabit, the universe will experience different epochs in which different components dominate. Second, examination of the Friedman equation leads to the startling observation that as $t \to 0$, so too does the scale factor $a(t) \to 0$. As the scale factor parameterizes the relative size of the spacetime slices, it appears that spacetime vanishes in the distant past while $\rho \to \infty$. In fact, observational evidence strongly indicates that the universe was once in a very hot and dense state.

Theoretical challenges to this paradigm arise in two primary directions. The first - often called the Cauchy problem - is to produce a theory of initial conditions. The most popular accounts of how this is to be done is through inflationary models [47, 66]. The second is related to interpreting the behavior of the spacetime as the scale factor approaches zero. Classically, this is interpreted in terms of the singularity theorems, in which such behavior is understood to be a generic feature of many spacetimes and subject only to modest assumptions, cf. Chapter 9 of [59]. One might expect that General Relativity (Einstein Gravity) is to be a replaced with a quantum theory of gravity applicable to the early universe[7]. Unfortunately, no fully consistent quantum theory of gravity, "in the UV", is yet known. The Horndeski theories we study in Chapter 4 are an "infrared", or low energy, classical generalization of Einstein gravity.

In summary, the existence of FLRW solutions that are consistent with the Einstein equation translates the task of the observational cosmologist into one of determining the component energy densities $\Omega_m, \Omega_r, \Omega_\Lambda$, and perhaps a small number of additional parameters, from observations along the past light-cone. This task can be attempted in one

[7] [67] discusses semi-classical and low energy quantum gravity theories, arguing that these are sufficient for many problems in cosmology.

of two ways. First, from direct measurement of geometric quantities or second, from the information available in large scale structure. The machinery of cosmological perturbation theory is required to make the link between structure formation and underlying cosmology or fundamental physics.

2.2.3 Theory of Large Scale Structure: Cosmological Perturbation Theory

The goal of Cosmological Perturbation Theory is to predict the large scale distribution of matter in the universe as it undergoes gravitationally driven evolution [68], [69]. We will assume that our theory of gravity is sufficiently close to General Relativity that we are furnished with a background spacetime around which to study the behavior of small perturbations. In Einstein Gravity, the task of cosmological perturbation theory is to solve the perturbed Einstein equation,

$$\delta G^{\mu}_{\nu} = 8\pi G \delta T^{\mu}_{\nu} \tag{2.7}$$

where the perturbation tensors δG^{μ}_{ν} and δT^{μ}_{ν} involve perturbations of the homogeneous and isotropic background spacetime of an FLRW model to the more realistic case of a universe with slight deviations from homogeneity. We will restrict ourselves to scalar perturbations on a flat background, as this is expected to be a very good model for the real universe. The metric of 2.4, becomes

$$ds^2 = a(\eta)^2 \left[-(1+2\Phi)d\eta^2 + (1-2\Psi)\delta_{ij}dx^i dx^j \right] \tag{2.8}$$

in the Conformal Newtonian Gauge. The functions Φ and Ψ are referred to as the Bardeen potentials. Large Scale structure measurements, such as those of a LIM experiment or galaxy survey, probe specific combinations of the Φ and Ψ [70]. The perturbation theory problem can then be broken into two constraint equations (the first and fourth) and two evolution equations (the second and third) for the Bardeen potentials.

$$\begin{aligned} 3\mathcal{H}(\Psi' + \mathcal{H}\Phi) - \nabla^2\Psi &= 4\pi G a^2 \delta\rho^N \\ (\Psi' + \mathcal{H}\Phi)_{,i} &= 4\pi G a^2 (\bar{\rho} + \bar{p}) v^N_{,i} \\ \Psi'' + \mathcal{H}(\Phi' + 2\Psi') + (2\mathcal{H}' + \mathcal{H}^2)\Phi + \frac{1}{3}\nabla^2(\Phi - \Psi) &= 4\pi G a^2 \delta p^N \\ (\partial_i\partial_j - \frac{1}{3}\delta^i_j\nabla^2)(\Psi + \Phi) &= 8\pi G a^2 \bar{p}(\partial_i\partial_j - \frac{1}{3}\delta^i_j\nabla^2)\Pi \end{aligned} \tag{2.9}$$

where $\mathcal{H}$ is the conformal Hubble constant, Π is the dimensionless anisotropic stress, and superscript N indicates that the perturbation is evaluated in this gauge. The constraint equations relate the potentials to the perturbations on a fixed time slice (elements of the foliation $\Sigma \times \mathbb{R}$), while the evolution equations evolve them backwards or forwards to future time slices. It is also possible to reframe the problem in terms of energy-momentum continuity by imposing the condition that $T^\mu_{\nu;\mu} = 0$. Note that this condition generalizes energy-momentum conservation to a curved background. This leads to a set of energy continuity equations and the Euler equation, which can be used as an alternative, and often more straightforward way, to solve for the evolution of the potentials and perturbations.

For a perfect fluid, $\Phi = \Psi$ and we can express the field equations entirely in terms of Φ and its derivatives. It is typical, then, to re-express the evolution of Φ in terms of the primordial perturbations, usually assumed to arise during inflation, in terms of a transfer

function that depends on scale and the growth function that expresses the evolution of the power spectrum with redshift (or scale factor). We have,

$$\Phi(k, a) \propto \Phi_0 T(k) D_+(a), \tag{2.10}$$

where Φ_0 is the primordial potential, $T(k)$ is a scale dependent transfer function, and $D_+(a)$ is a scale independent growth function [47]. The potential is not directly observable but is related through the Poisson equation to the observable perturbation in the matter density through the Poisson equation, which has a simple form in Fourier space,

$$k^2 \Phi(k, a) = 4\pi G \rho_m(a) a^2 \delta_m(k, a) \tag{2.11}$$

where ρ_m is the background matter density and δ is the density perturbation. Equation 2.11 provides the link between large scale structure observables, such as the correlation function and power spectrum, and the theory of large scale structure and, more generally, gravity. The power spectrum is obtained by substituting in expressions for the matter density, as well as by solving the field equations in various limits (or numerically obtaining solutions) for the transfer and growth functions. As the Poisson equation will be modified if the underlying theory of gravity is assumed to differ from Einstein Gravity, the power spectrum will generally differ in shape from the ΛCDM prediction. It is therefore a promising probe of fundamental physics.

2.2.4 Observations of Large Scale Structure in Comoving and Redshift Space

In the previous section, we developed an account of how perturbations of the background spacetime generate density perturbations in the matter sector. Our task is to develop tools to measure the matter sector perturbations and compare them with the theoretical predictions. The key idea of this section is the notion of a *cosmological point process* and is based on the observation that what is measured in a galaxy survey is the number counts of observed sources at a given redshift and position on the sky.

Beginning from the definition of a point process [21],

Point Process:

A point process in d-dimensions is a random variable taking values in a measurable space formed by the family of all sequences Φ of points in $\mathbb{R}^d$ satisfying i) local finiteness and ii) simplicity. Notationally, we say that x $\in \Phi$ if the point x belongs to the point process and that Φ is a random measure counting the points in a given region, e.g. $\Phi(A) = n = \Sigma\mathbb{1}(A)$ for A $\in \mathbb{R}^d$.

The definition of a point process is agnostic to the process that produces it. In the context of a cosmological point process, we assume that inflation (or a similar early universe process) generates a continuous gaussian distribution - a gaussian random field - of scalar perturbations characterized uniquely by a mean and variance. What is observed by a galaxy survey (or intensity map that is mediated by photon production in galaxies) is a discrete Poisson sampling of a Gaussian random field. In the point process literature, this is called a *Cox Process*, a type of (in general) doubly stochastic inhomogeneous Poisson process. On sufficiently large scales, we can model the galaxy distribution as homogenous

and driven by underlying gaussian random field. Observations of the galaxy distribution measure the (co)variance or correlation functions from counts of objects at given spatial positions.

In the language of statistical physics, the distribution of matter in the universe is represented by a stationary continuous stochastic process (SSP) or field of fluctuations about a given mean [20]. Fluctuations above the mean describe the presence of galaxies, while fluctuations below the mean describe voids. The galaxy sampling of the underlying random field discretizes this continuous field to a discrete SSP. Important properties of this SSP are stationarity and ergodicity,

Stationarity:

A stochastic process is said to be stationary if it is statistically homogenous or translationally invariant. This is justified for cosmological random fields by the assumptions of homogeneity and isotropy used to define the class of FLRW models.

an additional requirement of the cosmological point processes is that they are *ergodic*.

Ergodicity:

A process that generates a distribution $\rho(r)$ is said to be ergodic if a function F($\rho(r)$) has an expectation value $\langle F(\rho(r))\rangle$ that converges to the spatial average of F as the volume goes to infinity. In other words,

$$\langle F(\rho(r))\rangle \, \bar{F} = \lim_{V\to\infty} \frac{1}{V} \int_V d^3 r_0 F(\rho(r_0 + r_1, r_0 + r_2, ...) \tag{2.12}$$

The study of stochastic processes now furnishes the correlation function and power

spectrum, In particular, it is common to consider the reduced 2-pt correlation function,

$$\xi(r_{12}) = \frac{\langle(\hat{\rho}(r_1) - \rho_0)(\hat{\rho}(r_2) - \rho_0)\rangle}{\rho_0^2} \tag{2.13}$$

by isotropy, $\xi(r_{12})$ is a function of the separation of two points only. We interpret this as giving the excess probability of detecting a galaxy at a given separation from another galaxy. In angular coordinates on the sky, this is called the angular correlation function, and denoted $\omega(\theta)$, where θ is an angular separation vector. In Chapter 3, we work primarily in terms of the angular correlation function, as is typical for photometric intensity mapping analyses. In Chapter 4, we work in the more commonly used 3D Power Spectrum, P(k), rather than the real space correlation function. The power spectrum is defined as the function P(k) that satisfies,

$$\xi(r) = \frac{1}{(2\pi)^d} \int P(k) \exp(ik \cdot r) d^d k. \tag{2.14}$$

Which has a familiar form when d=3. The 3D power spectrum, P(k), is related to the angular power spectrum C_l through the Limber approximation [71].

Observational constraints on the Correlation function and Power Spectra are based on counts of galaxies or other tracers of the mass distribution. Chapter 4 provides explicit models for the uncertainty in the measurements of the Power Spectrum in the context of line intensity mapping in the sub-mm/far-IR, and Chapter 3 discusses the origins of correlation function uncertainties in fluctuations of tracer galaxy counts.

Difference between Comoving and Redshift Space

So far, we have considered the power spectrum expressed in the Fourier space

corresponding to comoving coordinates $\vec{r}$. Real observations, however, take place in a 2+1 dimensional space of angular coordinates, right ascension and declination on the sky, and a redshift space coordinate, z. The redshift space coordinate is converted from the comoving coordinates through the relation, $\vec{r_z} = \vec{r} + \vec{v}$, which is a sum of the comoving position and velocity of the galaxy in the comoving frame, so called peculiar velocities.

Measurements in redshift space are therefore distorted from measurements made in the comoving space. Here, we summarize the salient features of these distortions and refer the interested reader to [72] for a more complete summary. While one might initially suspect that these Redshift Space Distortions (RSD) are simply a nuisance systematic to be modeled and removed, the distortion actually carries information about cosmology that exceeds the information present only in the matter power spectra. The reason for this is that RSD are a consequence of non-zero peculiar velocities of sources in the comoving frame, and these velocities are sourced by perturbations in the matter density field through the Poisson linearized continuity equations. For linear redshift space distortion parameter β, peculiar velocity field v, and overdensity δ, we have,

$$\nabla \cdot v + \beta\delta = 0. \tag{2.15}$$

One can derive a relationship between the observed overdensity in redshift space and the *true* overdensity in comoving space by combining the continuity equation with number conservation - that is, for an identical physical volume in comoving and redshift space, the number count of galaxies is conserved. This leads to a differential operator relating the two densities. If one then makes the linear-plane parallel approximation that

the distortions are parallel to the coordinate basis, a good approximation of the observer is distant, and moves to Fourier space, one finds that the differential operator is now diagonal. Hence the distortion is linear in the comoving density with statistically independent Fourier modes. As the distortion depends on the growth of structure governed by the Poisson equation, the difference between the real and redshift space power spectrum is a potentially sensitive probe of cosmology. We will study the sensitivity of LSS measurements to modified gravity effects in Chapter 4.

2.2.5 Dark Energy and Modified Gravity

Is Einstein Gravity the correct theory of classical gravitational interactions? Remarkably, it can be shown that the Einstein equation (2.2) is, in some sense, the most general description of gravity consistent with the basic assumptions of Section 2.2.1. This result is due to [73], and can be phrased in modern notation [74] as follows,

Lovelock's Theorem:

Let (M, g_{ab}) be a four dimensional spacetime. In a coordinate neighborhood of a point p $\in M$, let Θ_α be the components of a tensor constructed from $\{g_{\lambda\mu}; g_{\lambda\mu,\nu}; g_{\lambda\mu,\nu\rho}\}$ such that $\nabla^n \Theta_{nb} = 0$, then $\Theta_{ab} = rG_{ab} + qg_{ab}$ where ∇_a is the derivative operator associated with g_{ab}, G_{ab} is the Einstein tensor, and q and r are arbitrary constants.

The above formulation is written in the language of the geometric interpretation of Einstein Gravity, but can be re-expressed in terms of the Lagrangian of the theory and the same result is obtained [75]. This result is interpreted as limiting the space of possible modifications to Einstein Gravity to,

1. Consider other fields beyond the metric tensor
2. Accept higher derivatives of the metric in the equivalent of the Einstein field equation
3. Work in a space with a higher dimensionality than four
4. Give up type (2,0) tensor field equations, symmetry of the field equations under index exchange, or divergence-free field equations
5. Give up locality

In fact, it is already known that Einstein gravity must be modified to describe the accelerated expansion of the universe [76] [77]. This is accomplished by changing 2.2 to read,

$$G_{\mu\nu} + \Lambda g_{\mu\nu} = T_{\mu\nu} \tag{2.16}$$

where Λ is a vacuum energy density. We can either view the inclusion of Λ is a modification of gravity or as a new term in the stress-energy tensor. In this context, we refer to Λ as Dark Energy, a new component energy density that is interpreted as a "modified form of matter".

In addition to Λ, we can consider the addition of a scalar ("spin-0") field, ϕ, a vector ("spin-1") field, for example, A_μ (the vector potential of classical E&M) or an

additional tensor ("spin-2"). [78]. We will specifically study a modification of the Einstein equation that includes an additional scalar field with its own dynamics. In addition to the mathematical requirements imposed on the Einstein Equation by general covariance, the equivalence principle, and by consistency with special relativity and Newtonian physics, in scalar-tensor theories, it is typical to impose the condition that the action be free of Ostrogradski instabilities. This occurs if the Euler-Lagrange equations corresponding to the action of the theory have terms that are higher than second order. This stability condition implies that the theory depends in part on derivatives of the scalar field kinetic term, and hence strongly constrains the form of the action. Schematically, the Horndeski action is of the form [79],

$$S = \int d^4x\sqrt{-g}\Sigma_i\mathcal{L}_i \tag{2.17}$$

where $\mathcal{L}$ is a function of ϕ and X = $\frac{\partial\phi\partial\phi}{2}$. The exact form is fixed by the stability conditions to be,

$$\begin{aligned}
\mathcal{L}_2 &= K(\phi, X) \\
\mathcal{L}_3 &= -G_3(\phi, X)\phi \\
\mathcal{L}_4 &= G_4(\phi, X)R + G_{4X}(\phi, X)\left[(\phi)^2 - \phi_{;\mu\nu}\phi^{;\mu\nu}\right] \\
\mathcal{L}_5 &= G_5(\phi, X)G_{\mu\nu}\phi^{;\mu\nu} - \\
&\quad \frac{1}{6}G_{5X}(\phi, X)\left[(\phi)^3 + 2\phi^{\nu}_{;\mu}\phi^{\alpha}_{;\nu}\phi^{\mu}_{;\alpha} - 3\phi_{;\mu\nu}\phi^{;\mu\nu}\phi\right].
\end{aligned} \tag{2.18}$$

Horndeski theories generalize ΛCDM, Quintessence and K-essence, f(R) and general scalar-tensor models, as well as Galileons, and Gauss-Bonnet coupling. For a full

comparison of the Horndeski action to the space of previously considered models, see [80]. We further discuss additional stability conditions on the propagation of perturbations in Horndeski theories in Chapter 4.

The introduction of dark energy Λ was motivated by the need to fit observations of Type 1a supernova that constrain the expansion rate and hence the Hubble constant. There is now a growing body of evidence that low redshift measurements, so called "local universe" observations, give an estimate for H_0 that differs from measurements of the CMB and other "early universe" probes [81]. [82] reviews a large space of dozens of possible theoretical responses to the tension and classifies solutions into 11 broad categories. A non-exhaustive list includes new relativistic degrees of freedoms, new particle physics interactions, changes to inflationary physics, modified recombination histories, and various flavors of dynamical dark energy.

Horndeski theories with a dynamically evolving scalar field coupled to the background evolution are a natural framework for considering such models [83]. This allows for the equation of state parameter ot either "freeze" or "thaw", that is, w either decreases to its cosmological constant value of -1 or increases away from -1 as the scalar field evolves. Dynamical dark energy models have been studied extensively, cf [84], and for early dark energy constraints from LIM by [85]. LIM is especially promising for searching for signs of dynamical dark energy because it probes both large cosmological volumes and a wide range in redshift. This motivates the work of Chapter 4.

Chapter 3

Forecasts for Broadband Tomography with CASTOR and SPHEREx

3.1 Introduction

The extragalactic background light (EBL) is a powerful probe of structure formation, cosmic star formation history, and the intergalactic medium [86, 87]. Because the ultraviolet background (UVB) component of the EBL is both a direct probe of these processes and sets the ionization state of the intergalactic medium, understanding the evolution of the UVB and the EBL is both an important modeling problem and a promising observational constraint on the photon distribution. Contributions to the EBL (and UVB) come from direct emission due to galaxies and active galactic nuclei that produce a discrete

component, and from radiative processes, including dust scattering and recombination that produce a diffuse component. The EBL contains information about the emission over cosmic time of total integrated processes, and therefore provides an important consistency check for models that attempt to reproduce the photon production history of the universe [13].

In the ultraviolet (UV), direct measurements of the EBL have been attempted with Voyager 1 and 2 at 110 nm [88], and with Voyager UVS at 100 nm [89]. At these wavelengths, the dominant foreground uncertainty is due to skyglow, leading to large uncertainties on the total EBL intensity [43]. In the blue portion of the optical, attempts have also been made with Pioneer 10 and 11 [90] at 440 nm with the broadband Long Range Reconaissance Imager (LORRI) on New Horizons from 440 nm - 870 nm [91]. Direct photometric measurements with New Horizons have found that a large fraction of background photons may be associated with a diffuse component not associated with identified sources [54]. This diffuse component may arise either from galactic sources or extragalactic sources below the limiting magnitude of current galactic surveys.

Beyond spacecraft measurements, observations as a function of galactic latitude [4, 53] place upper limits on the total combined galactic and extragalactic component, subject to foreground uncertainties due to the zodiacal component and contributions from faint stars. One way to mitigate these uncertainties is the dark cloud technique [92, 3], where observations are taken in the direction of opaque clouds in the interstellar medium and compared to blank sky observations. The difference between these two measurements is taken to estimate the foreground and combined brightness. Each of these techniques attempts to capture the contribution of diffuse emission at low surface brightness, which results in large

statistical and systematic uncertainties arising from the larger skyglow, zodiacal, and galactic foregrounds. The latter also complicates interpretation of direct intensity constraints as they must be decomposed into galactic and extra-galactic components.

An alternative strategy (for a recent review see Hill2018) integrates the total emission over number and luminosity counts of sources down to some limiting magnitude [93, 94, 2]. This derives an indirect lower limit on the extragalactic component, subject to large uncertainties in the contributions of fainter and diffuse sources. Since constraints on the photon production history of the universe require knowledge of the diffuse component that is produced by both undetected sources and scattering far from detected discrete sources, significant uncertainties remain about the relative contributions.

To measure the total contribution of faint sources, intensity mapping measures a continuous spatial brightness function on the sky without setting an absolute detection threshold. Using the intensity maps in the Galaxy Evolution Explorer (GALEX) near (NUV) and far ultraviolet (FUV) from [95] and [53], [1] introduced the concept of broadband intensity tomography to measure the EBL. By cross correlating a spectroscopic tracer catalog with these maps [56, 57], an integrated constraint on the total EBL in two filters was derived with high fidelity separation between the extragalactic signal and the foreground and galactic contributions. In this work, we forecast a similar measurement using future UV telescopes. We consider in particular the Cosmological Advanced Survey Telescope for Optical and UV Research (CASTOR), a one meter class telescope intended for launch in the mid to late 2020s [96], and Spectro-Photometer for the History of the Universe, Epoch of Reionization and Ices Explorer (SPHEREx). CASTOR is a wide field of view survey satellite

capable of producing all sky intensity maps with an expected 0.15" PSF. SPHEREx is an infrared observatory which can extend and complement local restframe UV measurements by observing at higher redshifts, $z \approx 5 - 9$.

The nominal mission design for CASTOR includes a survey over a 7700 deg^2 [96] region defined to cover the overlap between the Roman Space Telescope [97], Euclid [98], and Vera C. Rubin Observatory [99] survey areas. It will provide complementary information in the optical and near ultraviolet to those surveys targeting longer wavelengths. The CASTOR surveys would be performed in three broadband filters from 150 nm to 550 nm. The larger mirror size, overall redder filter set and improved calibration compared to the < 250 nm NUV and < 150 nm FUV filters on GALEX offers potential for extending integrated constraints on the UV-optical background light, including Lyman continuum (LyC) escape fractions, the slope and normalization of the continuum emission and its evolution to intermediate redshifts up to $z \approx 3 - 4$, with improved error properties at lower redshift.

SPHEREx is an all sky spectro-photometric survey covering 0.75-5 μm. The spacecraft features a 0.2 m mirror and produces spectra of 6.2 arcsec^2 pixels by scanning 96 linear variable filters across the sky. Although nominally an infrared survey, at $z > 5 - 9$, SPHEREx will produce rest-UV intensity maps of Lyα emission. Modeling the complete response of a set of narrowband filters approximating the SPHEREx instrument can extend these maps to measure the UV continuum and its evolution across these redshifts.

The plan of this paper is as follows. In Section 3.2, we introduce our notation and derive the cross-correlation function which is at the heart of broadband tomography. In Section 3.3, we introduce our emissivity model and the application of this technique to the

expected CASTOR throughput and wavelength coverage. Section 3.4 estimates the error budget for such a survey. In Section 4.4, we discuss how the additional filter and different wavelength coverage impact our inference of the underlying spectral energy distribution and the EBL monopole. Finally, in Section 3.6, we extend these results with a discussion of how a broadband tomographic measurement with CASTOR is complementary to broadband constraints from SPHEREx and LUVOIR on the ultraviolet background and history of Lyα emission. We conclude in Section 3.7 with a summary of this work.

Where necessary, this paper assumes a 2018 Planck fiducial cosmology [62] with $\Omega_m = 0.31$, $\Omega_\lambda = 0.69$, $\Omega_B = 0.05$, and $H_0 = 67$ km/s/Mpc.

3.2 Broadband Tomographic Intensity Mapping

In this Section we will introduce our notation and derive the cross-correlation function between photon over-intensity and matter over-density. We will work throughout with quantities averaged over angular shells. Quantities will be a function of r, the size of a radial shell on the sky, or θ, the angular distance on the sky. We will also measure change with redshift, z, and denote quantities which depend on frequency with a subscripted ν. We follow the derivation from Section 2 of [1], and summarize below.

3.2.1 The Filter Specific UV/Optical Photon Intensity

The comoving emissivity in the restframe, $\epsilon_\nu(r, z)$, often presented in ergs $\mathrm{s}^{-1}\mathrm{Mpc}^{-3}$ Hz^{-1}, is not a directly observable quantity, but is related to the observed angle average specific intensity at frequency ν, $j_\nu(r, z)$ (in ergs s^{-1} $\mathrm{cm}^{-2}\mathrm{Hz}^{-1}\mathrm{Sr}^{-1}$) via the equation of

cosmological radiative transfer [48];

$$\left(\frac{\partial}{\partial\nu} - \nu H(z)\frac{\partial}{\partial t} + 3H(z)\right) j_\nu(r,z) \tag{3.1}$$

$$= -c\kappa_\nu j_\nu(r,z) + \frac{c}{4\pi}\epsilon_\nu(r,z)(1+z)^3\,. \tag{3.2}$$

Here $H(z)$ is the Hubble function, c is the speed of light and κ_ν is the opacity. The integral solution in the observed frame is

$$j_{\nu,obs}(r) = \frac{c}{4\pi}\int_0^\infty dz \frac{1}{H(z)(1+z)}\epsilon_\nu(r,z)e^{-\tau_{\rm eff}(\nu,z)}, \tag{3.3}$$

and $\nu = (1+z)\nu_{\rm obs}$. $\tau_{\rm eff}(\nu,z)$ is the effective optical depth, for which we use the simple model of [100],

$$\tau_{\rm eff}(\nu,z) = \frac{4}{3}A\sqrt{\pi\sigma_L}\left(\frac{\nu}{\nu_L}\right)^{-1.5}\left((1+z)^{1.5}-1\right), \tag{3.4}$$

where $A = 1.4\times10^7$ is a normalization constant fixed by estimates of the density of Lyman Limit Systems (LLS), $\sigma_L = 6.3\times10^{-18}{\rm cm}^2$ scales the hydrogen photoionization cross section, and ν_L is the Rydberg frequency 3.3×10^{15} Hz.

A broadband survey measures the convolution of this quantity with the filter response function $R_Y(\nu_{obs})$,

$$J_Y(r) = \int \frac{d\nu_{obs}}{\nu_{obs}} R_Y(\nu_{obs}) j_{\nu,obs}(r)\,. \tag{3.5}$$

Here Y denotes the filter band and is u, v or g. $R_Y(\nu_{obs})$ has been normalized such that $J_Y(r) = j_\nu(r)$ for a flat input spectrum. This ensures that the band averaged magnitude is a function of the source emissivity over the observed frequencies, rather than the band shape.

3.2.2 The Broadband Tomography Cross-Correlation Function

Intensity mapping experiments measure a continuous spatial flux distribution, rather than a discrete sampling of emitting sources. Thus, rather than constructing a catalog of objects, intensity mapping experiments produce maps of the sky in which the intensity of each pixel is associated with both resolved and unresolved sources.

Broadband tomography [1] is a technique for extracting the redshift distribution of emission from intensity maps in the presence of bright foregrounds. Cross correlating an intensity map with a spectroscopic tracer catalog results in an estimate of the emission distribution in redshift. Here we summarize the key features of this technique and refer the interested reader to previous work for more details.

Our ultimate aim is to estimate the comoving emissivity as a function of redshift, $\epsilon_\nu(z)$, from the band averaged specific intensity, J_Y, measured on the sky. We build a model for $\epsilon_\nu(z)$, and forward model an estimate of the redshift evolution of J_Y, denoted dJ_Y/dz. We compare this forward model to the cross-correlation of the over-intensity observed in the map with a reference catalog and thus estimate the parameters of the model.

To make this explicit, consider a field X with coordinates (ϕ, z), where ϕ is the angular separation from some reference location θ, and a spectroscopic tracer object. If the overdensity of spectroscopic tracer objects is represented by $\delta_r(\phi+\theta, z)$ (which is 1 if a tracer object is located at a location $\phi+\theta$ and 0 otherwise), then the cross-correlation is

$$\omega_{X,r}(\theta, z) = \int X(\phi, z)\delta_r(\phi+\theta, z)d\phi \tag{3.6}$$

Subscripts indicate the two fields that are being cross-correlated. Subscript X would be ϵ

for the emissivity map, or J for the observed band-averaged specific absolute over-intensity ΔJ_Y. Subscript r indicates the reference emitter catalogue.

To relate the observable cross correlation to the comoving emissivity in redshift, consider the case where we have three dimensional information about the distribution of emitters. Then the comoving emissivity, $\epsilon_\nu(\theta, z)$, is given by

$$\epsilon_\nu(\theta, z) = \epsilon_\nu(z)(1 + \omega_{\epsilon,r}(\theta, z)) \,, \tag{3.7}$$

$$\epsilon_\nu(z) = \langle \epsilon_\nu(\theta, z) \rangle \ ,$$

where $\epsilon_\nu(\theta, z)$ is the specific emissivity at angular separation θ from objects in the reference catalogue at redshift z and $\epsilon_\nu(z)$ is the spatial mean specific emissivity. Angle brackets denote a 2D average over both sky directions. $\omega_{\epsilon,r}(\theta, z)$ is the angular cross correlation function between emissivity and the spectroscopic tracer catalogue, defined in Equation 3.6. Equation 3.7 is interpreted as giving the excess probability of detecting photons at the given separation.

Our goal is to relate this to the observable cross correlation between the band-averaged specific intensity map and the spectroscopic catalog, $\omega_{J,r}$. To do this, we substitute the integral solution of Equation 3.3 into Equation 3.7, and then apply the binning integral from Equation 3.5 to find

$$J_Y(\theta) = \langle J_Y(\theta) \rangle + \int \omega_{\epsilon,r}(\theta, z) \frac{dJ_Y}{dz}(\theta, z) dz \,. \tag{3.8}$$

The first term on the right side of Equation 3.8 represents the average specific intensity, or monopole, while the second is the term we seek, relating the shell 1-bin averaged map intensity J_Y to the redshift distribution and the rest frame emissivity cross correlation.

To increase the signal to noise ratio on estimates of the cross correlation, we define normalized weights $W(\theta)$ such that $\int W(\theta)d\theta = 1$ in angular separation and integrate out the angular dependence to produce a one-bin measurement of the cross correlation or another angular dependent quantity.

The second term in Equation 3.8 can be expressed in terms of the underlying matter correlation function $\omega_{MM}(z)$ if both the intensity map (or comoving emissivity) and the large scale structure tracer are biased tracers of it.

$$\omega_{J,r}(z) = \frac{dJ_Y}{dz} b_r b_{im} \omega_{M,M}(z). \tag{3.9}$$

As both the tracer catalog and the EBL photons are biased tracers of the underlying matter field, we include scale-independent linear bias factors b_{im} and b_r. This defines the angular cross correlation function, $\omega_{J,r}$ between the tracer catalog and the intensity map, which is the observed quantity. The use of the angular correlation function to extract redshift dependent quantities in this way is due to [56]. The explicit result in Equation 3.9, however, was first arrived at in [57] who take this as the definition of the angular cross correlation function $w_{J,r}$ between the specific intensity (or its band averaged counterpart) and the large scale structure tracer.

Equation 3.9 is the intrinsic observable obtainable in a broadband measurement, where J_Y is the band averaged specific intensity (Equation 3.5), which depends on the integrated source rest frame emissivities, ϵ_ν (see Section 3.3 for our modelling of these quantities). The matter angular correlation function $\omega_{M,M}$ can be estimated either numerically with tools like CLASS [101] or CAMB [102] or with fitting functions [103]. The

assumption of linear or scale independent biasing is valid on the large scales measured here and has been tested in the context of clustering redshift estimation in [104, 105]. dJ_Y/dz encodes information about the astrophysics of UV photon production, while the remaining terms encode the structure formation history and underlying cosmology dependence.

We will consider the effect of modeling the reference catalog bias b_r in Section 3.4.2 and infer the evolution of the map bias, b_{im}, by modeling it as a double power law in redshift and frequency, with evolution parameters γ_ν and γ_z:

$$b_{im}(\nu, z) = b_{1500}^{z=0} \left(\frac{\nu}{\nu_{1500}} \right)^{\gamma_\nu} (1+z)^{\gamma_z} \,. \tag{3.10}$$

These model the evolution of the frequency and redshift dependent photon clustering bias $b_{im}(\nu, z) \approx b_{im}(\bar{\nu}, z)$ that we evaluate at the effective frequency ($\bar{\nu}$) of the filter in estimating cosmic or sample variance on a per filter basis. The effective frequency we compute averages over the filter response, estimating the effective bias by its average value in the filter. Although choices in how this average is performed may change the estimate of the filter-specific cosmic variance, this is dominated by the bias weighted integral of the correlation function of the underlying matter field, which on the scales we consider is orders of magnitude smaller than the contributions of field to field variance, shot noise in the spectroscopic catalog, and evolution of the bias. As such, the choice to include or exclude filter-specific cosmic variance does not change our forecasted constraints on UVB model parameters.

3.3 Emissivity Model

3.3.1 Restframe Model

The comoving UV emissivity– the frequency-dependent energy emitted per unit time and volume– is written as the sum of UV photon contributions from all sources. UV photons can be produced by stellar populations in galaxies (written as $\epsilon_\nu^\star$), by active galactic nuclei ($\epsilon_\nu^{\rm AGN}$), and through recombinations ($\epsilon_\nu^{\rm rec}$), all of which are considered in the source rest frame. Therefore, the total restframe emissivity ϵ_ν determined from broadband observations is

$$\epsilon_\nu = \epsilon_\nu^{\rm AGN} + \epsilon_\nu^\star + \epsilon_\nu^{\rm rec}\,. \tag{3.11}$$

Our model for ϵ_ν follows [1] and parameterizes the model in [50]. This model has been compared to broadband tomographic constraints from GALEX and used to inform improved synthesis modeling in [52]. We approximate the spectral energy distribution of the EBL over the wavelength range 500 to 5500 Å as a series of piecewise defined power laws. The filter width of the instrument is much wider than the emission feature, so the Lyman-α emission line can be represented by a delta function at 1216 Å.

For ionizing photons with $\lambda < 912$ Å, $\nu > 3.29 \times 10^{15} Hz$, we write

$$\epsilon_\nu = f_{\rm LyC}(z) \left(\frac{\nu_{1216}}{\nu_{1500}}\right)^{\alpha_{1500}} \left(\frac{\nu_{912}}{\nu_{1216}}\right)^{\alpha_{1216}} \epsilon_{1500} \left(\frac{\nu}{\nu_{912}}\right)^{\alpha_{912}}, \tag{3.12}$$

where $f_{\rm LyC}$ is a function that parameterizes the evolution of the Lyman continuum escape fraction. We normalize $f_{\rm LyC}$ at redshifts where the Lyman break is directly constrained as

it passes through the GALEX filters, such that

$$\begin{aligned}\log f_{\mathrm{LyC}}(z) = &\left(\left(\log f_{\mathrm{LyC}}^{z=2} - \log f_{\mathrm{LyC}}^{z=1}\right) / \log\left(\frac{1+2}{1+1}\right)\right) \times \\ &\log\left(\frac{1+z}{1+1}\right) + \log f_{LyC}^{z=1}.\end{aligned} \tag{3.13}$$

ϵ_{1500} will appear in each expression and normalizes the total emissivity to its value at 1500 Å, while ν_{X} is the frequency corresponding to X Å. Similarly, α_{X} is the spectral slope at X Å for X = 912, 1216 and 1500 Å. The spectral slopes at 1216 and 1500 Å evolve with redshift according to

$$\alpha_X = \alpha_X^{z=0} + C_{\alpha X}\log(1+z), \tag{3.14}$$

where $X = 1216, 1500$, and the $\alpha_X^{z=0}$ are the values of the power law parameters at $z = 0$ as determined from the GALEX intensity photometric intensity maps in [1].

For photons overlapping with Lyman-α emission, that is 912-1216 Å, or $\nu = 2.47 - 3.29 \times 10^{15}$ Hz, we supplement the power law with a delta function for Lyman-α:

$$\begin{aligned}\epsilon_\nu &= \epsilon_{1500}\left(\frac{\nu_{1216}}{\nu_{1500}}\right)^{\alpha_{1500}}\left[\left(\frac{\nu}{\nu_{1216}}\right)^{\alpha_{1216}} + D(z,\nu)\right] \\ D(z,\nu) &= \mathrm{EW}_{\mathrm{Ly}\alpha}(z)\delta(\nu-\nu_{1216})\left(\frac{\nu^2}{c}\right).\end{aligned} \tag{3.15}$$

Motivated by the midpoints of the GALEX filter bands, we follow [1] and model the Lyα equivalent width, $\mathrm{EW}_{\mathrm{Ly}\alpha}(z)$, as linear in $\log(1+z)$:

$$\begin{aligned}\mathrm{EW}_{\mathrm{Ly}\alpha}(z) &= C_{Ly\alpha}\log(1+z) + EW_{Ly\alpha}^{z=0.3} \\ C_{Ly\alpha} &= (EW_{Ly\alpha}^{z=1} - EW_{Ly\alpha}^{z=0.3})/\log\left(\frac{1+1}{1+0.3}\right)\end{aligned} \tag{3.16}$$

CASTOR measures redder wavelengths than GALEX ($0.15-0.55\mu$m instead of $0.1-0.15\mu$m), and so the new data will not measure $\mathrm{EW}^{0.3}_{\mathrm{Ly}\alpha}$. We therefore fix it to the fiducial value of -6.17 from GALEX. Similarly, we fix $\alpha_{912} = -1.5$ as this parameter lacks a direct data constraint in CASTOR or GALEX photometry. The final piece of the emissivity model is the non-ionizing or long wavelength continuum for photons with wavelengths greater than 1216 Å or $\nu < 2.47 \times 10^{15}$ Hz,

$$\epsilon_\nu(z) = \epsilon_{1500} \left(\frac{\nu}{\nu_{1500}} \right)^{\alpha_{1500}}, \tag{3.17}$$

with redshift evolution

$$\epsilon_{1500} = \epsilon^{z=0}_{1500}(1+z)^{\gamma_{\epsilon 1500}}. \tag{3.18}$$

Intensity mapping experiments measure a biased tracer of the underlying matter distribution. ϵ_{1500} is thus constrained only as a product with the $z = 0$ bias normalized $b^{z=0}_{1500}$.

In summary, our emissivity model has 11 free parameters that we evaluate in our inference from $\lambda = 700$ to 3000 Å. Four parameters model the power law slope of the emissivity with redshift ($\alpha^{z=0}_{1216}$, $\alpha^{z=0}_{1500}$, $C_{\alpha 1216}$, $C_{\alpha 1500}$). Two model the log of the Lyman continuum escape fractions ($\log f^{z=2}_{LyC}, \log f^{z=1}_{LyC}$). Additionally, we have the Lyα equivalent width at $z = 1$ ($\mathrm{EW}^{z=1}_{\mathrm{Ly}\alpha}$), the product of the emissivity and the bias normalization $\log(\epsilon^{z=0}_{1500} b^{z=0}_{1500})$ and the redshift evolution of the emissivity $\gamma_{\epsilon 1500}$.

3.3.2 Projection in Redshift Space

The piecewise model of Section 3.3.1 is related to the observed frame intensity j_ν via Equations 3.1-3.5. To derive the observed frame quantity, we also require an instrumental response function which characterizes the transmission fraction or the probability

of detecting an incident photon. This yields an instrumental magnitude of a source, which is a combination of the distribution of emitted photons, the distance to the source, and the instrumental response to detected photons. We can thus convert the observed broadband intensity in frequency space into a broadband intensity distribution in redshift. Combining Equations 3.3-3.5 above yields the observed frame quantity desired in Equation 3.9 for a tomographic survey,

$$\frac{dJ_Y}{dz} b_{im}(z) = \frac{c}{4\pi H(z)(1+z)} \int \frac{d\nu_{obs}}{\nu_{obs}} R(\nu_{obs}) b_{im}(\nu, z) \epsilon_\nu(z) e^{-\tau_{eff}(\nu,z)}, \tag{3.19}$$

where c is the speed of light, $H(z)$ is the Hubble function, τ_{eff} is the effective optical depth, ν is the emission rest frame frequency and ν_{obs} is the observed frame frequency.

Equation 3.19 is a band averaged intensity distribution and a function only of redshift. In this sense, the instrumental response function has turned the rest-frame emissivity function into a photon distribution in redshift by convolving a frequency and redshift dependent quantity with a function that is of frequency only. The behavior of this function is most easily seen by considering a single delta emissivity function in frequency that is produced at a range of wavelengths. In this case, one would simply recover exactly the filter curve in redshift space (see Figure 1 of [1]). The redshift distribution functions are then filter specific combinations of the evolution of the underlying emissivity distribution and the instrument response.

3.4 The CASTOR Filters and Error Budget

CASTOR is a proposed near UV-optical survey telescope. Wavelength coverage

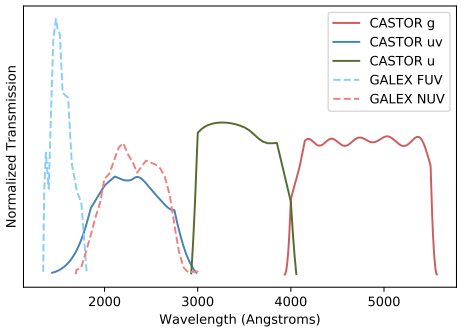

Figure 3.1: The filter transmission curves for CASTOR UV, u, and g filters (solid) and GALEX NUV and FUV (dashed). The short wavelength GALEX FUV filter is not replicated in CASTOR, which replaces it with two redder filters.

for the UV imaging instrument is $\approx 550 - 5500$ Å. The filter response functions $R(\nu_{obs})$ are shown in Figure 3.1, where we have also included the GALEX $\{NUV, FUV\}$ filter sets for comparison. GALEX covers effective wavelengths $0.1 - 0.15\mu$m in the FUV and NUV, compared to effective wavelengths of $0.23 - 0.5\mu$m for the $\{uv, u, g\}$ filters on CASTOR. The NUV and uv filters on GALEX and CASTOR provide similar constraining power, while the u and g filters extend the data constraints in observed frame frequency and thus higher redshift. CASTOR thus has weaker constraints on short wavelength emission at low redshift, but greater potential to constrain shorter wavelengths at higher redshifts in the red filters. While GALEX samples the continuum to $z = 1$ in the FUV and $z = 2$ in the NUV, CASTOR's redder filters extend these constraints to $z = 2.5 - 3$ in the g band.

In this section we will describe our error models for a CASTOR like survey. We will consider the contributions from shot noise (Section 3.4.1), photometric zero point (Section 3.4.3), and evolution of the reference catalog bias (Section 3.4.2). We place upper and lower bounds on the total error budget from these contributions.

3.4.1 Shot Noise

For a galaxy tracer-intensity map cross correlation, shot noise is introduced due to both the discrete nature of the galaxy tracers and the contribution from the tracers to the observed intensity in the map. In other words, for a flux weighted cross correlation, the amplitude of the shot noise becomes flux weighted. To estimate the size of the shot noise on estimates of the correlation function, one can use a counts in cells approach, as in [106] developed for HI intensity mapping or work directly from the definition of the cross correlation estimator. In either case, for a tracer with angular number density n_g, the variance in flux weighted counts is then (cf. [20]),

$$\sigma^2_{SN} = \frac{\langle J_Y \rangle}{n_g}. \tag{3.20}$$

This corresponds to a scale independent shot noise with amplitude set by the angular number density of tracer objects per redshift bin, n_g. In general, the tracer catalog density will be a function of both the galaxy density function in units of number per steradian, which can be computed from the halo mass function dN/dM, where dN is the number per mass bin M+dM, by integrating in mass and over the cosmological volume and a survey selection function.

To model the tracer distribution as a function of redshift, we take the SDSS CMASS and LOWZ [107], eBOSS LRG and QSO [108], and SDSS QSO DR12 [109] and DR14 [110] catalogs and divide the redshift distribution into 80 bins from redshift $0 - 4$. In total, this corresponds to 2,727,612 tracer objects distributed over $\approx$ 7000 square degrees in the northern hemisphere.

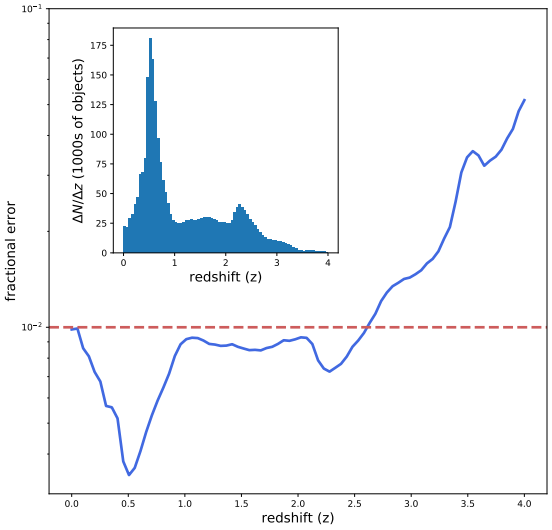

Figure 3.2: The fractional error budget as a function of redshift $\sim 1/\sqrt{n_g}$. Also plotted is a photometric zero point error for which we assume a fixed 1% value in our optimal error model. Inset is the redshift distribution from the SDSS tracer surveys we consider in this work. The corresponding shot noise curve is multiplied by a factor of 5 to account for the improved depth of future spectroscopic catalogs, and calculated using the relationship derived in § 3.4.1

We plot the total error budget in Figure 3.2. At most redshifts, the photometric zero point error is larger than the shot noise component. Future spectroscopic tracer catalogs are expected to improve on the completeness, that is, detect a larger fraction of galaxies contributing to the diffuse component of the UVB, of existing surveys, especially at $z > 1$. In Section 3.4.3 we discuss how uncertainty in the field to field photometric zero point propagates to a $1 - 3\%$ uncertainty in the angular correlation function. Shot noise from existing tracer catalogs is subdominant to the photometric error for $z \gtrsim 0.2$ and for $z \lesssim 2.6$. In Section 3.4.4 we will consider two noise models that bound the uncertainty in the recovery of the intensity distribution in redshift. In order to set the lower bound, we consider a spectroscopic tracer catalog improved in depth, as measured by the number density of sources in each redshift bin, by a factor of 5, which delivers a shot noise term that is subdominant to the photometric error for $z < 4$. Concurrent with the nominal lifetime of the observatories we consider, in the mid to late 2020s, several large scale structure experiments will deliver deeper spectroscopic catalogs. In particular, the Dark Energy Spectroscopic Instrument is expected to deliver a factor of 10 improvement in depth over the catalogs we consider, $\approx$ 30 million galaxy and quasar redshifts, between $z = 0$ and $z \gtrsim 3.5$ [111].

The shot noise estimate given in Equation 3.20 assumes that noise is due entirely to emission from discrete sources. That is, we neglect the variance in estimating the flux from an intensity map discretized due to the finite resolution of an observed intensity map. This underestimates the error since the intensity map will also have contributions from diffuse emission due to extra-galactic sources below the detection limit of spectroscopic tracer

catalogs. Given the deeper spectroscopic catalogs we consider, we expect the overall effect of neglecting the contributions of diffuse sources to be a larger effect for current than for future surveys. This leads us to expect that, with the improved depth of future spectroscopic catalogs, neglecting the diffuse extra-galactic component in our analytic approach will lead to only a small underestimate of the total noise amplitude.

It is important to note that our definition of the map bias, b_{im}, encodes that the observed map intensity J_Y is a biased tracer of the underlying matter density field. As a result, the estimate of the shot noise in Equation 3.20 is a bias weighted estimate. Since dim and diffuse sources will be less clustered than more massive sources that produce a greater observed intensity, we expect that the contribution of diffuse sources to the shot noise in the map will be less than the contribution from the discrete sources considered in the cross-correlation.

The frequency resolution for discrete features of the spectral energy distribution is set by the ratio between the reference catalog binning δ_r, in redshift space given by $\Delta z = 0.05$, and the intrinsic clustering scale δ_c [57]. This is because the clustering scale is a small number when evaluated in redshift space. A 5 Mpc angular separation corresponds to $\Delta z \approx 0.001$ at $z = 0$ and $\Delta z \approx 0.01$ at $z \approx 1$. The signal to noise ratio also increases with the effective survey volume, owing to more tracer objects in the reference catalog. Broadband estimates of the SED therefore favor larger survey volumes and hence larger redshift binning.

For existing spectroscopic catalogs, shot noise is comparable to photometric errors. However, improved tracer catalogs reduce uncertainties by a factor of the survey depth, thus

requiring improved photometric error control. Still broadband tomography may provide advantages over other measurement techniques as these are often limited by the ability to perform a foreground decomposition into galactic and extragalactic components.

3.4.2 Error due to Bias Evolution in the Tracer Catalog

From Equation 3.9, the ability to extract the bias weighted redshift distribution $\frac{dJ_\nu}{dz} b_{im}(\nu, z)$ is limited by knowledge of reference catalog bias b_r evolution with redshift. Uncertainty in the angular correlation function and the tracer catalog bias propagates to the cross-correlation, $\frac{dJ}{dz} b_{im}$ (eq. 3.19). We can estimate the contribution of the bias evolution to the inferred distribution by considering the mean offset in the inferred redshift,

$$E[\hat{z}] - z = \int z^{\alpha+1} \mathcal{N}(z_0, \sigma) dz - \int z \mathcal{N}(z_0, \sigma) dz, \tag{3.21}$$

We assume a Gaussian probability distribution, $\mathcal{N}(z_0, \sigma)$ for the emission redshift, z. z_0 is the true mean redshift of the emission, σ is the associated standard deviation of the distribution about z_0 and α is a parameter describing the bias evolution such that $b_r \propto z^\alpha$. Following [57], we assume that $\alpha = 0.1$, that is, estimates of the bias neglect up to 10% of its evolution with redshift and that $\sigma \approx 0.5$ based on the SDSS redshift distribution. We show the evolution of Equation 3.21 with redshift as the dotted curve in Figure 3.3. This effect is largest at low redshift and decreases rapidly at higher redshift.

3.4.3 Photometric Zero Point and Cosmic Variance

Errors in the photometric zero point of the intensity map and tracer catalog contribute to the determination of the angular correlation function [112] due to the finite field

of view measured by each exposure. Varying zero points between fields produce an effectively varying magnitude limit, which in turn produces a difference in map depth and a change in the estimated surface brightness. That is, since we take correlations between the tracer catalog and the absolute overintensity, variations in the effective mean intensity $\langle J_Y \rangle$ propagate to cause spurious changes in ΔJ_Y.

A second and smaller effect arises from differences in the photometric zero point, or catalog depth, of the spectroscopic tracer catalog. Here, the effect is to increase the variance beyond the typical Poisson 1/N scaling as each field varies due to the fluctuating magnitude limit. The photometric effect scales with the photometric zero point fluctuation amplitude and, since it is a consequence of field to field variations, the number of fields over which the cross correlation is measured. The spectroscopic effect is an order of magnitude smaller, [56] estimated this latter effect at the roughly 0.1% level in Monte Carlo tests under conservative assumptions.

For CASTOR, the mirror diameter increases to 1 m from 0.5 m for *GALEX* leading to increases in the point-source derived limiting magnitudes from 19.9 fuv, 20.8 nuv, in GALEX All-Sky Imaging Survey (AIS) to ≈ 27, in the uv, u, and g for CASTOR respectively [113]. Although not derived for a low surface brightness background measurement in a photometric intensity mapping survey, we expect similar corresponding improvements in the photometric error properties for *CASTOR*. A rough estimate for the photometric error, which scales with mirror area, is that it should improve by a corresponding multiple of the improvement in the mirror size. This is because the field to field variance is due to drop out of sources, and the probability of detecting a source in a given field is a function of the limiting magnitude, set by the integration time and mirror size. The important quantity, here, is not the absolute photometric zero point, but the variation in zero point between fields. Together, the zero point effects were estimated to contribute on the order of

3% to the fractional error of the GALEX intensity maps in [1]. Given both the several magnitude improvement in the point source limiting magnitude and the 4× increase in mirror area with CASTOR, we thus naively expect photometric zero point error to be $\leq 0.75\%$. However, achieving better than 1% error control is always challenging, and so we will conservatively assume a 1% photometric zero point error. Note that the photometric zero point error dominates the error budget. The most worst case would be the 3% photometric zero point error from GALEX, which would achieve similar constraints to [1].

We also considered a more general model which allows for the growth of photometric errors with redshift. The first term of Equation 3.19 models the dimming of the source at higher redshift. Motivated by the form of this expression, while noting that J_Y and the bolometric flux differ by an additional factor of 1/(1+z), we assume photometric error scales with the flux, which scales with $1/(1+z)^2$. We assume a functional form

$$\sigma_P = A_n(1+z)^2 \tag{3.22}$$

where we take A_n, the noise amplitude, to be approximately the same level as the fixed component of the photometric noise, i.e. 1%. This has the effect of rescaling the errorbars with redshift such that the distribution becomes photometric noise dominated at all redshifts for existing spectroscopic tracer catalogs.

On large scales, the correlation function is limited by the finite number of modes available. However, we use the correlation function only on degree scales, while the tracer survey covers 7000 degrees. We thus expect cosmic variance to contribute only at the 10^{-6} level, negligible in comparison to shot noise and photometric uncertainties [114].

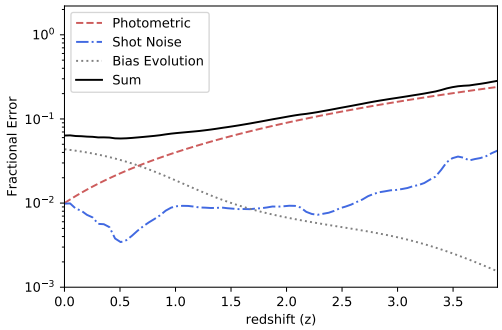

Figure 3.3: Fractional Error as a function of redshift for Model C. Our error model consists of three components, a photometric error, shot noise in the spectroscopic tracer catalog and noise related to systematic error in parameterization of the bias evolution with redshift. Model C incorporates each source of error, while Model O sets a lower limit on the errorbars due to shot noise and a fixed photometric zero point error.

3.4.4 Summary of Error Models and Optimal Spectroscopic Tracer Catalogs

We combine the error sources above into two error models, which bound the upper and lower limits of uncertainty in the precision of a CASTOR measurement.

1. Model O: In this model, we consider only shot noise and fixed photometric zero point. This is consistent with quoted errorbars on clustering redshift estimation in simulations and plotted in Figure 3.2 [105]. Since we seek a lower bound on the total uncertainty, we consider an optimal spectroscopic tracer catalog such that shot noise is always less than a fixed photometric error. This optimal catalog is assumed to have five times the depth but the same distribution as the SDSS catalogs discussed in Section 3.4.1. For comparison, DESI achieves an ≈ 10 fold increase in tracer catalog depth and so will achieve optimal tracer density.

2. Model C: To the errorbars in Model O, we add the effects discussed in Sections 3.4.2 and 3.4.3, that better reflect the errorbars in broadband tomographic measurements found in [1] and

[115]. We assume only the existing spectroscopic catalogs in modeling the shot noise component.

We show Model C in Figure 3.3. Model O (whose evolution with redshift is shown in Figure 3.2) is a lower bound on the error due to fixed additive noise from varying photometry and tracer catalog completeness, while Model C is likely to overestimate the real low redshift error bars owing to its simple parameterization of weakly constrained bias evolution and assumption that photometric errors increase with redshift rather than remaining constant. The fractional error grows with redshift, but not rapidly enough to produce large absolute uncertainties given the decline in the intensity with redshift. Therefore, the signal and the error together go smoothly to zero at high redshift because of the pre-factor in Equation 3.19 and the shape of the filter, regardless of the underlying SED shape that we constrain.

The conservative error estimates we obtain show that the common assumption of 1/N Poisson noise [116] tends to underestimate the true uncertainties. Further, comparison of our analytic approach with bootstrapped errorbars from GALEX in [1] reveals an unaccounted for and redshift dependent term that inflates the error by a factor of 2-3 at $z > 0.7$. Another possibility is unmodeled systematics in the reference catalog, owing to differences in the underlying tracer populations. Although we do not attempt to explicitly model this effect, we expect that it is a consequence of the filter shape, where fewer photons are detected as the emission redshifts out of the filter coverage. A stronger evolution of the photometric error could capture this effect at high redshift at the cost of less agreement at lower redshift where most of our constraining power is expected to be.

To summarize the redshift dependencies of each model. In Model O, shot noise is subdominant to photometric uncertainties which become comparable as the completeness of the spectroscopic tracer catalog falls off at $z > 2.5$. In Model C, at low redshift, error due to bias evolution dominates, while for $z \gtrsim 0.5$, photometric errors grow and dominate over both shot noise and bias evolution.

In the remainder of this work, we will show results from both models. We expect the real

performance to lie somewhere in between.

3.5 CASTOR Results

The bias weighted intensity distribution contains information about both the spectral energy distribution (SED) of the extragalactic background and its overall intensity or monopole term. In Section 3.5.1 we estimate uncertainties on the parameters governing the shape of the SED model and its evolution. In Section 3.5.2 we infer the EBL monopole conditioned on the SED model parameter distribution as a convenient statistic for summarizing measurements of the EBL in a technique independent fashion.

3.5.1 UV-Optical Background Spectral Energy Distribution

To estimate CASTOR's sensitivity to the parameters of the underlying SED model, we write the likelihood of the fiducial model given a vector of model parameters Ψ as

$$p(D|\Psi) = \mathcal{N}\left(\frac{dJ}{dz} b_{im}(\Psi, z), \sigma^2\right) \tag{3.23}$$

where σ^2 is computed by adding the terms in each error model in quadrature. Here, $\mathcal{N}$ indicates the Gaussian normal distribution. The probability that a vector Ψ defines the true underlying model is given by Bayes' theorem.

We assign uniform priors on each parameter with width specified by the marginalized posterior uncertainties in [1]. We sample our likelihood function using the affine-invariant Markov Chain Monte Carlo code, EMCEE [117]. Table 3.5.1 summarizes our fiducial model parameters and their corresponding priors. As mentioned in Section 3.3.1, we do not constrain $\mathrm{EW}_{\mathrm{Ly}\alpha}^{z=0.3}$, since we lack the FUV filter present on GALEX and thus cannot directly observe Lyα emission at low redshift. As the additional and overall redder filter set on CASTOR is not expected to improve constraints

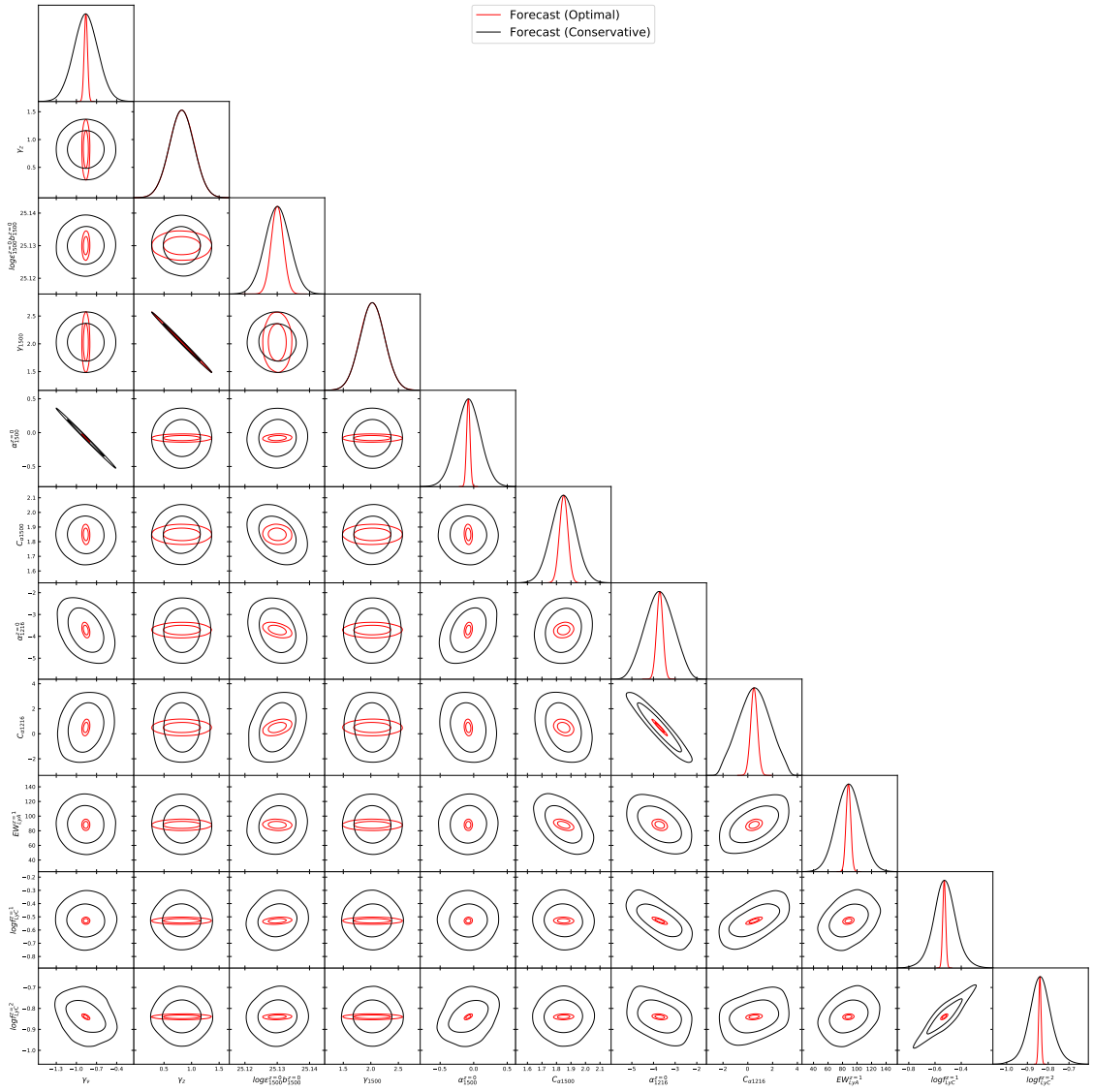

Figure 3.4: From left to right, posterior distributions for the parameters of the SED model γ_ν, γ_z, $\log(\epsilon_{1500}^{z=0} b_{1500}^{z=0})$, γ_{1500}, $\alpha_{1500}^{z=0}$, $C_{\alpha 1500}$, $\alpha_{1216}^{z=0}$, $C_{\alpha 1216}$, $\mathrm{EW}_{Ly\alpha}^{z=1}$, $\log f_{LyC}^{z=1}$, $\log f_{LyC}^{z=2}$. Red contours indicate uncertainties for the optimal error model using a spectroscopic tracer catalog with five times the depth of the SDSS and a fixed photometric uncertainty. Black curves indicate corresponding uncertainties in a conservative error model which adds a redshift dependent photometric uncertainty, bias evolution, and shallower tracer catalog. Diagonal panels show marginalized posteriors for each parameter, while off-diagonal panels show the relationships between model parameters. The geometric mean improvement of the optimal forecast over the conservative model is a factor of ≈ 5 and a factor of ≈ 10 better than GALEX. As discussed in the text, $\log \epsilon_{1500} b_{1500}$, γ_z and γ_{1500} are prior dominated or see minimal improvements with the additional and redder filter coverage.

Table 3.1: Priors on and fiducial values for parameters of the SED model as derived from the best fit parameters and uncertainties in GALEX constraints on the UVB.

Parameter	**Range**	**Type**	**Fiducial**
γ_ν	[-3.44, +0.8]	Flat	-0.86
γ_b	$\sigma = 0.33$	Gaussian	0.79
$\log(\epsilon_{1500} b_{1500}^{z=0})$	$\sigma = 0.01$	Gaussian	25.13
γ_{1500}	$\sigma = 0.30$	Gaussian	2.06
$\alpha_{1500}^{z=0}$	[-1.76, 2.48]	Flat	-0.08
$C_{\alpha 1500}$	[-0.71, +4.29]	Flat	1.85
$\alpha_{1216}^{z=0}$	[-5.67, -1.03]	Flat	-3.71
$C_{\alpha 1216}$	[-2.38, 3.42]	Flat	0.5
$\mathrm{EW}_{Ly\alpha}^{z=1}$	[-9.72, 190.9]	Flat	88.02
$\log f_{LyC}^{z=1}$	<0	Flat	-0.53
$\log f_{LyC}^{z=2}$	<0	Flat	-0.84

on the overall amplitude of the bias weighted intensity normalization at 1500 Å compared to the constraints from GALEX, we place Gaussian priors on $\log(\epsilon_{1500} b_{1500})$, the photon clustering bias evolution with redshift γ_z and the evolution of the 1500 Å normalization $\gamma_{\epsilon 1500}$.

Figure 3.4 shows the 2D contours and 1D marginalized uncertainties for our fiducial model conditioned on the forecasted bias weighted intensities under each error model. These values are summarized in Table 3.2. Our uncertainties are given as the 67% interquartile range relative to the fiducial model parameter.

The parameters governing the evolution with redshift of the frequency evolution and the $1500\mathring{A}$ evolution, γ_b and $\gamma_{\epsilon 1500}$, are coupled because they are only measured via the evolution of the SED amplitude, $\log(\epsilon_{1500} b_{1500})$. Similarly, in the frequency evolution of the normalization, there is a degeneracy between α_{1500}, the evolution of the emissivity with frequency and the frequency dependent clustering bias evolution γ_ν. Since CASTOR NUV is only sensitive to wavelengths greater than rest 1500 Å, a similar degeneracy between the $C_{\alpha 1216}$ and $\alpha_{1216}^{z=0}$ parameters arises. A change in the slope can offset a change in the intercept of the evolution of the emissivity in frequency. Finally, the LyC escape fraction is parameterized by differences in the data constraints from the

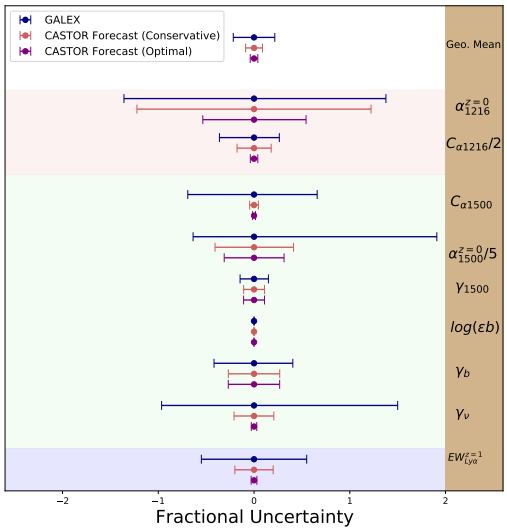

Figure 3.5: Comparison of the posterior fractional uncertainties on the SED model parameters forecasted for CASTOR conservative (red) and optimal (purple) error model to the constraints from GALEX data (blue) in [1]. Parameters in the red region are constrained by the data to $z \approx 4$, in the green region to $z \approx 2.7$, and in the blue region at $z = 1$. Also shown is the geometric mean of the fractional uncertainties for each.

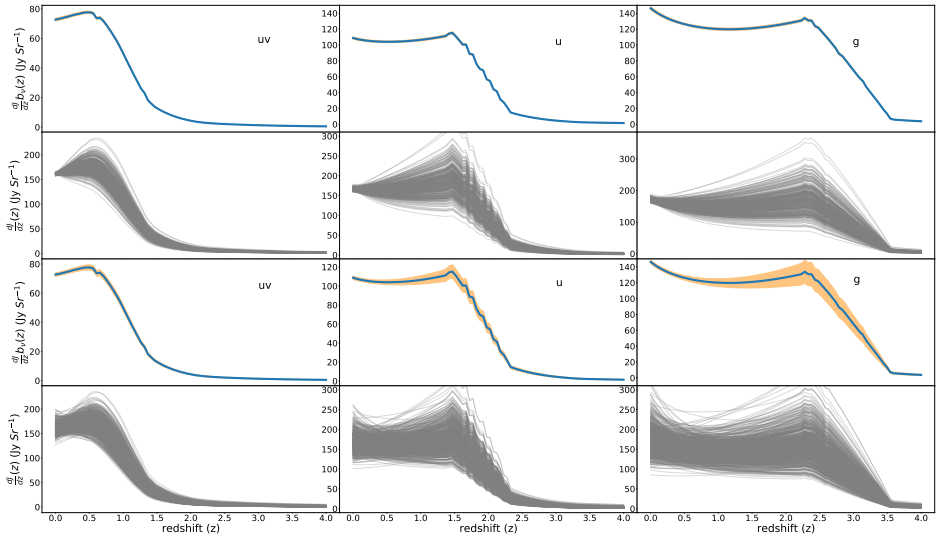

Figure 3.6: First row: The bias weighted specific intensity distribution, $\frac{dJ}{dz} b_{im}(z)$, as a function of redshift for the CASTOR uv imager filters. The shaded region represents the error budget as a function of redshift, determined from our optimal tracer catalog and fixed photometric error. Second row: Intensity distribution in redshift with bias removed and sampling of corresponding fits to the distribution from the SED posteriors. Also indicated is the magnitude of the filter specific EBL monopole. Third row: Same as first row for our second error model incorporating redshift dependent photometric errors, bias evolution, and a combination of existing spectroscopic tracer catalogs. Fourth row: Same as the second row but for the second error model.

Table 3.2: Posteriors interquartile ranges for parameters of the SED model under a conservative and optimal error model. The upper and lower limits are the 67% interquartile range.

Parameter	**Optimal**	**Conservative**
γ_ν	[-0.88, -0.83]	[-1.04, -0.68]
γ_z	[0.60, 1.04]	[0.60, 1.04]
$\log(\epsilon_{1500}^{z=0} b_{1500}^{z=0})$	[25.128, +25.131]	[25.126, +25.133]
$\gamma_{\epsilon 1500}$	[1.81, 2.25]	[1.81, 2.24]
$\alpha_{1500}^{z=0}$	[-0.1, -0.06]	[-0.26, 0.1]
$C_{\alpha 1500}$	[1.82, 1.85]	[1.77, 1.93]
$\alpha_{1216}^{z=0}$	[-3.85, -3.7]	[-4.34, -3.06]
$C_{\alpha 1216}$	[0.23, 0.77]	[-0.77, 1.8]
$\mathrm{EW}_{Ly\alpha}^{z=1}$	[84.90, 91.20]	[71.9, 105.6]
$\log f_{LyC}^{z=1}$	[-0.54, -0.52]	[-0.61, -0.44]
$\log f_{LyC}^{z=2}$	[-0.85, -0.83]	[-0.89, -0.79]
Monopole (uv) Jy/Sr	[300, 403]	[300, 405]
Monopole (u) Jy/Sr	[180, 220]	[180, 221]
Monopole (g) Jy/Sr	[384, 547]	[382, 562]

GALEX filters at $z = 1$ and $z = 2$, leading to degeneracies between the inferred values of $\log f_{\mathrm{LyC}}^{z=2}$ and $\log f_{\mathrm{LyC}}^{z=1}$.

We compare the relative uncertainties from GALEX and both CASTOR error models, along with the range under which that parameter is constrained by the data, in Figure 3.5. These represent competitive or improved uncertainties over those quoted for GALEX with a geometric mean improvement of a factor of 2-3 for the conservative error model and a factor of ≈ 10 for the optimal error model.

In particular, the improved constraints on the 1216 Å continuum slope, which are unconstrained by GALEX, are driven by the deeper redshift coverage of a CASTOR-like survey. Constraints on the parameters of the spectral energy distribution provide additional windows into the ionization and thermal history of the IGM out to $z \approx 3$ that can be compared with constraints at higher redshift.

$\log f_{\mathrm{LyC}}$ at $z = 1$ and $z = 2$ has a $10 - 20\%$ uncertainty in the conservative error model,

and $\approx 1\%$ uncertainty in the optimal model. These constraints offer a window into the UV photon production history at intermediate redshifts. Previous measurements of the total photon budget in the UV favour models for reionization with significant contributions from galaxies, but require large escape fractions [118]. Both observational and theoretical measurements of the escape fraction of ionizing photons from galaxies are poorly constrained. Observational measurements of the escape fraction from $z \approx 3$ galaxies find low escape fractions (< 10 percent) that cannot account for galaxy-driven reionization [119, 120] and escape fractions derived from simulations find wildly varying results [121, 122, 123]. However, if a larger proportion of ionizing photons escape from low luminosity galaxies at high redshift, then the low measured escape fraction in low redshift galaxies can be reconciled with galaxy driven reionization [124, 87]. Although our approach in constraining the escape fraction in this work does not distinguish between diffuse and discrete components, instead modeling the total combined spectral energy distribution, measurements with real data can be decomposed and considered separately by masking sources. This then yields a direct integrated constraints on the sources of diffuse photons to $z \approx 3$.

SED information is captured by differences in the relative filter responses as a function of redshift. In Section 3.4.1 we considered the contribution from deeper tracer catalogs with fixed source distributions as well as improvements in the photometric uncertainties. Since the tracer catalog, and hence shot noise, is redshift dependent, we expect changes in the inferred parameter uncertainties to be driven more by improvements in the spectroscopic tracer catalog than by uniform multiplicative improvements in the photometric noise. We tested this by running additional test chains with a flat error model independent of redshift and one that was a linear function of redshift, finding modest improvements for the latter over the former at fixed mean uncertainty.

In summary, improved uncertainties in model parameters are driven both by the information present in the additional filters and reduction in the cross correlation error bars. The addition of a third filter both appends a third column to our data vector and extends the constraints to higher

redshift. Parameters normalized to their evolution at 1216 Å are constrained to $z \approx 3.5 - 4$, while parameters normalized at 1500 Å are constrained to $z \approx 2.7$. This compares to limiting redshifts on the data constraints of $z < 1$ for GALEX FUV/NUV or the CASTOR uv filter alone.

3.5.2 Total EBL Monopole

The EBL monopole is the leading order contribution to the spherical harmonic decomposition of the EBL. This makes it a convenient summary statistic at a given effective frequency for comparing EBL constraints across a variety of measurement techniques and frequency ranges. Further, beyond being a summary statistic, the EBL monopole intensity at a given effective frequency includes information about a combination of astrophysical emission and cosmic structure [42].

The EBL monopole is determined from the bias weighted intensity distribution functions, $\frac{dJ}{dz} b_{im}(z)$, shown in Figure 3.6 for both error models by integrating Equation 3.19 over redshift from $z = 0$ to $z = z_{max}$ and fixing the redshift dependent photon clustering bias to its fiducial value as determined from the best fit model. Although the photon clustering bias is only measured as a product with the emissivity normalization, it can be obtained in regions where the frequency evolution of the bias is known to be flat and where a discrete source catalog exists [1]. Estimated monopole values and uncertainties are given in Table 3.2. Error bars are determined from 67% inter-quartile ranges on the monopole values determined from the posteriors to the parameter fits, a sampling of which are shown in the lower panels of Figure 3.6.

For our fiducial model, [1] estimates values in the NUV of 172 photons cm^{-2} s^{-1} Hz, while [2] gives lower limits of 171 and 254 photons cm^{-2} s^{-1} Hz in the u and g. The CASTOR uv filter nearly replicates the information present in the NUV filter on GALEX (see Figure 3.1), while the u and g filters extend these constraints into the blue end of the optical. Our forecast EBL monopoles in each filter and their associated $1 - \sigma$ uncertainties determined from the posterior distributions of each model parameter are shown in Figure 3.7. The measured quantity is the extragalactic light

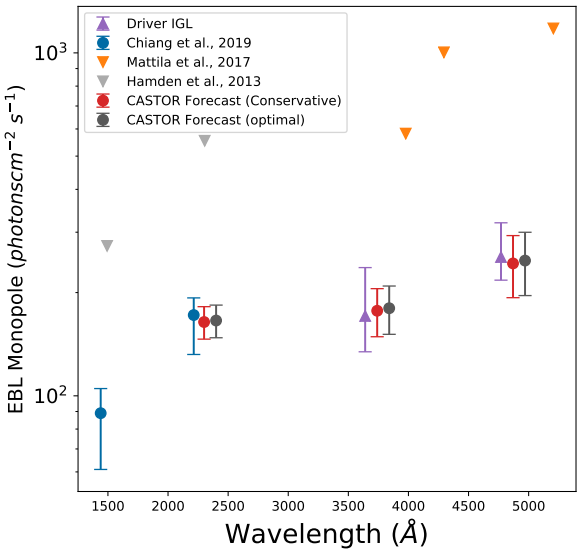

Figure 3.7: Comparison of our forecasted EBL monopole values in the uv, u and g CASTOR filters (red and dark grey bars) to the constraints on the intergalactic light (galaxies + AGN only) from [2] (purple arrows), [3] using a dark cloud technique (orange arrows), the high galactic latitude measurements from [4] (light grey arrows) and the GALEX constraints (blue bars). To facilitate comparison of the uncertainties, we have introduced a 100 Å offset in wavelength. As described in the text, we have also multiplied the CASTOR forecasted values by ≈ 1.4, to better match the existing constraints given differences in the optical depth model.

at the Earth; there is hence a degeneracy between the emitted extragalactic background light and intergalactic medium absorption. The EBL is thus measured up to a function of the mean optical depth $\tau_{\rm eff}$. Our simple analytic model for $\tau_{\rm eff}$ differs from the model of [125], which was used to derive the parameters of the fiducial model in [1], by $20-30\%$. To facilitate a comparison between our forecast and the existing results, we rescale our optical depth model so that the central forecast CASTOR monopole in the uv filter matches the measured value in the GALEX nuv filter. This corresponds to a factor of ≈ 1.4.

We compare our uncertainties on the EBL monopole to existing limits in Figure 3.7. Our

forecasted constraints are shown in red for the conservative model and dark grey for the optimal model. We also include the limits in the u and g derived from COSMOS, HST ERS, and HST UVUDF number and luminosity counts [2], including only extra-galactic contributions from discrete galaxies as purple lower limits. Also shown are constraints from dark cloud measurements [126] as orange upper limits, and observations at high galactic latitudes from [4] as light grey upper limits as they include contributions from both foregrounds and the extragalactic background.

Our error bars are derived under both optimal and conservative error models from the posterior fits to the spectral energy distribution. Both GALEX FUV and CASTOR uv, u, g have uncertainties about a factor of 3 smaller than the New Horizons measurements and comparable to the uncertainties from number count techniques, with the advantage of an unambiguous decomposition into extra-galactic and galactic components. CASTOR's redder filter set extends measurement of the EBL monopole as compared to GALEX. As the EBL monopole is already well constrained in GALEX, and it is not uniquely fixed by the emission redshift distribution, we do not find substantial additional constraining power. Similarly, as the EBL monopole is sensitive to the value of $\gamma_{\epsilon 1500}$ that is not well constrained in either the conservative or optimal error models, there is little change in the uncertainty on the inferred monopole between the two CASTOR scenarios we consider.

Although these constraints are competitive with the current best constraints, we caution that our technique only measures the EBL monopole up to a degeneracy with the photon clustering bias that must be determined independently. This degeneracy can be broken if one has a priori knowledge of the emissivity distribution or, as in [1], a near-flat estimate of the slope of the continuum that produces an integral constraint on the bias normalization. Further, the EBL monopole is estimated only up to a factor dependent on the effective optical depth.

3.6 SPHEREx and LUVOIR

CASTOR is able to constrain the EBL from $z = 0$ to $z \approx 3$ as compared to $z < 1$

for GALEX. Such a measurement is enabled by high redshift spectroscopic catalogs produced by ground based large scale structure surveys (DESI, eBOSS), and would be extended by complementary spectro-photometric observations with SPHEREx at higher redshift and LUVOIR at high spectral resolution.

In this section, we study an extension of our CASTOR models with SPHEREx using a simplified SED model. We then discuss the ability of LUVOIR to carry out a deep UV-optical intensity mapping experiment.

3.6.1 SPHEREx Filters, Error Model, and Results

The SPHEREx instrument is a spectro-photometer based on a series of linear variable filters arranged such that the scan of the telescope across the sky exposes each independently. With accurate pointing knowledge, spectra for each point on the sky are reconstructed. Spectral resolution across the complete band-pass varies and is $R = 35 - 130$.

SPHEREx Lyman-α intensity maps will be produced by observing from $0.75 - 1.2\mu$m with $R = 41$. We can model the spectro-photometer of SPHEREx as a limiting case of a broadband tomographic experiment where one defines a series of narrow-band filters that approximate the response of the spectro-photometer. The conservative instrument can be modelled by a series of 96 filters, however, only the first 19 constrain Lyα over this redshift range. We model these as a series of Gaussians with FWHM set by the spectral resolution.

With 19 effective narrowband photometric filters, inferring the parameters of the conservative rest frame emissivity model discussed in Section 3.3.1 becomes computationally expensive. To mitigate this, we consider only the terms governing emission of Lyα and the Ly continuum observed over this redshift range. We fix all other parameters to their fiducial values. In total, we constrain the bias evolution in frequency and redshift, γ_ν, γ_z, as well as the Ly-continuum slope and evolution parameters α_{1216} and $C_{\alpha 1216}$ and Lyα equivalent width, evolved to its low redshift value, $\mathrm{EW}_{Ly\alpha}^{z=1}$.

Table 3.3: Posterior Interquartile Range on the parameters of a simplified high redshift SED model assuming fractional uncertainties of 5% and 10% for measurement of the bias weighted redshift distribution.

Parameter	**10%**	**5%**	**Fiducial**
γ_ν	[-0.89, -0.83]	[-0.87, -0.85]	-0.86
γ_z	[0.788, 0.792]	[0.789, 0.791]	0.79
$\alpha_{1216}^{z=0}$	[-4.4, -3.02]	[-4.04, -3.38]	-3.71
$C_{\alpha 1216}$	[-0.22 ,1.22]	[0.16, 0.84]	0.5
$EW_{Ly\alpha}^{z=1}$	[38.91 ,138.38]	[60.5, 115.52]	88.02

For CASTOR, existing spectroscopic tracer catalogs and robust estimates of the bias evolution allowed us to place limits on the signal to noise properties of our error budget at the $1-10\%$ level. For SPHEREx, few spectroscopic tracer objects are known at $z > 5$ and future tracer catalog depths (from, e.g., Roman Space Telescope) are only known to within an order of magnitude [127]. The lack of reliable high redshift catalogs and constraints on the bias evolution makes a detailed estimate of the cross correlation errors depend on assumptions about the cosmological stellar mass and survey selection functions at high redshift. Rather than make assumptions about parameters which can vary over an order of magnitude, we instead consider fixed redshift independent fractional errors on estimates of the cross correlation and derive corresponding SED parameter constraints.

We summarize results for SPHEREx in Figure 3.8 for fractional errors of 5% and 10%. The former approximates the average amplitude of the bootstrapped errors in GALEX while the former inflates these to approximate the peak observed noise amplitudes. Marginalized uncertainties are given in Table 3.3 as the 67% interquartile range. Either error model produces 1% level constraints on the frequency and redshift bias evolution, 10% level constraints on the continuum slope, a $30-50\%$ constraint on $EW_{Ly\alpha}^{z=1}$ and constrains the continuum normalization to within an order of magnitude.

The 30% constraint on the Lyα equivalent width provides a window into the population of Lyman α emitters (LAEs) at high redshift (Ouchi2019 and references therein, 1967ApJ...147..868P). Traditional techniques for studying this population rely on identifying individual sources with either

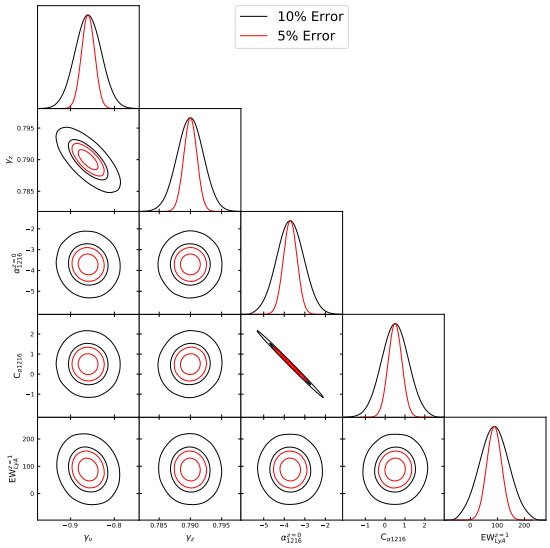

Figure 3.8: Restricted parameter uncertainties on SPHEREx with fractional uncertainties of of 5% and 10%.

narrowband photometry or slitless spectroscopy, both of which suffer from long exposure times on 4-8 meter class telescopes and limit the population of identified LAEs up to $z \approx 8$ to $10^3 - 10^4$ [128]. In contrast, our technique measures the population statistics of Lyα emitters at $z = 5 - 9$ without identifying individual LAEs. Further, comparison of the bias parameters for Lyα sources and high redshift AGN can shed light on the relationship between LAEs and AGN through their environmental dependence [129, 130]. The mass function $n(M)$ and luminosity function $\phi(L)$ are also constrained through their dependence on the total UV photon density $\rho_{\rm UV}$ and escape fraction $f_{\rm esc}$ that we measure through the evolution of the EBL monopole.

Previously, measurements of the rest-UV specific luminosity density and Lyα luminosity density, $\rho_{\rm UV}$ and $\rho_{{\rm Ly}\alpha}$, relied on high resolution spectroscopy. However, we are able to forecast constraints on these at the $10 - 30\%$ level as determined from our posterior distribution for the SED model parameters, assuming our emissivity model can be extrapolated to the higher $z = 5 - 9$ redshift range. This particular redshift range is of interest, as they are expected to evolve rapidly at this epoch. Both $\rho_{\rm UV}$ and $\rho_{{\rm Ly}\alpha}$ can provide direct constraints on the timing and sources of

reionization, so such a measurement overlapping with the expected reionization epoch expected to end around $z \approx 6 - 5.5$ [131, 132, 133, 134] would be of particular interest.

Population synthesis modeling of high redshift LAEs have been challenged by the lack of high signal to noise continuum detection in individual spectra [135, 136]. In contrast to stacking techniques that are challenged by the presence of strong nebular lines, our technique is sensitive only to broadband noise features that are produced systematically across the population of LAEs. The joint analysis of a broadband tomographic measurement of the LAE population and high spectral resolution studies of samples of LAEs would benefit from differences in the underlying systematic uncertainties.

3.6.2 Measuring the UV-Optical Background SED with LUVOIR

In contrast to SPHEREx and CASTOR, the LUMOS instrument on LUVOIR will enable studies of a small number of sources with extremely high spectral resolution [137]. Studies of the IGM and CGM will primarily use background QSOs to study the diffuse sky in absorption from $z = 1 - 2$. Systematic and statistical errors in measurements of absorption constraints on the UV background are summarized in [138], and include uncertainties in the effective optical depth, temperature-overdensity relation, and Jean's smoothing, which affect small scales and require detailed modeling or simulations to estimate. In contrast, our error budget is dominated by large scale effects that evolve with redshift and can be estimated with linear theory.

In addition to the spectroscopic instrument, LUVOIR also has a UV-optical High Definition Imager (HDI) with wavelength coverage from 0.2-2.5 μm. Although a galaxy counting experiment with LUVOIR would have improved depth compared to HST measurements, it would be limited to the component of the UV background which arises directly from discrete components. A diffuse sky measurement similar to GALEX and the one we envision with CASTOR could provide a powerful complement to measurements of discrete sources. Broadband tomography will yield com-

petitive constraints if a large enough area of the sky can be observed such that there is sufficient deep spectroscopic tracer catalog overlap and minimal uncertainties due to cosmic or sample variance. Compared to a large focal plane survey mission, HDI has a field of view of $0.2' \times 0.3'$, about a factor of 150 smaller than the 0.25 deg^2 field of view for the CASTOR imager.

LUVOIR-A is envisioned to have a 15 m primary, while LUVOIR-B would have a more modest 8 m primary, corresponding to factors of 225 and 64 in light gathering power, respectively. Assuming a constant limiting magnitude equivalent for both, an intensity mapping experiment with LUVOIR would then survey an equivalent area with a similar overall exposure time. A 1 month intensity mapping survey with LUVOIR would scan a map of $\approx 100\text{deg}^2$. Such a survey would likely be cosmic variance limited at the 1% level assuming the scalings in [114]. Since only knowledge, but not control, of telescope pointing is required, it is interesting to note that a 6 month survey with the Hubble Space Telescope following gyroscope failure could achieve a similar level of constraining power.

3.7 Conclusions

We have considered the ability of future survey instruments, CASTOR and SPHEREx, and optionally LUVOIR or HST, to extend the constraints from GALEX on the extragalactic component of the optical and UV background light at redshifts $z = 0-3$ and $z = 5-9$. The low redshift regime constrains properties of the UV background and the high redshift regime constrains the timing and sources of reionization. For CASTOR, we have modelled measurement uncertainties with a combination of shot noise from galaxy cross-correlation tracers, photometric errors, and fluctuations in the bias evolution. We consider two error models, a limiting optimal model achievable with future spectroscopic catalogs where shot noise from the tracer catalog is subdominant to photometric errors, and a conservative model intended to bound upper limits on each effect we consider. For SPHEREx, we instead considered fixed total error budgets of 5% and 10%. We derive posterior distributions

on the model parameters for each model and experiment.

For CASTOR, we find a factor of $2-3$ improvement in the geometric mean of the relative errors in parameters of our spectral energy distribution model under conservative and optimistic error models respectively. These constraints are determined from the application of clustering redshift estimation to a future all sky broadband intensity mapping experiment. From the posterior SED fits, we estimated monopole uncertainties for the uv, u and g filters, finding that these constraints are competitive under both error models. SPHEREx would constrain Lyα emission at the $10-30\%$ level from $z=5-9$ and shed light on the population of Lyα emitters at high redshift.

An observed frame UV broadband tomographic measurement with CASTOR intensity maps would represent a significant improvement on current experiments targeting these wavelengths. SPHEREx, by contrast, would constrain the population of Lyman-α emitters at high redshift with observed frame infrared measurements. Intriguingly, LUVOIR's large mirror size compensates for its small field of view and would allow it to place tight limits on the UV-optical SED with a modest investment in observing time. Similarly, since accurate pointing control is not necessary, a larger investment of HST time in a post-gyroscopic failure mode offers a promising extension to this storied mission's history as a photometric intensity mapping experiment.

CASTOR and SPHEREx would yield an improved picture of the low surface brightness universe and total photon budget in two windows, from $z=1-3$ and $z=5-9$. Together, we expect knowledge of the SED at the few percent level, representing a factor of $2-10$ over the current state of the art.

Chapter 4

A Forecast for Large Scale Structure Constraints on Horndeski Gravity with Line Intensity Mapping

4.1 Introduction

The theory of General Relativity (GR) has withstood attempts at revision on theoretical and experimental grounds for more than a century. In light of the non-renormalizability of GR and the need to explain the observed change in the expansion rate of the universe, there is now a rich taxonomy of theories that revise standard GR, including f(R), Horava-Lifshitz, and scalar-tensor theories, for a thorough review, see [75]. Despite stringent experimental limits on deviations from GR on small scales, measurements of the Hubble constant [76, 77, 139], the Cosmic Microwave

Background (CMB; [140]) and Baryonic Acoustic Oscillations (BAO; [141]) all point to an accelerated expansion of the universe. Although the most minimal explanation is arguably a cosmological constant, other potential solutions include a new coupling to the matter sector or a modification of the gravity theory itself.

Astrophysical and cosmological tests of GR are also worth pursuing even if they do not seek to explain the expansion of the Universe, as they are able to probe regimes inaccessible to Solar System probes. Horndeski theories are the most general theories which include a scalar field and have 2nd order equations of motion [79]. They are interesting because they include a number of previously studied classes of model as subcases, including Brans-Dicke, f(R), and Galileon models [80].

Modified gravity effects can be observed both through changes to the background expansion and large-scale geometry, or through measurements of large-scale structure (LSS) that probe changes to the Poisson equation and the physics of galaxy formation and evolution ([142] and references therein). BAO and CMB measurements probe geometry, while lensing, Redshift Space Distortions (RSD), and biased tracers of the matter power spectrum probe structure formation. It is typical to combine multiple probes to improve constraining power and perform consistency checks [143], with specific consistency conditions for Horndeski theories derived in [144, 145]. Measurements of galaxy cluster abundance and the linear growth rate of perturbations have placed limits on modifications to gravity, especially in the dark energy equation of state (w) - linear growth rate parameter (γ) plane (cf. [146, 147]).

As a general framework of modified gravity, Horndeski theories have a variety of operators which can be constrained by different cosmological experiments. In the context of effective field theory parameterizations of modified gravity, [148] find that modified gravity constraints are primarily driven by a large amplitude modification of the ISW in CMB measurements. [149] pursue lensing and clustering constraints on Horndeski model parameters from KiDS + GAMA. [150]

combine measurements of the CMB, RSD and SDSS $P_{\rm m}(k)$ measurements from the LRG catalog to derive constraints on the Horndeski model parameters, with results similarly driven by the large effect of modified gravity parameters at low ℓ in Planck $C_\ell^{\rm TT}$ measurements. However, large uncertainties, especially from galaxy biasing and degeneracies in the measurement of $P_{\rm m}(k)$, limit its constraining power beyond the CMB-only result. In addition, the recent simultaneous detection of gravitational and electromagnetic waves from neutron star mergers constrains the speed of gravity to match the speed of light to high accuracy [151, 152]. Future theoretical work as well as next generation-surveys (e.g., Vera C. Rubin Observatory/Legacy Survey of Space and Time [153], Nancy Grace Roman Space Telescope [154], Euclid [155]) are likely to improve measurements of the matter power spectrum, and will improve constraints subject to uncertainties in the biasing of LSS tracers.

In this paper we will make forecasts for an alternative avenue for constraining modified gravity, based on Line Intensity Mapping (LIM). LIM is a promising technique for constraining both astrophysics and cosmology in large cosmological volumes [6, 85, 156, 8, 39, 157, 32]. LIM uses moderate resolution observations to detect LSS in aggregate by integrating over discrete sources [6]. By using a spectrometer to target a spectral line with known rest-frame wavelength, the redshift of the source emission is known and 3D maps of cosmic structure can be constructed.LIM is particularly advantageous for measuring a wide redshift range, including high redshifts where individual galaxies become too faint to be detected in a traditional galaxy survey. This makes LIM an attractive way to probe the evolution of structure during both the epochs of matter and dark energy domination, and thus provide powerful constraints on modified gravity scenarios.

Numerous atomic and molecular lines are now being targeted by LIM experiments across a wide range of wavelengths. High-redshift measurements of the 21 cm neutral hydrogen spin-flip transition in the intergalactic medium are expected to probe the timing and sources of reionization [158, e.g. HERA], while similar measurements of HI within galaxies at lower redshifts will constrain dark energy [159, 11]. At shorter wavelengths, far-IR lines such as the CO $J \to J-1$ rotational

transitions and the ionized-carbon [CII] fine structure line trace star formation and cold gas, are known to be bright in early galaxies, and are being targeted at redshifts $0 < z < 10$ by instruments observing in the cm-THz range [160, 32, 161, 162, 163, 164, 165]. Finally, lines such as Hα and Lyα are targets for optical LIM experiments; for example, SPHEREx targets galactic astrophysics and reionization [166, 167, 168, 169].

Current and near-future far-IR LIM experiments aim to constrain the star formation rate and galaxy formation history over a wide range of redshifts. Those targeting CO include COPSS [170] and mmIME [171, 172], which have both reported first detections of CO shot noise power, COMAP [161], EXCLAIM [10], YTLA [173] and SPT-SLIM [83]. TIME [174] and CONCERTO target [CII] [175]. Recently the COMAP collaboration has placed upper limits on the CO(1-0) signal at clustering scales [27]. While the first generation of mm-wave LIM experiments will primarily constrain the astrophysics of the emission line, future generations have the potential to deliver competitive constraints on cosmology, including early/dynamical dark energy and neutrino masses [85, 9]. In particular, compact mm-wave spectrometers are now being demonstrated that could enable future surveys with orders of magnitude more sensitivity than current experiments [176].

In this paper, we investigate the constraining power of future ground-based wide-bandwidth mm-wave LIM experiments targeting multiple rotational CO transitions over the redshift range $z \approx 0 - 3$. In addition to large accessible cosmological volumes, this extends constraints on modified gravity to higher redshifts than are available in current large optical surveys. In section 4.2 we review Horndeski gravity and the application to LSS through the matter power spectrum and redshift space distortions. Then, in section 4.3, we introduce the formalism of LSS measurements with LIM. In section 4.4, we investigate the range of accessible scales and required survey integration times to achieve competitive constraints on the linear theory parameters, accounting for the atmosphere, astrophysical continuum, and interloper lines. In section 4.5, we discuss implications of these results. We conclude in section 4.6.

Although modifications to GR generally imply a different expansion history, we assume that all deviations are small and only affect linear structure formation around a ΛCDM background. As such, where necessary, we assume a flat ΛCDM-like cosmology with $h = 0.678$, $\Omega_b h^2 = 0.0224$, $\Omega_c h^2 = 0.12$, and $\Omega_\Lambda = 1 - \Sigma\Omega_i$.

4.2 Horndeski Gravity

Horndeski theories construct a relativistic theory of gravity from a Lagrangian including a metric tensor and a scalar field, and lead to second order equations of motion [79]. In this section, we review the features of Horndeski theory relevant to this work, and refer the interested reader to [80], which develops the formalism employed here, and its application to the Einstein-Boltzmann solver `CLASS` [101] to produce the extended Horndeski in Linear Cosmic Anisotropy Solving System (`HI_CLASS`) [177, 178].

In the linear regime, solving the perturbed Einstein equation allows for the construction of four functions of time, denoted $\alpha_i(t)$, that translate the functional degrees of freedom in the action into four time-dependent parametric degrees of freedom [80]. The Horndeski action, the background relations, and prescriptions for the $\alpha_i(t)$ fully determine the evolution of perturbations in the linear regime and hence LSS. There are 4 functions, two of which are in principle measurable by LIM (α_B and α_M) and two of which are not (α_K and α_T). They have the following physical interpretations:

- α_B encodes mixing between the scalar and metric perturbations that arises from the clustering of the Horndeski scalar field, and appears as perturbations to T_{0i}. $\alpha_B = 0$ in ΛCDM + GR. We treat α_B as a free parameter to be constrained by the LIM experiment.

- α_M rescales the Planck mass, representing a change in the strength of gravity. While a constant rescaling of the strength of gravity does not affect structure formation, its time evolution generates anisotropic stress. Since α_M parameterizes the evolution of the Planck

mass with time, $\alpha_M = 0$ in ΛCDM + GR. We treat α_M as a free parameter to be constrained by the LIM experiment.

- α_K represents perturbations to the energy-momentum tensor $T_{\mu\nu}$ arising directly from the action. These can be thought of as perturbations in an additional fluid connected with the modification to gravity. However, α_K affects only scales close to the cosmological horizon, far larger than those measured by LIM or other LSS probes (for a discussion of this to second order, see [80]). While $\alpha_K = 0$ represents the value in ΛCDM + GR and is therefore a natural choice, we choose $\alpha_K = 1$ to ensure that our models easily satisfy the condition for avoiding ghosts in the scalar mode: $\alpha_K + 3/2\alpha_B^2 > 0$.

- α_T gives the tensor speed excess, potentially inducing anisotropic stress, even in the absence of scalar perturbations. $\alpha_T = 0$ in ΛCDM + GR. We set $\alpha_T = 0$, as it is well constrained by measurements of the speed of gravitational waves [151, 152].

These expressions are implemented in the Einstein-Boltzmann solver Horndeski in Cosmic Linear Anisotropy Solver (`HI_CLASS`), which we use to predict the matter power spectrum $P_{\rm m}(k)$ under an assumed ΛCDM background, and to vary the free functions according to the parameterizations described in the next section.

4.2.1 Parameterizations

In the linear regime of cosmological perturbation theory, we assume that all perturbations are small and taken around a flat background spacetime,

$$ds^2 = -(1 + 2\Psi)dt^2 + (1 + 2\Phi)\delta_{ij}dx^i dx^j, \tag{4.1}$$

where Ψ and Φ are small metric perturbations. In the case of fluid scalar perturbations and general theories of gravity, LSS observations such as the galaxy power spectrum, weak lensing shear field, or RSD probe a small number of combinations of these potentials. In Horndeski theory the potentials

are also complicated functions of the α_i, arbitrary functions that represent the maximal amount of information available from cosmology to constrain the dynamics of this class of models. The evolution of the flat background itself can be determined from the Friedmann equations.

The functional freedom to pick the Horndeski α_i allows any evolution for the background spacetime to be realized. LSS alone cannot pick out either the expansion history or a unique form for the α_i. To reduce this freedom, we begin by first noting that geometric measurements are consistent with the universe being nearly ΛCDM, which we select as our model for the background evolution. Once a background is chosen, it is necessary to define a functional form to parameterize how modifications to gravity evolve with time.

Parameterization I: A natural choice in a nearly-ΛCDM universe is to parameterize the modified gravity effect as proportional to the cosmological constant density, Ω_Λ. As this term grows with redshift, it "turns on" modified gravity effects at late times and during the epoch of dark energy domination. Thus for our first parameterization we assume that α_B and α_M are linear functions of Ω_Λ:

$$\alpha_{B,M} = c_{B,M}\Omega_\Lambda. \tag{4.2}$$

Here we have adopted notation from [150] and [148], and refer to this as Parameterization I.

Parameterization II: To evaluate the sensitivity of our probes to observations at high redshift, we use an alternate parametrization where the effect of gravity modification is linearly proportional to the scale factor [177]. This allows the modified gravity to become important at early times, before the onset of dark energy domination. We thus have

$$\alpha_{B,M} = c_{B,M}a. \tag{4.3}$$

Figure 4.1 shows the relative deviation of the matter power spectrum at a fixed scale ($k = 0.05$ h Mpc^{-1}) as the Planck mass rescaling c_M and braiding c_B parameters are allowed to vary. Large deviations from ΛCDM are possible for extreme values of the α functions. As noted in [150], curves

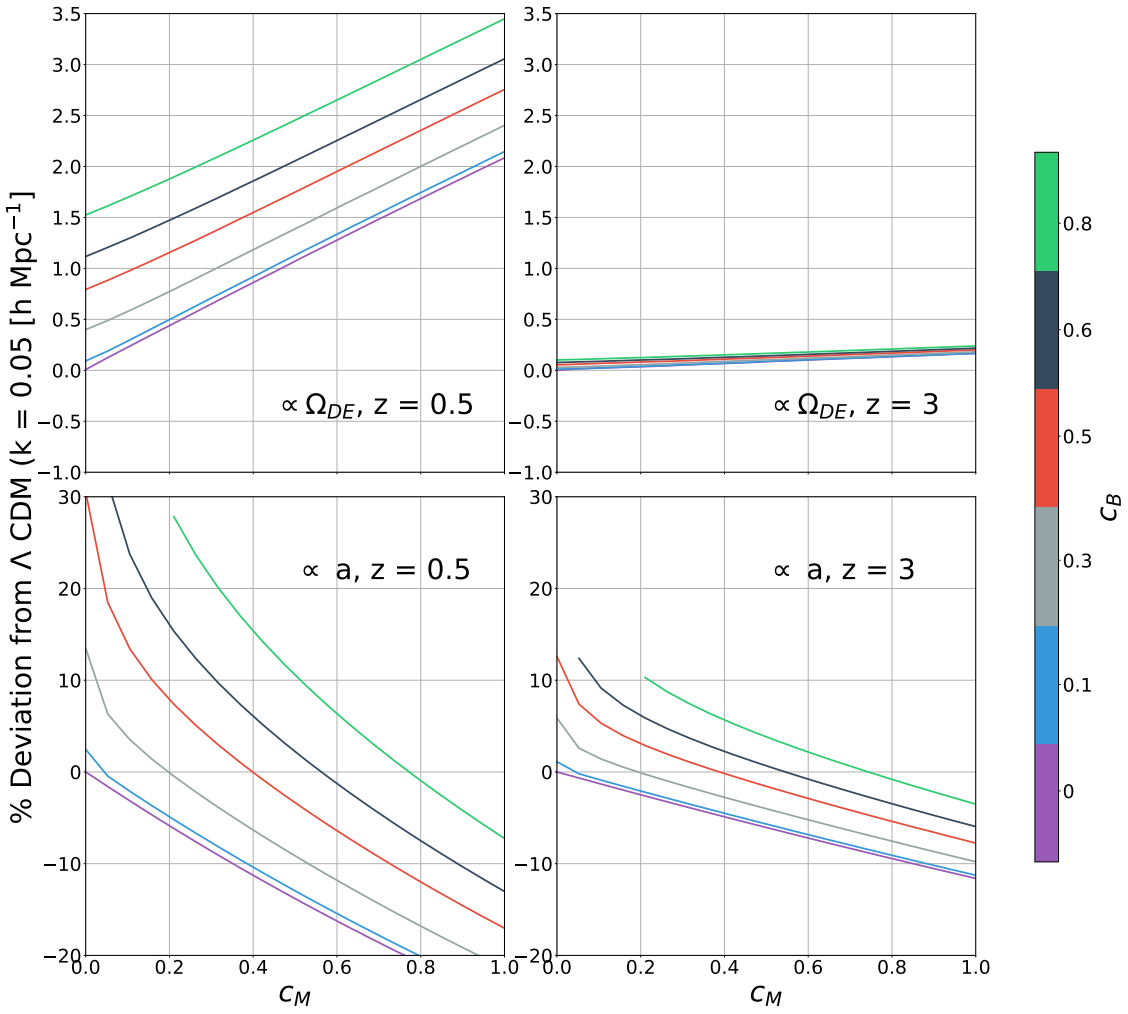

Figure 4.1: Relative deviation of the matter power spectrum for fixed $k = 0.05$ h Mpc^{-1} at $z = 0.5$ (Left) and $z = 3$ (Right) as a function of c_M, with curves labelled by their value of c_B. Top row shows Parametrization I, bottom row shows Parametrization II. The c_B and c_M parameters are allowed to vary over the range $0 - 1$. In Parametrization II ($\alpha_i \propto a$) we have truncated the results due to gradient instabilities when c_M is small and c_B is large.

that intersect the ΛCDM prediction exhibit a degeneracy between c_M and c_B for the matter power spectrum with $c_B \approx 1.8 c_M$ in Parameterization II ($\alpha_i \propto a$). By design, the effect of modifying gravity is largest for the late-time universe, near the end of matter domination. One implication of this evolution is that achieving robust constraints on these linear theory parameters and simultaneously constraining deviations from GR in both parameterizations requires an experiment that targets a large range in redshift.

By selecting a fiducial k-scale to summarize the effects of varying α_M and α_B, we have ignored the k-dependence introduced by the modification to gravity. A well known generic feature of these models is a turnover in the power spectrum, where an excess on large scales becomes a deficit on small scales (with respect to ΛCDM). However, this turnover occurs on scales near the cosmological horizon and is thus extremely difficult to measure with LSS measurements.[1]

At the intermediate scales measured by a LIM experiment, the characteristic feature of modified gravity models relative to ΛCDM + GR is a uniform excess in the power spectrum. The size and behavior with varying c_M, c_B of the effect depends strongly on the choice of parameterization, with a $< 1\%$ difference in ΛCDM at $z = 3$ in Parameterization I and a few percent difference at $z = 0.5$, even for extreme values of the c_M, c_B. The effect of modified gravity on the power spectrum is larger in Parameterization II, approaching instability in the theory when c_M is small and c_B is large. We therefore expect greater sensitivity to the c_M, c_B in Parameterization II than in Parameterization I.

To summarize, we have two modified gravity functions that scale with the background evolution of the spacetime that we seek to constrain. The c_B and c_M parameters govern respectively the evolution of the braiding α_B (clustering of dark energy) and the Planck mass run rate α_M (the large-scale strength of gravity). ΛCDM differs from the models we consider in that the large-scale strength of gravity is fixed and dark energy does not cluster. We assume two functional forms for

[1]The turnover is an unambiguous signature of modified gravity, and would constrain the braiding scale, a function of α_M and α_B.

the scaling of these parameters with the background evolution: one parameterization that scales with the effective dark energy component density Ω_{DE} and one that scales with the scale factor. We fix the remaining two functions to be constant and assign them to unity. We specifically forecast for the uncertainties $\sigma(c_B)$, $\sigma(c_M)$.

4.3 Line Intensity Mapping

In this section we discuss the details of the LIM observables used in our projections. We then discuss experimental effects that limit the scales accessible in the power spectrum, in addition to the effects of interloper lines and Galactic foregrounds.

4.3.1 Line Power Spectrum

Emission lines targeted by LIM experiments originate in galaxies that are biased with respect to the underlying matter overdensity field. On the intermediate and large scales we consider here, outside the nonlinear regime, we can parameterize clustering with a scale-independent clustering bias $b(z)$ that varies with redshift. Since the target lines we consider are correlated with galaxy properties (e.g., star formation rate and metallicity) that evolve with redshift, the line intensity $I(z)$ is also redshift-dependent. The LIM clustering power spectrum is

$$P_{\rm clust}(k,z) = b^2(z) I^2(z) P_{\rm m}(k,z). \tag{4.4}$$

Here $P_{\rm m}(k,z)$ is the underlying matter power spectrum which contains the cosmological information (Section 4.2.1). We show the matter power spectrum for a range of choices of the c_M and c_B in Figure 4.2, and the product of the matter power spectrum normalization and linear growth function, $f(z)\sigma_8(z)$, in Figure 4.3. We assume the bias is scale independent and varies linearly with redshift, $b = (1+z)$.

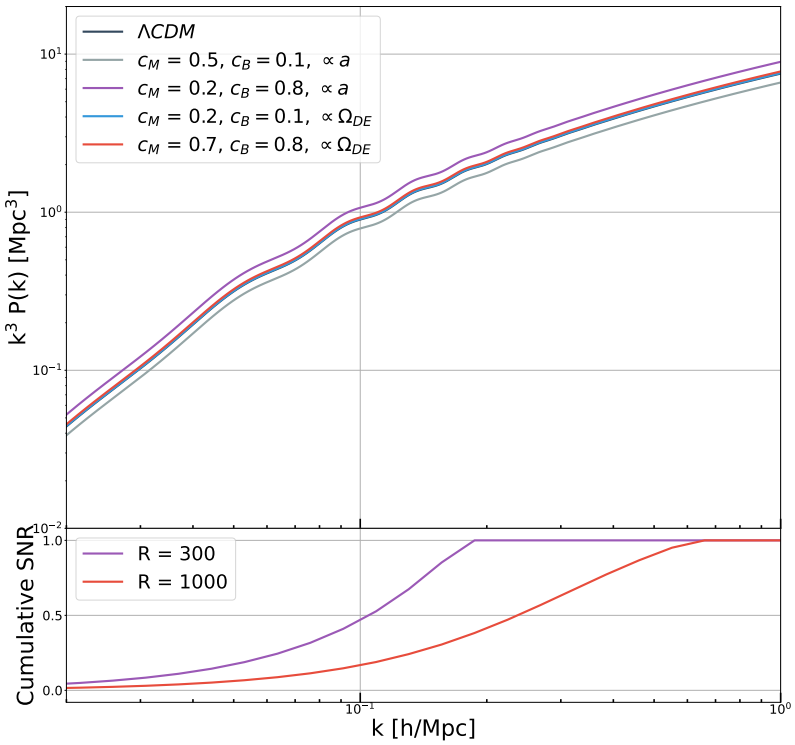

Figure 4.2: Top panel shows the matter power spectrum at $z = 0.5$ in both parameterizations. We have chosen values of c_B and c_M representative of the range of deviations in $P_m(k)$ that we constrain. Bottom panel shows the cumulative constraining power as a function of scale assuming a spectral resolution of $R = 300$ or 1000 in the baseline $f_{\rm sky} = 40\%$ case. The SNR saturates once the scales probed are below the spectral resolution of the LIM experiment. The lower spectral resolution with $R = 300$ causes the SNR to saturate at an larger k than in the $R = 1000$ case.

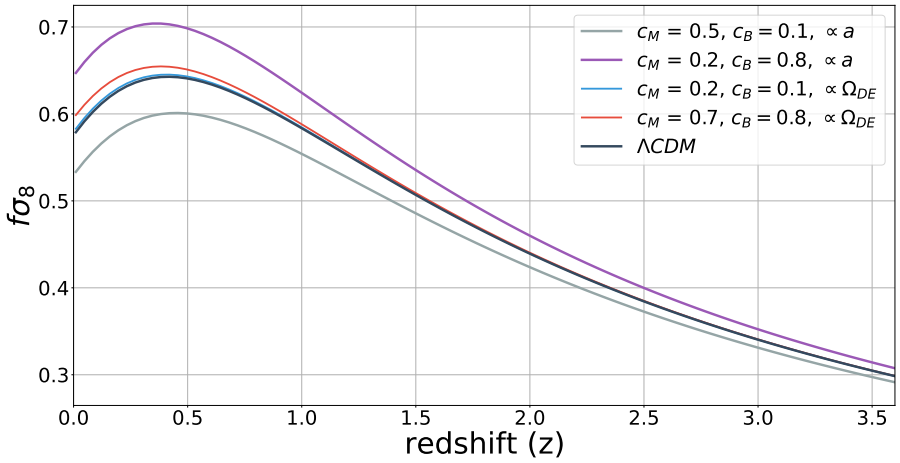

Figure 4.3: Evolution of the power spectrum normalization $f(z)\sigma_8(z)$ over the range of redshifts accessible to the experiment we forecast for. We have also indicated the approximate redshift where the CO(1-0), CO(2-1), and CO(3-2) lines that we target in our forecast are brightest. The evolution of the line brightness differs from that of the power spectrum normalization, both in the peak and evolution with redshift. This allows an experiment that measures LSS at a range of redshifts to disentangle the evolution of a modified gravity effect on $P_{\rm m}(k)$ from that of $I(z)$.

We assume that the line evolution is given by the line models in [179]. Line intensities are estimated from the specific luminosity density $\rho(z)$. Redshift-dependent luminosity densities are a function of the halo mass (dn/dM(M, z)) or line luminosity functions (dn/dL(z)), that are obtained through empirical scaling relations through the dependence of L(M) with SFR(M,z) or SFRD(M,z). In the [179] models, the line luminosities are derived from the Eagle simulation and are uncertain from a factor of a few to ten. For a recent review of line intensity modeling, see [180].

The observable effect of the modification to gravity is a constant excess or deficit in $P_{\rm m}(k)$. The degeneracy between the line intensity, $I(z)$, and the matter power spectrum introduces a degeneracy between the modified gravity effect and the evolution of the bias and line intensity. However, $f(z)\sigma_8(z)$, which controls the power excess on the scales we observe, has a distinctly different form of redshift evolution from the astrophysics-dependent term $I(z)$. Observing a continuing increase relative to the ΛCDM expectation as the line intensity decreases (or vice-versa) as a function of redshift can therefore break this degeneracy, allowing us to potentially recover a signal from modified gravity effects.

A LIM experiment measures the clustering power, shot noise due to the discrete nature of the emitting galaxies, and instrumental noise:

$$P_{\rm obs}(k,z) = P_{\rm clust}(k,z) + P_{\rm shot}(z) + P_{\rm N}. \tag{4.5}$$

The uncertainty in the power spectrum measurement from a LIM experiment depends both on the number of observed modes and on the instrumental noise. We write the number of Fourier modes at a scale k, in bins of width Δk, in a total volume V_s as

$$N_m(k) = \frac{k^2 \Delta k V_s}{4\pi^2} \tag{4.6}$$

and the variance $\sigma(k)$ on a measurement of $P(k)$ at a scale k is

$$\sigma^2(k,z) = \frac{P^2_{\rm obs}(k,z)}{N_m(k)}. \tag{4.7}$$

Estimates for $P_{\rm shot}$ are given in Table 4.1, while estimates of $P_{\rm N}$ are discussed in Section 4.3.3.

4.3.2 Redshift Space Distortions

Observations of LSS are not made in the isotropic comoving space in which the matter power spectrum is defined, but in the 2+1 dimensional space of angles and redshift. Since the redshift of an emitter has components due to both the Hubble flow and its peculiar velocity, the power spectrum in redshift space is distorted relative to comoving space [181].

Because the inferred transverse and line of sight coordinates are affected differently by the RSD, it is necessary to consider the full anisotropic power spectrum in the space of parallel ($k_{||}$) and perpendicular ($k_{\perp}$) modes. The RSD power spectrum can be expressed in (k, μ) coordinates, where the cosine of the angle is denoted $\mu = \hat{z} \cdot \hat{k}$. Then, in the linear plane-parallel approximation, the anisotropic matter power spectrum is

$$P_{\rm obs}(k, \mu, z) = [b(z)^2 I(z)^2 + f(z)^2 I(z)^2 \mu^2]^2 P_{\rm m}(k). \tag{4.8}$$

Here $f(z)$ is the linear growth rate of structure, which is sensitive to modifications of gravity. We show the redshift evolution of $f\sigma_8$ for the range of Horndeski theories we consider in Figure 4.3.

[150] consider constraints on the Horndeski theory parameters c_B and c_M from both anisotropic clustering measurements of the growth factor D in SDSS and $f\sigma_8$ at $z = 0.57$ in the 6dF survey at $z = 0.067$. While the power spectrum adds little constraining power directly, the RSD constraint improves the posterior uncertainties, especially on the c_M parameter, when compared to the CMB-only constraint.

Although one can infer the value of $f\sigma_8$ directly from the full shape of the anistropic matter power spectrum in (k, μ, z) space, it is simpler to consider constraints from the non-vanishing

$\ell = 0, 2, 4$ moments obtained by convolving Eq. 4.8 with the Legendre polynomials $\mathcal{L}_l$:

$$P_l(k) = \frac{2l+1}{2} \int_{-1}^{1} \mathcal{L}_l(\mu) P(k,\mu)\ d\mu \tag{4.9}$$

Explicit expressions for the monopole and quadrupole are

$$\begin{aligned} P_0(k) &= \left(1 + \frac{2}{3}\beta(bI)^2 + \frac{1}{5}(bI)^2\beta^2\right) P_{\rm m}(k) \\ P_2(k) &= \left(\frac{4}{3}(bI)^2\beta + \frac{4}{7}(bI)^2\beta^2\right) P_{\rm m}(k). \end{aligned} \tag{4.10}$$

Here we neglect the $l = 4$ moment since the hexadecapole is both difficult to measure and contains little information not present in the first two multipoles [182]. For consistency with the literature, we also work with $\beta = f/b$ rather than $f\sigma_8$ directly. These expressions allow us to compute the moments of the redshift space distortions from the isotropic power spectrum $P_{\rm m}(k)$. The variance between the multipole moments can be computed explicitly:

$$\mathrm{Cov}_{l,l'}(k) = \frac{(2l+1)(2l'+1)}{N_m} \int_{-1}^{1} L_l(\mu) L_{l'}(\mu) (P_{\rm obs}(k,\mu))^2\ d\mu. \tag{4.11}$$

[183] (eq. C2-C4) gives explicit expressions for $\mathrm{Cov}_{l,l'}$ (where we have here combined their shot noise term with our $P_{\rm N}$ notation). For the monopole:

$$\begin{aligned} \mathrm{Cov}_{0,0}(k) = \frac{2}{N_k}\Bigg[&\left(1 + \frac{4}{3}\beta + \frac{6}{5}\beta^2 + \frac{4}{7}\beta^3 + \frac{1}{9}\beta^4\right) \\ &\times (bI)^2 P_{\rm m}(k)^2 + 2P_{\rm N}\left(1 + \frac{2}{3}\beta + \frac{1}{5}\beta^2\right)(bI)^2 P_{\rm m}(k) + P_{\rm N}^2\Bigg]. \end{aligned} \tag{4.12}$$

For the monopole-quadrupole cross-term:

$$\begin{aligned} \mathrm{Cov}_{0,2}(k) = \frac{2}{N_k}\Bigg[&\left(\frac{8}{3}\beta + \frac{24}{7}\beta^2 + \frac{40}{21}\beta^3 + \frac{40}{99}\beta^4\right) \\ &\times (bI)^2 P_{\rm m}(k)^2 + 2P_{\rm N}\left(\frac{4}{3}\beta + \frac{4}{7}\beta^2\right)(bI)^2 P_{\rm m}(k)\Bigg]. \end{aligned} \tag{4.13}$$

Finally, for the quadrupole:

$$\mathrm{Cov}_{2,2}(k) = \frac{2}{N_k}\Bigg[\left(5 + \frac{220}{21}\beta + \frac{90}{7}\beta^2 + \frac{1700}{231}\beta^3 + \frac{2075}{1287}\beta^4\right) \times (bI)^2 P_{\mathrm{m}}(k)^2 + 2P_{\mathrm{N}}\left(5 + \frac{220}{21}\beta + \frac{30}{7}\beta^2\right)(bI)^2 P_{\mathrm{m}}(k) + 5P_{\mathrm{N}}^2\Bigg]. \quad (4.14)$$

The above expressions are exact in the case of flat P_{N}, and are approximately correct on intermediate and large scales where the finite spatial and spectral resolution induce only small attenuation in the signal.

4.3.3 Target Lines, Redshifts, and Noise Estimates

Our forecasts focus on measuring the LIM power spectrum from $0 < z < 3$, where ground-based CO experiments are most sensitive. In Parametrization I ($\alpha_i \propto \Omega_\Lambda$), the excess near the turnover in the matter power spectrum at $k = 0.01$ is $\sim 1\%$ at $z = 3$, and an order of magnitude larger at $z = 0.5$. The evolution in the effect of modified gravity for Parametrization II ($\alpha \propto a$) is comparable in magnitude, but begins at earlier redshifts, as shown in Figure 4.1.

We consider an experiment measuring the CO J $\rightarrow$ J-1 rotational transitions, which emit at rest-frame frequencies of 115J GHz. CO offers several advantages compared to other LIM targets: it is a known tracer of molecular gas and is therefore indicative of star formation (which peaked at $z \sim 2$), it has been detected in individual galaxies at high redshift using ground-based telescopes observing in the millimeter band, and the multiple transitions allow a wide range of redshifts to be detected in a modest instrumental bandwidth. Our forecasts use the CO line amplitudes from [179].

To detect the CO power spectrum we consider ground-based mm-wave LIM surveys observing roughly from 75–310 GHz. Technology for this frequency range has seen significant recent development for large-format CMB arrays: focal planes featuring dense arrays of background-limited detectors are now common [184], and current instruments have demonstrated wideband optics that

Table 4.1: Line frequencies, target redshifts, $P_{\rm shot}$ estimates, and line temperatures used in this forecast. Unlisted rotational transitions up to CO(9-8) are assumed to contribute interloper power, but are not included as targets as they are an order of magnitude smaller in line brightness temperature.

Line	$\nu_{\rm rest}$ [GHz]	$\nu_{\rm obs}$ [GHz]	z	$P_{\rm shot}$ [μK^2]	Temp [μK]
CO(1-0)	115	95	0.21	2.66	0.14
CO(2-1)	230	95	1.42	8.54	0.75
CO(3-2)	345	95	2.63	2.98	0.60
CO(2-1)	230	150	0.53	81.8	0.24
CO(3-2)	345	150	1.3	100	0.46
CO(3-2)	345	245	0.4	295	0.14

can measure the 1–3 mm band in a single receiver [185]. Current-generation mm-wave spectrometers are significantly larger than their broadband counterparts since they generally use a physically large apparatus (e.g. grating, Fourier Transform, or Fabry-Perot) for spectral separation. However, *on-chip* spectrometer technology is rapidly progressing [186] and instruments are now being planned to demonstrate LIM with dense spectrometer arrays that approach CMB packing efficiency. Our forecasts anticipate that this technology can be scaled over the next ten years in the same manner as CMB instruments leading up to CMB-S4 [187].

The oxygen line at 118 GHz and the water line at 183 GHz naturally divide up the 75–310 GHz mm-wave band into three windows: 75–115 GHz, 120–175 GHz, and 190–310 GHz. We discuss our approach to estimating noise power in Appendix A. To account for the frequency dependence of the line temperature, we calculate an effective redshift and line strength for each target by averaging over the window. Target line frequencies, temperatures, and redshifts are given in Table 4.1. Additional contributions to the noise model are discussed in the following section.

4.3.4 Finite Resolution and Foregrounds

Instrument Resolution

The scales accessible to a LIM experiment are determined by the finite spatial and frequency resolutions. In the frequency direction, the smoothing scale is characterized by the spectrometer resolution $\delta\nu$, while in the transverse direction, the smoothing is a function of the beamwidth θ_b. These correspond to comoving smoothing scales at redshift z in the transverse $\sigma_\perp$ and parallel (to the line of sight) direction $\sigma_{||}$. In the perpendicular (spatial) direction, the smoothing scale is

$$\sigma_\perp = \frac{\theta_b R(z)}{\sqrt{8ln2}}, \tag{4.15}$$

where θ_b is the full width at half maximum of the beam. The smoothing scale in the parallel (frequency) direction is a function of the target frequency, resolution, and the Hubble scale $H(z)$,

$$\sigma_{||} = \frac{c\delta\nu(1+z)}{H(z)\nu_{\rm obs}}. \tag{4.16}$$

The noise power spectrum $P_{\rm N}(k)$ is the product of the white noise level $P_{\rm N}$ and a factor accounting for the finite spectral and spatial resolutions of the instrument,

$$P_{\rm N}(k) = P_{\rm N} e^{k^2\sigma_\perp^2} \int_0^1 d\mu \; e^{\mu^2 k^2 (\sigma_{||}^2 - \sigma_\perp^2)} \tag{4.17}$$

where μ is the cosine of the angle between the wavevector k and the line-of-sight direction, and the integral averages over all such angles μ to yield the spherically-averaged 3D power spectrum. Here we treat the signal $P(k)$ as fixed, while the finite resolution of the survey causes the noise to become inflated at small scales. This differs from the physical situation, in which instruments generally have flat noise properties as a function of k (or its angular counterpart, l), above a scale $l_{\rm knee}$. In fact, it is the inherent signal that is attenuated and not the noise.

Each point in the 2D $k_{||} - k_\perp$ Fourier plane (averaged over the angular directions) has some attenuation factor due to the instrument resolution. The RSD introduce some phase dependence into the signal as structures move in the redshift direction only, that are picked out by the RSD

operator. However, the attenuated 2D noise does not change due to the velocity-induced distortion of the signal. On large and intermediate scales, and for small values of $P_{\rm N}$ the attenuation factor contributes negligibly to the noise on measurements of the multipole moments. This allows us to use Eqs. 4.12 - 4.14 even in the case of finite instrument resolution.

Atmospheric Fluctuations

Atmospheric fluctuations generate scale-dependent noise. A frozen pattern of 2D fluctuations blowing across the field of view at fixed height above the instrument produces a $1/f$ or Kolmogorov spectrum with an approximate form of $P_{\rm N}(\ell) \propto \ell^{-8/3}$. Here we have introduced ℓ, the angular counterpart to k, which is the Fourier transform pair of the angle θ on the sky. Since atmospheric fluctuations are local to the instrument, it is common to express their effects in ℓ rather than through the redshift dependent mapping to k. Since the fluctuations are finite in size, they only affect the largest accessible scales, with the cut-off used to define the parameter $\ell_{\rm knee}$, such that

$$P_{\rm N}(\ell) = P_{\rm N}\left(1 + \left(\frac{\ell}{\ell_{\rm knee}}\right)^{\alpha}\right). \tag{4.18}$$

The values of $\ell_{\rm knee}$ and α are determined empirically from fits to observed band powers at fixed scan rate. In our forecasts we fix $\alpha = -2.8$ and $\ell_{\rm knee} = 200$ to be consistent with measured values from contemporary fast-scanning CMB experiments in temperature [188]. These values are scan strategy-dependent and should be viewed as approximate. Moreover, it is possible that LIM measurements will have improved noise properties due to the ability to excise atmospheric lines in the spectroscopic measurement. Near-future pathfinder experiments will provide more detailed atmospheric characterization suitable for LIM forecasts and better inform estimates of the largest scales at which LIM is sensitive to cosmology.

Interloper Lines

For observations at fixed redshift and target line frequency, line confusion arises because the emission from sources at various redshifts overlaps in observed frequency. Without additional information, observed power at a given target redshift cannot be easily distinguished from power at a different redshift that has the same observed frequency. This effect can be large. For example, for [CII] experiments targeting $z \sim 7$, CO rotational transitions between $z = 0.45$ and $z = 1.8$ act as foregrounds with power larger than the target line. For the low-J transitions of CO that we target, higher rotational transitions are the main source of interloper confusion. To model this scale-dependent effect, we modify the numerator of Eq. 4.7 to

$$\Sigma_i b_i(z) I_i(z) P_{\rm m}(k, z_i) + P_{\rm shot} + P_{\rm N}. \tag{4.19}$$

For the RSD multipoles, we similarly modify Eq. 4.11 to sum over the RSD power spectrum at each redshift,

$$\mathrm{Cov}_{l,l'}(k) = \frac{(2l+1)(2l'+1)}{N_m} \times \int_{-1}^{1} L_l(\mu) L_{l'}(\mu) (\Sigma_i P_{\rm m}(k, \mu, z_i) + P_{\rm N})^2 \, d\mu. \tag{4.20}$$

In other words, we assume that the interloper power adds to the noise, and does not contribute signal to the estimate of $P_{\rm m}(k, z_i)$. In fact, the interloper contributions themselves carry cosmological information similar to the information that we will consider from the brightest lines. For example, in a wideband experiment observing a large range in redshift and different rotational CO transitions simultaneously, internal cross-correlations may be able to extract the underlying matter power spectrum from each CO line and add them coherently to the signal.

A wide variety of techniques has been proposed for interloper deconfusion. For surveys targeting higher redshifts, masking techniques—i.e., removing brighter pixels that are more likely to come from lower redshifts [164, 189], or using an external catalog of bright interloping galaxies [190]) can significantly reduce the interloper contribution. Cross-correlations between lines can also

reconstruct a high percentage of the true underlying map [182, 22]. Finally, geometric tests for interloper deconfusion were introduced in [165] and [38].

Galactic Continuum Foregrounds

Galactic continuum emission can be a significant foreground for both CMB and LIM experiments. For CO, thermal dust can significantly eclipse the line brightness temperatures at frequencies above 50 GHz while non-thermal synchrotron emission dominates at lower frequencies. By fitting a smooth, low-order polynomial to a foreground that slowly varies in frequency, this can be subtracted and removed, leaving only the underlying cosmological signal. However, residuals from fitting these broadband terms can lead to spuriously inferred excess matter power at large scales that is a function of the residuals after continuum subtraction [37].

We used NBODYKIT to combine the linear matter power spectrum with the Galactic dust continuum, and studied recovery of the power spectrum. We began by adding a mock LIM signal to a typical Galactic dust spectrum, and then removed a series of low-order polynomials. We find that even under pessimistic assumptions, foreground removal only affects large scales ($k \sim 10^{-3}$ h/Mpc) that contribute little weight to the overall constraint (due to the small number of available modes), and which are additionally impacted by atmospheric noise. In a simple but more realistic model for the continuum fitting, the difference between the input and recovered spectrum is less than 1% on intermediate scales. We therefore neglect galactic continuum foregrounds in our forecast.

4.4 Results

In this section, we review the Fisher Matrix formalism used to derive constraints, and describe the specifics of the survey we forecast, motivated by the relevant scales needed to constrain modified gravity. We then present constraints for a future mm-wave LIM experiment as a function of sensitivity, and account for various systematic effects.

4.4.1 Fisher Matrix Formalism

Fisher matrix methods are a standard way of estimating the precision of future experiments [191]. Beginning from an assumption of Gaussian errors, by Taylor expanding about the true parameter values, we have

$$\exp\left(-\frac{1}{2}\chi^2\right) \propto \exp\left(-\frac{1}{2}F_{jk}\delta p_j \delta p_k\right) \tag{4.21}$$

where the matrix F_{jk} is called the Fisher matrix, and can be evaluated as

$$F_{jk} = \sum_b \frac{N_b}{\sigma_b^2}\frac{\delta f_b}{\delta p_j}\frac{\delta f_b}{\delta p_k}. \tag{4.22}$$

The Fisher matrix is equivalent to the inverse of the covariance matrix. Equation 4.22 instructs us to estimate the covariance matrix by computing derivatives of the observable quantity in bins labelled by b and with corresponding error σ_b. Inverting F_{jk} then yields the variance and covariance of the model parameters. In our case, we use the binned power spectrum, $P_b(k)$, and estimate the error per bin σ_b using Equations 4.7, 4.17, and 4.19. An explicit expression of the Fisher matrix in terms of the modified gravity parameters is

$$F_{M,B} = \sum_k \frac{N_k}{\sigma_k^2}\frac{\delta P(k)}{\delta c_{M,B}}\frac{\delta P(k)}{\delta c_{M,B}}. \tag{4.23}$$

Equation 4.22 is sufficient for estimating the covariance in the c_B and c_M parameters from a single measurement of the power spectrum. In the case where multiple emission lines are independently used to constrain the power spectrum shape, the combined Fisher matrix is given by the sum of the independent Fisher matrices for each line, $F^{A+B} = F^A + F^B$.

As the RSD multipole moments are not statistically independent, we compute the joint constraint from the full covariance matrix:

$$F_{M,B} = \sum_k \sum_{l,l'} \frac{\delta P_l(k)}{\delta c_{M,B}} C_{l,l'} \frac{\delta P_{l'}(k)}{\delta c_{M,B}}, \tag{4.24}$$

where l, l' run over the 0 and 2 RSD multipole moments.

4.4.2 Survey Definition and Accessible Scales

Constraints on the modified gravity models considered here will search for a *nearly scale-invariant change* in the matter power spectrum from ΛCDM for $k \gtrsim 10^{-2}$ h/Mpc. This implies that the astrophysical line emission terms in Eq. 4.4 need to be known to better than the ∼few % deviations in $P_{\rm m}$ that we are considering. A LIM survey's sensitivity to the power spectrum falls off at the largest scales due to foreground filtering, atmospheric noise, and the decreasing number of Fourier modes in a finite survey volume. A heuristic for the sensitivity of a survey to an observable, e.g. the matter power spectrum on a given k-scale, is to count the number of accessible modes accessible at that scale.

The number of observable modes can be improved by increasing either the spectral or angular resolution or survey sky fraction. The LIM surveys we consider here are mismatched in angular and spectral resolution; while the arcminute scales accessible with 5–10m class dishes correspond to $k \sim 1 - 10$ h/Mpc, current mm-wave spectrometers have only been demonstrated up to $R \sim 300$ corresponding to $k \sim 0.2$. However, a factor of ∼several improvement in resolution should be possible with technology developments in the near future. In Fig. 4.2 we show the matter power spectrum ($k^3 P_{\rm m}(k)$) and cumulative signal-to-noise ratio on the power spectrum deviation as a function of k for representative values of c_M, c_B in both parameterizations at $z = 0.5$, focusing on the difference between the $R = \frac{\delta\nu}{\nu} = 300$ and 1000 cases. Increasing the spectral resolution increases the number of modes in the survey, leading to improved sensitivity even when a survey is unable to resolve the smallest scale structures. Most of the constraining power in the $R = 300$ case occurs around $k \sim 0.1$ h/Mpc, due to the larger number of modes after accounting for both the spectral resolution and number of modes contained in the survey volume. The scale at which non-linear growth affects the power spectrum at the 2% level is $k \sim 0.1$ h/Mpc at $z \approx 0$, and $k \sim 0.25$ h/Mpc at $z = 3$ (the mean redshift of the lines considered is shown in Table 4.1). Thus for $R = 1000$ about 50% of the constraining power comes from weakly non-linear scales. The exact level of non-linear

growth expected in Horndeski gravity is uncertain, but experiments with `HALOFIT` [192] suggest a moderate increase in the matter power spectrum, and thus moderately improved sensitivity. To be conservative, we assume the predictions of linear theory. Another source of non-linear biasing is the relationship between CO emissivity and dark matter power, which depends on the CO luminosity function [32] and exhibits non-linear effects at $k \sim 0.2$ h/Mpc [193]. The remaining uncertainties in the scale at which nonlinear biasing becomes important will be decreased with future small-scale detection of CO shot noise.

As a baseline survey definition, we consider a survey over 40% of the sky observing 75–310 GHz with $R = 300$. The sky fraction is set in part by the physical limits of telescopes and optics that often restrict observing to elevation angles $\geq$ 40-50 deg. Bright emission from the Galactic center can further restrict accessible sky fractions by another $\approx 10\%$. This survey geometry corresponds to a range of accessible scales between $\approx 2 \times 10^{-3} \leq k \leq 5 \times 10^{-1}$ h/Mpc. The maximum scale is set by the resolution in the frequency direction while the minimum scale is set by the assumed sky fraction. Increasing the sky fraction to 70% improves access to the largest scales by about a factor of two, while the smallest scales remain limited by the resolution in the frequency direction. Atmospheric and galactic thermal continuum foregrounds can also limit sensitivity to the largest scale modes.

Fixing the sky fraction and bandwidth allows us to make the estimates of the noise power given in Table 4.1. The white noise contribution arises from incident photon power from the atmosphere, telescope, and detector (Equations A.1, A.2). Within each of the mm-wave atmospheric windows ($\approx$ 75–115, 125–175, and 180–310 GHz), we use an effective NET in which all of the frequency channels within each band are nverse variance weighted. We then calculate the voxel volume using Equation A.4 for the minimum spatial and frequency scales, set by the telescope's angular resolution and spectrometer spectral resolution, respectively. We convert between NET and integration time via Equation A.3.

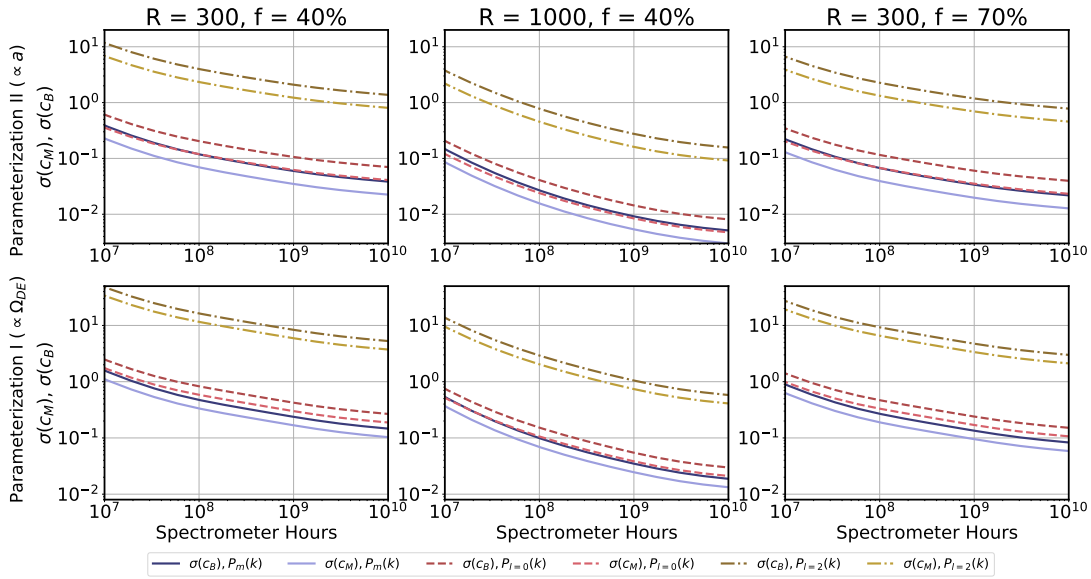

Figure 4.4: Sensitivity to the c_M, c_B parameters from the matter power spectrum or redshift space distortion monopole differs by a factor of ≈ 2 independent of spectral resolution or sky fraction. Here we show forecasted sensitivity (posterior width) as a function of spectrometer hours for the c_M and c_B parameters in the baseline ($R = 300$, $f_{\rm sky} = 40\%$), increased spectral resolution ($R = 1000$, $f_{\rm sky} = 40\%$), and increased survey volume ($R = 300$, $f_{\rm sky} = 70\%$) cases. Top panels are for Parameterization II and the bottom panel is for Parameterization I.

4.4.3 Fiducial Analysis

For our fiducial survey, we assume the experiment described in the previous section, with $R = 300$ spectral resolution and $f_{\rm sky} = 40\%$. In Table 4.1 we summarize our target lines, redshifts, and shot noise estimates. Combined constraints are obtained by summing the Fisher matrices over the full bandwidth, assuming statistical independence of each target line and redshift. We focus on the effects of survey definition for the sensitivity of the baseline survey to c_M, c_B, leaving the effects of interlopers and atmospheric foregrounds for the next section.

Figure 4.4 shows the 1σ posterior widths, $\sigma(c_b)$ and $\sigma(c_M)$, in Parameterization II ($\alpha_i \propto a$, top row) and Parameterization I ($\alpha_i \propto \Omega_\Lambda$, bottom row), as a function of *spectrometer-hours*, the

product of the number of spectrometers and integration time. In addition to the matter power spectrum constraint, we also show the results from the RSD power spectrum monopole and quadrupole separately. The fiducial experiment ($f_{\rm sky} = 40\%, R = 300$) achieves similar sensitivity to the RSD monopole and matter power spectrum, while the quadrupole is significantly less constraining [182].

Sensitivity can be improved by increasing the number of modes through larger survey volumes or improved spectral resolution. In the center and right panels of Figure 4.4, we forecast for increasing the spectral resolution from $R = 300$ to $R = 1000$ at fixed sky fraction, and for increasing the sky fraction from $f_{\rm sky} = 40\%$ to $f_{\rm sky} = 70\%$. We find a factor of a few improvement in sensitivity, achieving a ± 0.1 level constraint on each of the c_B, c_M in Parameterization II at 10^8 spectrometer-hours, with improved sensitivity with longer integration times in both the $R = 1000$ and $f_{\rm sky} = 70\%$ experiments.

Increasing the spectral resolution provides larger returns on sensitivity than going to higher sky fractions at fixed spectrometer-hours, with sensitivity approaching the ± 0.01 level in $\approx 10^8$ spectrometer hours. However, this result depends on the assumed shot noise for each target line. In a test where the shot noise was assumed to take its $z = 2$ values from [9], sensitivity saturates near ± 0.1 at 10^8 spectrometer-hours in the $R = 1000$ experiment in both parameterizations. Less sensitivity to the c_M, c_B is achieved in Parameterization I, regardless of survey definition.

4.4.4 Accounting for Interlopers and Low-Frequency Noise

In order to quantify the effect of different analysis choices on sensitivity to the power spectrum, we now consider the impact that interlopers and low-frequency noise have on measurements of the c_M and, c_B parameters. We begin by modifying the fiducial analysis and baseline survey according to the discussion in Section 4.3.3. Both the survey geometry and atmospheric scale limit the maximum accessible scales. Since the signal to noise ratio on measurements of the power spectrum decreases significantly on the largest scales, the atmospheric parameters ℓ and α will only signifi-

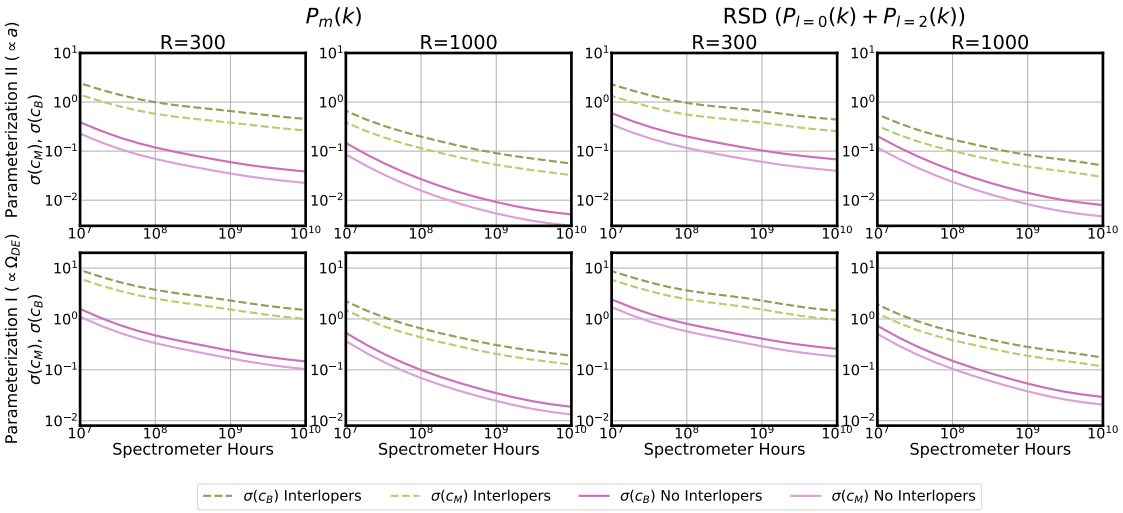

Figure 4.5: Including interlopers leads to a decrease in sensitivity both from $P_{\rm m}(k)$ and the sum of $P_{l=0}(k)+P_{l=2}(k)$, with a reduced sensitivity gap for the redshift space measurements. As before, we plot forecasted sensitivity (posterior width) as a function of spectrometer hours for the c_M and c_B parameters when interlopers are included or excluded in the baseline survey. Left panels show sensitivity from the matter power spectrum, right panels for RSD multipoles. Top panels show Parameterization II, bottom panels show Parameterization I.

cantly impact the constraint if they differ substantially from the scale set by the survey geometry. As discussed in Section 4.3.4, we assume that the atmospheric noise will be similar to that observed at the South Pole. As the relevant observable scales are above ℓ (see Figure 4.2) the choice of ℓ has little impact on our results.

We further consider the effect of interloper lines that mimic redshift dependent intensity fluctuations and therefore pose a potentially more serious problem. Interlopers can mimic a modified gravity effect, since at fixed redshift a change in the intensity bias is degenerate with a change in the growth function. In Figure 4.5, we plot the sensitivity as a function of spectrometer-hours for both the baseline case ($f_{\rm sky} = 40\%, R = 300$) and a case including interlopers and low frequency noise. We treat the interlopers following Section 4.3.4, where interloper lines are assumed to contribute noise but not signal to the measurement of the modified gravity parameters. Here we consider the sensitivity from $P_{\rm m}(k)$ and the sum of $P_{l=0}(k)$ and $P_{l=2}(k)$ computed using Equations 4.12 to 4.14 and 4.24. Interlopers are treated as in Equation 4.20.

The inclusion of interlopers can significantly reduce constraining power. While we obtain ± 0.1 level constraints in the fidicial survey for Parameterization II in 10^8 spectrometer hours, this now requires 10^9 spectrometer hours or more. In Parameterization I, a ± 0.1 constraint is no longer obtained in our range of spectrometer-hours. While such a measurement would still allow for characterization of the size of modified gravity effect over a range in redshift, an interloper-contaminated LIM measurement would add only a very limited amount of information as compared to the existing CMB and LSS measurements.

When there is clean separation between interloper and target lines (the "interloper free" baseline case), $P_{\rm m}(k)$ is more sensitive to the values of the c_M, c_B than the sum of the information from $P_{l=0}(k)$ and $P_{l=2}(k)$. However, in the case of poor line separation, this situation is reversed, where the RSD multipole moments retain more of the sensitivity that is lost in the matter power spectrum. That is, the difference between the interloper and interloper-free cases is smaller. This result is anticipated by the close relationship between Alcock-Paczynski tests, which can be used to achieve line separation, and the redshift space distortion. The two effects are degenerate with the matter power spectrum, and require an assumed background cosmology to fully isolate from one another [194]. The degree of line seperation working in redshift space depends on the linear growth factor f and ratios of volumes between the target and interloper line redshifts.

The two cases we have considered here (foreground/interloper-free and interloper-contaminated) roughly bound the range of expected sensitivity. The interloper-contaminated case we have considered is unrealistically pessimistic, where no attempt is made to remove interlopers before performing a cosmological analysis. Numerous techniques have been proposed in the literature for reducing their contributions (see Section 4.3.4). Although outside the scope of this work, one complication for LIM measurements of modified gravity is that several interloper mitigation schemes (e.g., geometric methods) depend on an assumed near-ΛCDM expansion history. Fully quantifying the effect of various assumptions on the recovery of the signatures of modified gravity is left for future work.

4.5 Discussion

The observable signature of Horndeski gravity on LSS is a scale-independent change in the normalisation of the matter power spectrum for $k > 10^{-3}$ h/Mpc, observable in either comoving or redshift space.

[150] found that the inclusion of $f\sigma_8$ from BOSS DR11 CMASS and 6dF led to increased sensitivity relative to the CMB-only and CMB + mPk cases. We therefore also forecast for an experiment targeting the RSD monopole and quadrupole, which carry information about the velocity field. We find similar sensitivity to c_B, c_M from combining the first two moments of the RSD power spectrum and the matter power spectrum alone. Consistent with the expectations from [182], the quadrupole contributes limited sensitivity compared to the monopole-only result. This is because the uncertainties on the quadrupole power spectrum are a factor of $\approx \sqrt{2l+1}/2$ larger than the uncertainties on the monopole. We assume fiducial models for the line biases and temperatures as discussed in Section 4.3.1 under the assumption that both will be well constrained by future experiments, for example, through multiple-line cross correlations or via cross-correlation with galaxy surveys [182].

Unmitigated interloper emission can reduce the sensitivity at fixed integration time by roughly an order of magnitude. This is expected since the primary effect of modifying gravity in our parameterizations mimics a change to the growth function with redshift. As interloper lines add noise power from a range of redshifts, this adds scatter to the inferred growth function, or equivalently the overall amplitude of the power spectrum on a range of scales.

The inclusion of interlopers in our baseline surveys leads to a reduction in sensitivity to the Horndeski linear theory α functions. We expect the sensitivity of a future experiment to lie somewhere between the no interlopers and interlopers cases shown in Figure 4.5. Although a large number of methods to mitigate the effect of interlopers on cosmological analyses have been studied in the literature, this motivates future work to understand how interlopers may bias future

measurements in cosmology.

A LIM experiment will produce a set of redshift-dependent power spectrum amplitudes that are weighted by the line temperatures and bias factors. Under a fixed background cosmology and assumed evolution of the line intensities, internal and external cross correlations can be used to both disentangle the interloper contributions and significantly reduce degeneracies between the astrophysics- and cosmology-dependent terms.

Our constraints make use of only the average line intensity across the target band and not its redshift evolution. However, the line intensity is expected to trace star formation and therefore peak at $z \approx 2$, while the modified gravity power spectrum excess is expected to grow monotonically with redshift. Therefore, the evolution of the two effects is expected to generically differ with an overall change in the line evolution as compared to ΛCDM. This provides another potential avenue for a LIM experiment to probe modified gravity directly from the redshift evolution. Making use of this information will require improvements in our understanding of the line evolution ($I(z)$) models and scaling relations that link these models to the SFR.

While direct constraints on Horndeski gravity from galaxy surveys have been challenged by limited cosmological volumes and uncertainty in the galaxy bias, next-generation galaxy surveys will probe larger volumes, allowing for joint analysis and cross-correlations that can break degeneracies between multiple probes. Galaxy-LIM cross correlations and multi-line LIM cross correlations, for example, can separate the line bias and intensities even in the presence of interlopers [7].

4.6 Conclusions

In this work, we investigated the ability of a wide-bandwidth ground-based LIM experiment targeting rotational CO transitions to constrain the linear theory parameters of Horndeski models. We consider two parameterizations for the evolution of these parameters, governing the braiding and running of the Planck mass, where both are allowed to evolve with the effective dark

energy density Ω_{DE} or with the scale factor a. Both parameterizations predict larger effects at low redshift, with excesses in apparent power at small scales and deficits in power at large scales for a large part of this 2D parameter space.

With observations in three atmospheric bands from 75–310 GHz, we find that the bright rotational CO transitions from redshifts 0–3 yield posterior widths for these parameters approaching the sensitivity of CMB and existing galaxy survey constraints at 10^8–10^9 spectrometer-hours. This result is robust to the presence of continuum foreground and atmospheric effects, being primarily driven by information obtained from intermediate scales and therefore mainly limited by the degree of interloper contamination. Models in which the modified gravity effect is proportional to the scale factor rather than Ω_{DE} yield constraints that are about an order of magnitude larger at fixed integration time, a result that is consistent with past measurements. There is significant uncertainty about what limits the sensitivity of future experiments in the space of noise, astrophysical, and cosmological modeling uncertainties, and our results should therefore be viewed as a preliminary estimate of the performance of a real instrument. Nonetheless, these results show that future LIM experiments could place competitive constraints on the space of modified gravity theories.

Horndeski theories represent a general class of modified gravity models that add scalar-coupled terms to the gravitational Lagrangian. As discussed in [80], measuring values of the α functions therefore constrains the parameter space of viable modifications to General Relativity. These include metric f(R), Kinetic Gravity Braiding, Galileon, Brans-Dicke, Palantini, and Gauss-Bonnet models.

LIM experiments with CMB heritage could potentially reach 10^8–10^9 spectrometer hours over the next 10–15 years. On similar timescales, space-based spectro-polarimeters operating in the far-IR are expected to become feasible [179]. A space-based instrument would trade angular spatial resolution for increased sensitivity to the integrated line emission through wider bandwidth and reduced large scale noise due to a lack of atmosphere. Combined with a larger $f_{\rm sky}$, this would

enable a range of complementary CMB and galaxy cluster science. As the signature of a modified gravity effect is largely scale-independent on intermediate scales, such an experiment would be able to improve constraints on deviations from General Relativity through both direct measurement of the matter power spectrum and through multi-tracer analyses similar to the one we consider here.

Measurement of modified gravity effects will require improvements in our knowledge of target line biases and intensities to break parameter degeneracies. While analysis and modeling methods for LIM remain in their infancy compared to well developed-methods for CMB and galaxy survey measurements, LIM experiments targeting rotational CO benefit from both this heritage and bright line temperatures. This makes these transitions promising targets for constraining modified gravity theories. Our results show that future LIM experiments can achieve constraints on the linear parameters of Horndeski theories that are competitive with the current state of the art.

Chapter 5

Conclusions and Future Work

Photometric and Spectroscopic Intensity Mapping are techniques for studying the aggregate large scale properties of the universe by measuring very large cosmological volumes. Chapter 3 of this dissertation has investigated the ability of a next generation UV survey satellite, the Cosmological Advanced Survey Telescope for Optical-UV Research (CASTOR), and an infrared Spectro-photometric experiment, the Spectro-Photometer (SPHEREx), to measure the astrophysics responsible for the production of UV and optical photons. Chapter 4 of this dissertation then investigated the ability of future all sky spectroscopic or line intensity mapping experiments to measure deviations from Einstein's theory of General Relativity and to use those deviations to constrain the Horndeski family of gravity theories. Major conclusions of this work can be summarized as follows,

1. CASTOR can measure the UV-optical portion of the EBL at redshifts 0-3, producing approximately 10% level measurements of the parameters of theoretical models for the UV-EBL.
2. SPHEREx can extend these constraints, targeting rest Ly-alpha, that has been redshifted into the IR in the observed frame, from redshifts z=5-9.
3. A future LIM experiment targeting the rotational CO J $\rightarrow$ J-1 transitions from z $\approx$ 0-3 can measure deviations from Einstein's theory of General Relativity through a constant excess

in the observed matter and redshift space power spectra on intermediate scales. Such a measurement is degenerate with the line bias and intensity, but can be disentangled through a measurement of the redshift dependent line evolution that differs in shape.

4. For a LIM experiment achieving $10^8 - 10^9$ detector hours, a constraint on the parameters of Horndeski models of large scale structure governing the large scale strength of gravity and the clustering of dark energy, we forecast constraints at the ± 0.1 level.

5. We find that this result is insensitive to choices about the inclusion of various noise sources and systematics, including galactic and atmospheric foregrounds. Interlopers are a more serious problem future LIM experiments to modified gravity theories, reducing sensitivity at fixed number of spectrometer hours by about an order of magnitude.

6. These results are based on linear cosmological perturbation theory and neglect higher order correlations, including in the line luminosity functions that may introduce additional noise sources not considered here. They depend on the ability to disentangle the evolution of target lines, as well as interloper line confusion, from the underlying cosmology and gravity dependent signal.

With 6) in mind, the remainder of this dissertation will review the prospects for principled inference of photometric and spectroscopic intensity mapping experiments.

5.1 Future Work in Line Intensity Mapping

5.1.1 Synergistic Measurement Techniques

While much of this dissertation has concerned itself with the autocorrelation and auto-power spectra of large scale structure, there is an increasing understanding that fully exploiting the information available in intensity mapping experiments will be done through cross-correlation, both

with multi-wavelength intensity mapping experiments, and with galaxy surveys in the optical and infrared. A non-exhaustive list of promising targets for cross-correlation,

1. *Ground Based Photometric and Spectroscopic Surveys* Over the next decade, a large number of ground based photometric and spectroscopic surveys are anticipated to see first light. The largest such survey, the Vera C. Rubin Observatory Legacy Survey of Space and Time (LSST), will produce an 18,000 square degree survey in six photometric filters from $\approx$ 320-1050 nm [153]. LSST is designed to produce cosmological parameter constraints through a combination of techniques, including weak lensing/cosmic shear, Baryon Acoustic Oscillations, constraints on the mass function of halos through weak lensing, and through supernova cosmology. As a photometric survey, LSST is able to achieve both a large and deep survey design (up to 24.5 magnitude) at the cost of spectroscopic information, and will require sophisticated techniques to estimate the photometric redshift probability distribution of sources for the cosmology analysis. By contrast, the Dark Energy Spectroscopic Instrument (DESI), will conduct a spectroscopic survey over $\approx$ 40% of the sky for large scale structure and redshift space distortion cosmology [195]. To achieve high survey areas in a spectroscopic survey, the limiting magnitude and depth of survey is limited to 19.5. As explored in **Chapter 3** for CASTOR, cross-correlations between large photometric and ground based surveys will provide improved redshift estimates for photometric experiments. More speculatively, similar cross correlations may also be able to address the interloper line problem for spectroscopic intensity mapping or contribute to removal of catastrophic outliers in photometric redshift surveys.

2. *Space Based Surveys - Roman and Euclid Observatories* The Nancy Grace Roman and Euclid Space Telescope will produce large and complementary surveys of much of the sky. Similar to the situation with ground based instruments that trade survey area for survey depth, the Roman telescope will survey 5% of the sky to a limiting magnitude of $\approx$ 27 [97], while Euclid will survey up to 50% of the sky to a much lower magnitude $\approx$ 24 in most bands [98]. Roman

and Euclid will depend on lensing studies to calibrate the bias in order to reliably estimate the matter density from clustering. Lensing of sub-mm intensity maps has only recently been explored (cf [196]), but 21 cm lensing has been more extensively studied (cf [197]). Cross correlations between Roman and Euclid with lensed intensity maps may aid the bias calibration of both LIM experiments as well as the space based galaxy surveys. Finally, cluster cosmology depends on accurate mass calibration from phase space modeling. Traditionally this has been achieved with high resolution spectroscopy of cluster galaxies, but future modeling of the LIM signal may allow a reliable inference from the measured intensity to the halo mass.

3. *Multi-wavelength LIM Cross-Correlations* Internal cross correlations between multiple lines observed simultaneously and external cross correlations between lines observed by multiple instruments are expected to be a major source of information about cosmology and astrophysics, as well as a key technique for mitigating systematics. Applications for extracting the target line power spectra in the presence of interloper emission are reviewed in Chapter 1.3. Targets include CO J $\rightarrow$ J-1 transitions, as well as rotational or CII Lyα with HETDEX at low redshift or SPHEREx at high redshift [35].

4. *Cosmic Microwave Background Experiments* Cosmic Microwave Background experiments have historically provided stringent constraints on the Cosmic Infrared Background (see Chapter 1). This opens the door for consistency checks on the CIB between *Planck* and *SPHEREx* CIB constraints. Lensing of the CMB is highly synergistic with sub-mm and 21 cm lensing, providing an obvious avenue for cross-correlation and calibration of, for example, estimates of the bias for galaxy surveys [7].

Cross-correlations between galaxy surveys and photometric or spectroscopic intensity mapping will likely be important for the first low SNR detections of the LIM clustering signal, and for extraction of information from photometric intensity maps. Synergies between next generation LIM experiments and future galaxy surveys will extend these to high SNR measurements capable of

constraining underlying astrophysics and cosmology.

5.1.2 Line Emission Models

Significant uncertainties in the estimates of line intensities and luminosity functions for sub-mm emission lines remain. In particular, predicting the line intensity power spectra and noise properties require knowledge of how line luminosities scale with halo and galaxy properties. There are two common approaches to solving this problem,

1. Semi-analytic modeling frameworks begin by generating dark matter halos with merger histories estimated from extended-Press Schechter models [198]. After producing merger histories for the halo population, empirical and simulation derived scaling relations are used to assign gas fractions and metallicities to the halo masses. Cooling rate estimates are then used to turn gas fractions and metallicities into estimates of the line emission. The key advantage of the SAM approach is that it is more interpretable than simulation derived estimates of line emission, while comparison of the SAMs are broadly consistent with observations over a large range in redshift. Despite this, applying existing SAMs to analysis of intensity maps requires uncertain extrapolation to higher redshifts where it is difficult to independently calibrate the SAMs.

2. Simulation post-processing frameworks are an alternative that attempts to self-consistently model multi-line emission properties. The Simulator of Galaxy Millimeter/Submillimeter Emission (SIGAME) is a tool for sub-grid modeling of smoothed particle hydrodynamic (SPH) simulations to self-consistently predict multi-line emission properties [199]. Outputs from SPH simulations are first read in to assign gas fractions, masses, and metallicities. SIGAME then uses gas fraction estimates to assign gas to giant molecular clouds and diffuse components, consistently tracking the metallicity of the gas. Radiative transfer models are then generated to track the line luminosities as a function of gas properties. Final outputs include gas

properties and spatially resolved line luminosities. SIGAME is a fully consistent and physically motivated tool, not relying on explicit scaling relations or uncertain extrapolations. This trades generalizability for interpretability, extending the domain over which models can be applied while potentially obscuring the underlying physics.

Approaches to line emission modeling based on both SAMs and post-processing tools will be useful for the analysis of future intensity mapping experiments. The computational simplicity of the SAM approach makes it appropriate for integration into Monte Carlo sampling to produce estimates of line evolution parameters. Despite this, the need to independently calibrate SAMs at redshifts that are inaccessible to auxiliary surveys introduces hard to quantify uncertainties into inference based solely on SAMs. While simulation based techniques are computationally expensive, such techniques can be used to provide an independent consistency check on the predictions of SAMs. Simulation based techniques can also be used to widely sample parameter space and estimate line emission statistics and luminosity functions without simplifying assumptions about structure formation.

5.2 Summary and Concluding Remarks

Spectroscopic and photometric intensity mapping experiments will provide complementary information, especially about higher redshifts, to the catalogs produced by large ground and space based survey in the next decade. With this in mind, this dissertation has studied the ability of future photometric and spectroscopic intensity mapping experiments to improve our knowledge of astrophysics and cosmology. Beyond the major improvements in our understanding of the UV-Optical extragalactic background light and new tests of Einstein Gravity that we forecast, a primary theme of this dissertation is that large scale structure remains important as both of immediate scientific interest and as a tool for enabling complementary measurements.

Appendix A

Noise Power for Single Dish Line Intensity Mapping Experiments

Noise power can be expressed in terms of the Noise Equivalent Temperature (NET) or the Noise Equivalent Flux Density (NEFD). For consistency with our parameterization of the line luminosities in terms of line temperature (μK), we choose to work in NET. We begin by assuming a dual polarization instrument and calculate the noise equivalent power (NEP) from the incident photon load Q for each detector:

$$\mathrm{NEP}_{\mathrm{ph}} = 2h\nu Q + \frac{1}{N_{\mathrm{modes}}}\frac{2Q^2}{\Delta\nu}, \tag{A.1}$$

where ν is the detector center frequency and $\Delta\nu$ is the bandwidth. Q is the sum of power arriving at the detector from the atmosphere and emission from the telescope:

$$Q_{\mathrm{tot}} = Q_{\mathrm{atm}} + Q_{\mathrm{tel}}. \tag{A.2}$$

A detector observing a load of temperature T with optical efficiency η sees photon power $Q \approx 2\eta kT\Delta\nu$ (for $h\nu \ll kT$). We use the *am* atmospheric modeling software to calculate the typical atmospheric temperature at each frequency for the South Pole winter [200]. The telescope emission

is assumed to be at the ambient South Pole temperature $\sim$ 250 K with an emission $\epsilon = 0.01$, as measured for the South Pole Telescope. Finally, we assume that each detector has an NEP of $\sim 10^{-18}$ W/$\sqrt{\text{Hz}}$, which is added in quadrature to the incident photon NEP.

After converting the NEP to a white noise level $\sigma_{\rm rms}(\approx 481\ \mu\text{K}\cdot\sqrt{s})$, the noise power spectrum for a given integration time per pixel $t_{\rm pix}$ is

$$P_{\rm N} = V_{\rm vox}\frac{\sigma_{\rm rms}^2}{t_{\rm pix}}, \tag{A.3}$$

where the voxel volume is

$$V_{\rm vox} = r(z)^2\frac{\lambda(1+z)^2}{H(z)}\Omega_{\rm pix}\Delta\nu. \tag{A.4}$$

Here $r(z)$ is the comoving radial distance, λ is the wavelength, $H(z)$ is the Hubble parameter, and $\Omega_{\rm pix}$ is the pixel size.

Bibliography

[1] Yi-Kuan Chiang, Brice Ménard, and David Schiminovich. Broadband intensity tomography: Spectral tagging of the cosmic uv background. *The Astrophysical Journal*, 877(2):150, Jun 2019.

[2] Simon P. Driver, Stephen K. Andrews, Luke J. Davies, Aaron S. G. Robotham, Angus H. Wright, Rogier A. Windhorst, Seth Cohen, Kim Emig, Rolf A. Jansen, and Loretta Dunne. Measurements of Extragalactic Background Light from the Far UV to the Far IR from Deep Ground- and Space-based Galaxy Counts. , 827(2):108, August 2016.

[3] K. Mattila, K. Lehtinen, P. Väisänen, G. von Appen-Schnur, and Ch. Leinert. Extragalactic background light: a measurement at 400 nm using dark cloud shadow*- I. Low surface brightness spectrophotometry in the area of Lynds 1642. , 470(2):2133–2151, September 2017.

[4] Erika T. Hamden, David Schiminovich, and Mark Seibert. The Diffuse Galactic Far-ultraviolet Sky. , 779(2):180, December 2013.

[5] Helge Kragh. Cosmological theories before and without einstein. In Helge Kragh and Malcom S Longair, editors, *Oxford Handbook of the History of Modern Cosmology*. Oxford University Press (OUP), 2019.

[6] Ely D. Kovetz, Marco P. Viero, Adam Lidz, Laura Newburgh, Mubdi Rahman, Eric Switzer, Marc Kamionkowski, James Aguirre, Marcelo Alvarez, James Bock, J. Richard Bond, Goeffry Bower, C. Matt Bradford, Patrick C. Breysse, Philip Bull, Tzu-Ching Chang, Yun-Ting Cheng, Dongwoo Chung, Kieran Cleary, Asantha Corray, Abigail Crites, Rupert Croft, Olivier Doré, Michael Eastwood, Andrea Ferrara, José Fonseca, Daniel Jacobs, Garrett K. Keating, Guilaine Lagache, Gunjan Lakhlani, Adrian Liu, Kavilan Moodley, Norm Murray, Aurélie Pénin, Gergö Popping, Anthony Pullen, Dominik Reichers, Shun Saito, Ben Saliwanchik, Mario Santos, Rachel Somerville, Gordon Stacey, George Stein, Francesco Villaescusa-Navarro, Eli Visbal, Amanda Weltman, Laura Wolz, and Micheal Zemcov. Line-Intensity Mapping: 2017 Status Report. *arXiv e-prints*, page arXiv:1709.09066, September 2017.

[7] Emmanuel Schaan and Martin White. Astrophysics &amp cosmology from line intensity mapping vs galaxy surveys. *Journal of Cosmology and Astroparticle Physics*, 2021(05):067, may 2021.

[8] Azadeh Moradinezhad Dizgah, Garrett K. Keating, and Anastasia Fialkov. Probing cosmic origins with co and [c ii] emission lines. *The Astrophysical Journal*, 870(1):L4, Jan 2019.

[9] Azadeh Moradinezhad Dizgah, Garrett K. Keating, Kirit S. Karkare, Abigail Crites, and Shouvik Roy Choudhury. Neutrino properties with ground-based millimeter-wavelength line intensity mapping, 2021.

[10] Hamsa Padmanabhan, Patrick Breysse, Adam Lidz, and Eric R. Switzer. Intensity mapping from the sky: synergizing the joint potential of [oiii] and [cii] surveys at reionization, 2021.

[11] Cosmic Visions 21 cm Collaboration, Réza Ansari, Evan J. Arena, Kevin Bandura, Philip Bull, Emanuele Castorina, Tzu-Ching Chang, Shi-Fan Chen, Liam Connor, Simon Foreman, Josef Frisch, Daniel Green, Matthew C. Johnson, Dionysios Karagiannis, Adrian Liu, Kiyoshi W. Masui, P. Daniel Meerburg, Moritz Münchmeyer, Laura B. Newburgh, Andrej Obuljen, Paul O'Connor, Hamsa Padmanabhan, J. Richard Shaw, Christopher Sheehy, Anže Slosar, Kendrick Smith, Paul Stankus, Albert Stebbins, Peter Timbie, Francisco Villaescusa-Navarro, Benjamin Wallisch, and Martin White. Inflation and early dark energy with a stage ii hydrogen intensity mapping experiment, 2019.

[12] P. J. E. Peebles. Introduction to the Extragalactic Background Meeting, held at Baltimore, 1993 May 18 - 20. In *Extragalactic Background Radiation Meeting*, pages 1–13, February 1995.

[13] Michael G. Hauser and Eli Dwek. The Cosmic Infrared Background: Measurements and Implications. , 39:249–307, January 2001.

[14] Marc-Antoine Miville-Deschênes and Guilaine Lagache. IRIS: A New Generation of IRAS Maps. , 157(2):302–323, April 2005.

[15] A. Pénin, G. Lagache, A. Noriega-Crespo, J. Grain, M. A. Miville-Deschênes, N. Ponthieu, P. Martin, K. Blagrave, and F. J. Lockman. An accurate measurement of the anisotropies and mean level of the cosmic infrared background at 100 μm and 160 μm. , 543:A123, July 2012.

[16] Daniel Lenz, Olivier Doré, and Guilaine Lagache. Large-scale Maps of the Cosmic Infrared Background from Planck. , 883(1):75, September 2019.

[17] Olivier Doré, Jamie Bock, Matthew Ashby, Peter Capak, Asantha Cooray, Roland de Putter, Tim Eifler, Nicolas Flagey, Yan Gong, Salman Habib, Katrin Heitmann, Chris Hirata, Woong-Seob Jeong, Raj Katti, Phil Korngut, Elisabeth Krause, Dae-Hee Lee, Daniel Masters, Phil Mauskopf, Gary Melnick, Bertrand Mennesson, Hien Nguyen, Karin Öberg, Anthony Pullen, Alvise Raccanelli, Roger Smith, Yong-Seon Song, Volker Tolls, Steve Unwin, Tejaswi Venumadhav, Marco Viero, Mike Werner, and Mike Zemcov. Cosmology with the SPHEREX All-Sky Spectral Survey. *arXiv e-prints*, page arXiv:1412.4872, December 2014.

[18] Yun-Ting Cheng and Tzu-Ching Chang. Cosmic Near-infrared Background Tomography with SPHEREx Using Galaxy Cross-correlations. , 925(2):136, February 2022.

[19] P. J. E. Peebles. *The large-scale structure of the universe*. 1980.

[20] A. Gabrielli, F.S. Labini, M. Joyce, and L. Pietronero. *Statistical Physics for Cosmic Structures*. Springer Berlin Heidelberg, 2006.

[21] V. J. Martínez and E. Saar. *Statistics of the Galaxy Distribution*. 2002.

[22] Yun-Ting Cheng, Tzu-Ching Chang, and James J. Bock. Phase-space spectral line deconfusion in intensity mapping. *The Astrophysical Journal*, 901(2):142, Oct 2020.

[23] Jonathan R Pritchard and Abraham Loeb. 21 cm cosmology in the 21st century. *Reports on Progress in Physics*, 75(8):086901, jul 2012.

[24] Alberto D. Bolatto, Mark Wolfire, and Adam K. Leroy. The CO-to-H_2 Conversion Factor. , 51(1):207–268, August 2013.

[25] Patrick C. Breysse, Ely D. Kovetz, and Marc Kamionkowski. The high-redshift star formation history from carbon-monoxide intensity maps. , 457(1):L127–L131, March 2016.

[26] Patrick C. Breysse, Dongwoo T. Chung, Kieran A. Cleary, Håvard T. Ihle, Hamsa Padmanabhan, Marta B. Silva, J. Richard Bond, Jowita Borowska, Morgan Catha, Sarah E. Church, Delaney A. Dunne, Hans Kristian Eriksen, Marie Kristine Foss, Todd Gaier, Joshua Ott Gundersen, Andrew I. Harris, Richard Hobbs, Laura Keating, James W. Lamb, Charles R. Lawrence, Jonas G. S. Lunde, Norman Murray, Timothy J. Pearson, Liju Philip, Maren Rasmussen, Anthony C. S. Readhead, Thomas J. Rennie, Nils-Ole Stutzer, Marco P. Viero, Duncan J. Watts, Ingunn Katherine Wehus, and David P. Woody. COMAP Early Science: VII. Prospects for CO Intensity Mapping at Reionization. *arXiv e-prints*, page arXiv:2111.05933, November 2021.

[27] Håvard T. Ihle, Jowita Borowska, Kieran A. Cleary, Hans Kristian Eriksen, Marie K. Foss, Stuart E. Harper, Junhan Kim, Jonas G. S. Lunde, Liju Philip, Maren Rasmussen, Nils-Ole Stutzer, Bade D. Uzgil, Duncan J. Watts, Ingunn Kathrine Wehus, J. Richard Bond, Patrick C. Breysse, Morgan Catha, Sarah E. Church, Dongwoo T. Chung, Clive Dickinson, Delaney A. Dunne, Todd Gaier, Joshua Ott Gundersen, Andrew I. Harris, Richard Hobbs, James W. Lamb, Charles R. Lawrence, Norman Murray, Anthony C. S. Readhead, Hamsa Padmanabhan, Timothy J. Pearson, Thomas J. Rennie, and David P. Woody. COMAP Early Science: IV. Power Spectrum Methodology and Results. *arXiv e-prints*, page arXiv:2111.05930, November 2021.

[28] Kieran A. Cleary, Jowita Borowska, Patrick C. Breysse, Morgan Catha, Dongwoo T. Chung, Sarah E. Church, Clive Dickinson, Hans Kristian Eriksen, Marie Kristine Foss, Joshua Ott Gundersen, Stuart E. Harper, Andrew I. Harris, Richard Hobbs, Håvard, T. Ihle, Junhan Kim, Jonathon Kocz, James W. Lamb, Jonas G. S. Lunde, Hamsa Padmanabhan, Timothy J. Pearson, Liju Philip, Travis W. Powell, Maren Rasmussen, Anthony C. S. Readhead, Thomas J. Rennie, Marta B. Silva, Nils-Ole Stutzer, Bade D. Uzgil, Duncan J. Watts, Ingunn Kathrine Wehus, David P. Woody, Lilian Basoalto, J. Richard Bond, Delaney A. Dunne, Todd Gaier, Brandon Hensley, Laura C. Keating, Charles R. Lawrence, Norman Murray, Rodrigo Reeves, Marco P.

Viero, and Risa Wechsler. COMAP Early Science: I. Overview. *arXiv e-prints*, page arXiv:2111.05927, November 2021.

[29] Dongwoo T. Chung, Patrick C. Breysse, Kieran A. Cleary, Håvard T. Ihle, Hamsa Padmanabhan, Marta B. Silva, J. Richard Bond, Jowita Borowska, Morgan Catha, Sarah E. Church, Delaney A. Dunne, Hans Kristian Eriksen, Marie Kristine Foss, Todd Gaier, Joshua Ott Gundersen, Stuart E. Harper, Andrew I. Harris, Brandon Hensley, Richard Hobbs, Laura C. Keating, Junhan Kim, James W. Lamb, Charles R. Lawrence, Jonas Gahr Sturtzel Lunde, Norman Murray, Timothy J. Pearson, Liju Philip, Maren Rasmussen, Anthony C. S. Readhead, Thomas J. Rennie, Nils-Ole Stutzer, Bade D. Uzgil, Marco P. Viero, Duncan J. Watts, Risa H. Wechsler, Ingunn Kathrine Wehus, and David P. Woody. COMAP Early Science: V. Constraints and Forecasts at $z \sim 3$. *arXiv e-prints*, page arXiv:2111.05931, November 2021.

[30] G. Sun, T.-C. Chang, B. D. Uzgil, J. J. Bock, C. M. Bradford, V. Butler, T. Caze-Cortes, Y.-T. Cheng, A. Cooray, A. T. Crites, S. Hailey-Dunsheath, N. Emerson, C. Frez, B. L. Hoscheit, J. Hunacek, R. P. Keenan, C. T. Li, P. Madonia, D. P. Marrone, L. Moncelsi, C. Shiu, I. Trumper, A. Turner, A. Weber, T. S. Wei, and M. Zemcov. Probing cosmic reionization and molecular gas growth with TIME. *The Astrophysical Journal*, 915(1):33, jul 2021.

[31] M. Bethermin, A. Gkogkou, M. Van Cuyck, G. Lagache, A. Beelen, M. Aravena, A. Benoit, J. Bounmy, M. Calvo, A. Catalano, B. de Batz de Trenquelleon, C. De Breuck, A. Fasano, A. Ferrara, J. Goupy, C. Hoarau, C. Horellou, W. Hu, A. Julia, K. Knudsen, J. C. Lambert, J. Macias-Perez, J. Marpaud, A. Monfardini, A. Pallottini, N. Ponthieu, Y. Roehlly, L. Vallini, F. Walter, and A. Weiss. CONCERTO: High-fidelity simulation of millimeter line emissions of galaxies and [CII] intensity mapping. *arXiv e-prints*, page arXiv:2204.12827, April 2022.

[32] Patrick C. Breysse, Ely D. Kovetz, and Marc Kamionkowski. Carbon monoxide intensity mapping at moderate redshifts. *Monthly Notices of the Royal Astronomical Society*, 443(4):3506–3512, Aug 2014.

[33] Patrick C. Breysse, Christopher J. Anderson, and Philippe Berger. Canceling Out Intensity Mapping Foregrounds. , 123(23):231105, December 2019.

[34] H. T. Ihle, D. Chung, G. Stein, M. Alvarez, J. R. Bond, P. C. Breysse, K. A. Cleary, H. K. Eriksen, M. K. Foss, J. O. Gundersen, S. Harper, N. Murray, H. Padmanabhan, M. P. Viero, I. K. Wehus, and COMAP Collaboration. Joint Power Spectrum and Voxel Intensity Distribution Forecast on the CO Luminosity Function with COMAP. , 871(1):75, January 2019.

[35] Marta B. Silva, Bernhard Baumschlager, Kieran A. Cleary, Patrick C. Breysse, Dongwoo T. Chung, Håvard T. Ihle, Hamsa Padmanabhan, Laura C. Keating, Junhan Kim, and Liju Philip. Synergies between the COMAP CO Line Intensity Mapping mission and a Ly{} galaxy survey: How to probe the early universe with voxel based analysis of observational data. *arXiv e-prints*, page arXiv:2111.05354, November 2021.

[36] José Luis Bernal, Andrea Caputo, Francisco Villaescusa-Navarro, and Marc Kamionkowski. Searching for the Radiative Decay of the Cosmic Neutrino Background with Line-Intensity Mapping. , 127(13):131102, September 2021.

[37] Matthew McQuinn, Oliver Zahn, Matias Zaldarriaga, Lars Hernquist, and Steven R. Furlanetto. Cosmological parameter estimation using 21 cm radiation from the epoch of reionization. *The Astrophysical Journal*, 653(2):815–834, Dec 2006.

[38] Adam Lidz and Jessie Taylor. On removing interloper contamination from intensity mapping power spectrum measurements. *The Astrophysical Journal*, 825(2):143, Jul 2016.

[39] Yan Gong, Xuelei Chen, and Asantha Cooray. Cosmological constraints from line intensity mapping with interlopers. *The Astrophysical Journal*, 894(2):152, May 2020.

[40] G. Sun, L. Moncelsi, M. P. Viero, M. B. Silva, J. Bock, C. M. Bradford, T.-C. Chang, Y.-T. Cheng, A. R. Cooray, A. Crites, S. Hailey-Dunsheath, B. Uzgil, J. R. Hunacek, and M. Zemcov. A foreground masking strategy for [c ii] intensity mapping experiments using galaxies selected by stellar mass and redshift. *The Astrophysical Journal*, 856(2):107, mar 2018.

[41] Emmanuel Schaan and Martin White. Multi-tracer intensity mapping: cross-correlations, line noise & decorrelation. , 2021(5):068, May 2021.

[42] Ryley Hill, Kiyoshi W. Masui, and Douglas Scott. The Spectrum of the Universe. *Applied Spectroscopy*, 72(5):663–688, May 2018.

[43] Kalevi Mattila and Petri Väisänen. Extragalactic background light: inventory of light throughout the cosmic history. *Contemporary Physics*, 60(1):23–44, January 2019.

[44] M. Ackermann, M. Ajello, A. Albert, W. B. Atwood, L. Baldini, J. Ballet, G. Barbiellini, D. Bastieri, K. Bechtol, R. Bellazzini, E. Bissaldi, R. D. Blandford, E. D. Bloom, E. Bottacini, T. J. Brandt, J. Bregeon, P. Bruel, R. Buehler, S. Buson, G. A. Caliandro, R. A. Cameron, M. Caragiulo, P. A. Caraveo, E. Cavazzuti, C. Cecchi, E. Charles, A. Chekhtman, J. Chiang, G. Chiaro, S. Ciprini, R. Claus, J. Cohen-Tanugi, J. Conrad, A. Cuoco, S. Cutini, F. D'Ammando, A. de Angelis, F. de Palma, C. D. Dermer, S. W. Digel, E. do Couto e. Silva, P. S. Drell, C. Favuzzi, E. C. Ferrara, W. B. Focke, A. Franckowiak, Y. Fukazawa, S. Funk, P. Fusco, F. Gargano, D. Gasparrini, S. Germani, N. Giglietto, P. Giommi, F. Giordano, M. Giroletti, G. Godfrey, G. A. Gomez-Vargas, I. A. Grenier, S. Guiriec, M. Gustafsson, D. Hadasch, K. Hayashi, E. Hays, J. W. Hewitt, P. Ippoliti, T. Jogler, G. Jóhannesson, A. S. Johnson, W. N. Johnson, T. Kamae, J. Kataoka, J. Knödlseder, M. Kuss, S. Larsson, L. Latronico, J. Li, L. Li, F. Longo, F. Loparco, B. Lott, M. N. Lovellette, P. Lubrano, G. M. Madejski, A. Manfreda, F. Massaro, M. Mayer, M. N. Mazziotta, J. E. McEnery, P. F. Michelson, W. Mitthumsiri, T. Mizuno, A. A. Moiseev, M. E. Monzani, A. Morselli, I. V. Moskalenko, S. Murgia, R. Nemmen, E. Nuss, T. Ohsugi, N. Omodei, E. Orlando, J. F. Ormes, D. Paneque, J. H. Panetta, J. S. Perkins, M. Pesce-Rollins, F. Piron, G. Pivato, T. A. Porter, S. Rainò, R. Rando, M. Razzano, S. Razzaque, A. Reimer, O. Reimer, T. Reposeur, S. Ritz, R. W. Romani, M. Sánchez-Conde,

M. Schaal, A. Schulz, C. Sgrò, E. J. Siskind, G. Spandre, P. Spinelli, A. W. Strong, D. J. Suson, H. Takahashi, J. G. Thayer, J. B. Thayer, L. Tibaldo, M. Tinivella, D. F. Torres, G. Tosti, E. Troja, Y. Uchiyama, G. Vianello, M. Werner, B. L. Winer, K. S. Wood, M. Wood, G. Zaharijas, and S. Zimmer. The Spectrum of Isotropic Diffuse Gamma-Ray Emission between 100 MeV and 820 GeV. , 799(1):86, January 2015.

[45] Jesús Zavala, Volker Springel, and Michael Boylan-Kolchin. Extragalactic gamma-ray background radiation from dark matter annihilation. *Monthly Notices of the Royal Astronomical Society*, 405(1):593–612, 06 2010.

[46] A. A. Penzias and R. W. Wilson. A Measurement of Excess Antenna Temperature at 4080 Mc/s. , 142:419–421, July 1965.

[47] Scott Dodelson. *Modern Cosmology*. 2003.

[48] P. J. E. Peebles. *Principles of Physical Cosmology*. 1993.

[49] Matthew McQuinn. The Evolution of the Intergalactic Medium. , 54:313–362, September 2016.

[50] Francesco Haardt and Piero Madau. Radiative Transfer in a Clumpy Universe. IV. New Synthesis Models of the Cosmic UV/X-Ray Background. , 746(2):125, February 2012.

[51] Ewald Puchwein, Francesco Haardt, Martin G Haehnelt, and Piero Madau. Consistent modelling of the meta-galactic uv background and the thermal/ionization history of the intergalactic medium. *Monthly Notices of the Royal Astronomical Society*, 485(1):47?68, Jan 2019.

[52] Claude-André Faucher-Giguère. A cosmic uv/x-ray background model update. *Monthly Notices of the Royal Astronomical Society*, 493(2):1614?1632, Jan 2020.

[53] M. S. Akshaya, Jayant Murthy, S. Ravichandran, R. C. Henry, and James Overduin. The Diffuse Radiation Field at High Galactic Latitudes. , 858(2):101, May 2018.

[54] Tod R. Lauer, Marc Postman, Harold A. Weaver, John R. Spencer, S. Alan Stern, Marc W. Buie, Daniel D. Durda, Carey M. Lisse, A. R. Poppe, Richard P. Binzel, Daniel T. Britt, Bonnie J. Buratti, Andrew F. Cheng, W. M. Grundy, Mihaly Horanyi J. J. Kavelaars, Ivan R. Linscott, William B. McKinnon, Jeffrey M. Moore, J. I. Nuñez Catherine B. Olkin, Joel W. Parker, Simon B. Porter, Dennis C. Reuter, Stuart J. Robbins, Paul Schenk, Mark R. Showalter, Kelsi N. Singer, Anne. J. Verbiscer, and Leslie A. Youn. New horizons observations of the cosmic optical background, 2020.

[55] Rudy C. Gilmore, Piero Madau, Joel R. Primack, Rachel S. Somerville, and Francesco Haardt. GeV gamma-ray attenuation and the high-redshift UV background. , 399(4):1694–1708, November 2009.

[56] Jeffrey A. Newman. Calibrating redshift distributions beyond spectroscopic limits with cross-correlations. *The Astrophysical Journal*, 684(1):88–101, Sep 2008.

[57] Brice Ménard, Ryan Scranton, Samuel Schmidt, Chris Morrison, Donghui Jeong, Tamas Budavari, and Mubdi Rahman. Clustering-based redshift estimation: method and application to data, 2013.

[58] Tim Maudlin and Scott Soames. *Space and Time*. Princeton University Press, 2012.

[59] Robert M. Wald. *General relativity*. 1984.

[60] John D. Norton. General covariance and the foundations of general relativity: Eight decades of dispute. *Reports on Progress in Physics*, 56(791–861), 1993.

[61] John D. Norton. Einstein?s conflicting heuristics: The discovery of general relativity, March 2018.

[62] Planck Collaboration, N. Aghanim, Y. Akrami, M. Ashdown, J. Aumont, C. Baccigalupi, M. Ballardini, A. J. Banday, R. B. Barreiro, N. Bartolo, S. Basak, R. Battye, K. Benabed, J. P. Bernard, M. Bersanelli, P. Bielewicz, J. J. Bock, J. R. Bond, J. Borrill, F. R. Bouchet, F. Boulanger, M. Bucher, C. Burigana, R. C. Butler, E. Calabrese, J. F. Cardoso, J. Carron, A. Challinor, H. C. Chiang, J. Chluba, L. P. L. Colombo, C. Combet, D. Contreras, B. P. Crill, F. Cuttaia, P. de Bernardis, G. de Zotti, J. Delabrouille, J. M. Delouis, E. Di Valentino, J. M. Diego, O. Doré, M. Douspis, A. Ducout, X. Dupac, S. Dusini, G. Efstathiou, F. Elsner, T. A. Enßlin, H. K. Eriksen, Y. Fantaye, M. Farhang, J. Fergusson, R. Fernandez-Cobos, F. Finelli, F. Forastieri, M. Frailis, A. A. Fraisse, E. Franceschi, A. Frolov, S. Galeotta, S. Galli, K. Ganga, R. T. Génova-Santos, M. Gerbino, T. Ghosh, J. González-Nuevo, K. M. Górski, S. Gratton, A. Gruppuso, J. E. Gudmundsson, J. Hamann, W. Handley, F. K. Hansen, D. Herranz, S. R. Hildebrandt, E. Hivon, Z. Huang, A. H. Jaffe, W. C. Jones, A. Karakci, E. Keihänen, R. Keskitalo, K. Kiiveri, J. Kim, T. S. Kisner, L. Knox, N. Krachmalnicoff, M. Kunz, H. Kurki-Suonio, G. Lagache, J. M. Lamarre, A. Lasenby, M. Lattanzi, C. R. Lawrence, M. Le Jeune, P. Lemos, J. Lesgourgues, F. Levrier, A. Lewis, M. Liguori, P. B. Lilje, M. Lilley, V. Lindholm, M. López-Caniego, P. M. Lubin, Y. Z. Ma, J. F. Macías-Pérez, G. Maggio, D. Maino, N. Mandolesi, A. Mangilli, A. Marcos-Caballero, M. Maris, P. G. Martin, M. Martinelli, E. Martínez-González, S. Matarrese, N. Mauri, J. D. McEwen, P. R. Meinhold, A. Melchiorri, A. Mennella, M. Migliaccio, M. Millea, S. Mitra, M. A. Miville-Deschênes, D. Molinari, L. Montier, G. Morgante, A. Moss, P. Natoli, H. U. Nørgaard-Nielsen, L. Pagano, D. Paoletti, B. Partridge, G. Patanchon, H. V. Peiris, F. Perrotta, V. Pettorino, F. Piacentini, L. Polastri, G. Polenta, J. L. Puget, J. P. Rachen, M. Reinecke, M. Remazeilles, A. Renzi, G. Rocha, C. Rosset, G. Roudier, J. A. Rubiño-Martín, B. Ruiz-Granados, L. Salvati, M. Sandri, M. Savelainen, D. Scott, E. P. S. Shellard, C. Sirignano, G. Sirri, L. D. Spencer, R. Sunyaev, A. S. Suur-Uski, J. A. Tauber, D. Tavagnacco, M. Tenti, L. Toffolatti, M. Tomasi, T. Trombetti, L. Valenziano, J. Valiviita, B. Van Tent, L. Vibert, P. Vielva, F. Villa, N. Vittorio, B. D. Wand elt, I. K. Wehus, M. White, S. D. M. White, A. Zacchei, and A. Zonca. Planck 2018 results. VI. Cosmological parameters. *arXiv e-prints*, page arXiv:1807.06209, July 2018.

[63] Chris Smeenk. Einstein's role in the creation of relativistic cosmology. In Michel Janssen and Christoph Lehner, editors, *The Cambridge Companion to Einstein*, pages 228–269. Cambridge: Cambridge University Press, 2014.

[64] A. Zee. *Einstein Gravity in a Nutshell*. Princeton University Press, New Jersey, 5 2013.

[65] Sean M. Carroll. *Spacetime and geometry. An introduction to general relativity*. 2004.

[66] Daniel Baumann. TASI Lectures on Inflation. *arXiv e-prints*, page arXiv:0907.5424, July 2009.

[67] David Wallace. Quantum Gravity at Low Energies. *arXiv e-prints*, page arXiv:2112.12235, December 2021.

[68] Robert H. Brandenberger. Lectures on the Theory of Cosmological Perturbations. In Nora Bretón, Jorge Luis Cervantes-Cota, and Marcelo Salgad, editors, *The Early Universe and Observational Cosmology*, volume 646, pages 127–167. 2004.

[69] Hannu Kurki-Suonio. Cosmological perturbation theory. *unpublished lecture notes available: https://www.mv.helsinki.fi/home/hkurkisu/CosPer.pdf*, 2022.

[70] Luca Amendola, Simone Fogli, Alejandro Guarnizo, Martin Kunz, and Adrian Vollmer. Model-independent constraints on the cosmological anisotropic stress. , 89(6):063538, March 2014.

[71] Marilena LoVerde and Niayesh Afshordi. Extended Limber approximation. , 78(12):123506, December 2008.

[72] A. J. S. Hamilton. Linear Redshift Distortions: a Review. In Donald Hamilton, editor, *The Evolving Universe*, volume 231 of *Astrophysics and Space Science Library*, page 185, January 1998.

[73] David Lovelock. The Einstein Tensor and Its Generalizations. *Journal of Mathematical Physics*, 12(3):498–501, March 1971.

[74] Erik Curiel. A simple proof of the uniqueness of the einstein field equation in all dimensions, 2016.

[75] Timothy Clifton, Pedro G. Ferreira, Antonio Padilla, and Constantinos Skordis. Modified gravity and cosmology. *Physics Reports*, 513(1-3):1–189, Mar 2012.

[76] Adam G. Riess, Alexei V. Filippenko, Peter Challis, Alejandro Clocchiatti, Alan Diercks, Peter M. Garnavich, Ron L. Gilliland, Craig J. Hogan, Saurabh Jha, Robert P. Kirshner, B. Leibundgut, M. M. Phillips, David Reiss, Brian P. Schmidt, Robert A. Schommer, R. Chris Smith, J. Spyromilio, Christopher Stubbs, Nicholas B. Suntzeff, and John Tonry. Observational Evidence from Supernovae for an Accelerating Universe and a Cosmological Constant. , 116(3):1009–1038, September 1998.

[77] Brian P. Schmidt, Nicholas B. Suntzeff, M. M. Phillips, Robert A. Schommer, Alejandro Clocchiatti, Robert P. Kirshner, Peter Garnavich, Peter Challis, B. Leibundgut, J. Spyromilio, Adam G. Riess, Alexei V. Filippenko, Mario Hamuy, R. Chris Smith, Craig Hogan, Christopher Stubbs, Alan Diercks, David Reiss, Ron Gilliland, John Tonry, José Maza, A. Dressler, J. Walsh, and R. Ciardullo. The High-Z Supernova Search: Measuring Cosmic Deceleration and Global Curvature of the Universe Using Type IA Supernovae. , 507(1):46–63, November 1998.

[78] Shinji Tsujikawa. Scalar tensor theories and modified matter models. In *TPCosmo V School on Cosmology*. Portsmouth Institute of Cosmology and Gravitation, 2019.

[79] Gregory Walter Horndeski. Second-Order Scalar-Tensor Field Equations in a Four-Dimensional Space. *International Journal of Theoretical Physics*, 10(6):363–384, September 1974.

[80] Emilio Bellini and Ignacy Sawicki. Maximal freedom at minimum cost: linear large-scale structure in general modifications of gravity. *Journal of Cosmology and Astroparticle Physics*, 2014(07):050–050, Jul 2014.

[81] Licia Verde, Tommaso Treu, and Adam G. Riess. Tensions between the early and late universe. *Nature Astronomy*, 3(10):891–895, Sep 2019.

[82] Eleonora Di Valentino, Olga Mena, Supriya Pan, Luca Visinelli, Weiqiang Yang, Alessandro Melchiorri, David F. Mota, Adam G. Riess, and Joseph Silk. In the realm of the Hubble tension-a review of solutions. *Classical and Quantum Gravity*, 38(15):153001, July 2021.

[83] K. S. Karkare, A. J. Anderson, P. S. Barry, B. A. Benson, J. E. Carlstrom, T. Cecil, C. L. Chang, M. A. Dobbs, M. Hollister, G. K. Keating, D. P. Marrone, J. McMahon, J. Montgomery, Z. Pan, G. Robson, M. Rouble, E. Shirokoff, and G. Smecher. SPT-SLIM: A Line Intensity Mapping Pathfinder for the South Pole Telescope. *Journal of Low Temperature Physics*, March 2022.

[84] Edmund J. Copeland, M. Sami, and Shinji Tsujikawa. Dynamics of Dark Energy. *International Journal of Modern Physics D*, 15(11):1753–1935, January 2006.

[85] Kirit S. Karkare and Simeon Bird. Constraining the expansion history and early dark energy with line intensity mapping. *Physical Review D*, 98(4), Aug 2018.

[86] J.M. Overduin and P.S. Wesson. Dark matter and background light. *Physics Reports*, 402(5-6):267?406, Nov 2004.

[87] M. McQuinn and M. White. On using angular cross-correlations to determine source redshift distributions. *Monthly Notices of the Royal Astronomical Society*, 433(4):2857?2883, Jul 2013.

[88] Jayant Murthy, Doyle Hall, Matthew Earl, R. C. Henry, and J. B. Holberg. An Analysis of 17 Years of Voyager Observations of the Diffuse Far-Ultraviolet Radiation Field. , 522(2):904–914, September 1999.

[89] Jerry Edelstein, Stuart Bowyer, and Michael Lampton. Reanalysis ofVoyager Ultraviolet Spectrometer Limits to the Extreme-Ultraviolet and Far-Ultraviolet Diffuse Astronomical Flux. , 539(1):187–190, August 2000.

[90] Y. Matsuoka, N. Ienaka, K. Kawara, and S. Oyabu. Cosmic Optical Background: The View from Pioneer 10/11. , 736(2):119, August 2011.

[91] Michael Zemcov, Poppy Immel, Chi Nguyen, Asantha Cooray, Carey M. Lisse, and Andrew R. Poppe. Measurement of the cosmic optical background using the long range reconnaissance imager on New Horizons. *Nature Communications*, 8:15003, April 2017.

[92] K. Mattila. Observations of the Extragalactic Background Light. In Stuart Bowyer and Christoph Leinert, editors, *The Galactic and Extragalactic Background Radiation*, volume 139 of *IAU Symposium*, page 257, January 1990.

[93] Piero Madau and Lucia Pozzetti. Deep galaxy counts, extragalactic background light and the stellar baryon budget. , 312(2):L9–L15, February 2000.

[94] Jonathan P. Gardner, Thomas M. Brown, and Henry C. Ferguson. Ultraviolet Galaxy Counts from Space Telescope Imaging Spectrograph Observations of the Hubble Deep Fields. , 542(2):L79–L82, October 2000.

[95] Jayant Murthy, R. C. Henry, and N. V. Sujatha. Mapping the Diffuse Ultraviolet Sky with the Galaxy Evolution Explorer. , 724(2):1389–1395, December 2010.

[96] Patrick Cote, Bob Abraham, Michael Balogh, Peter Capak, Ray Carlberg, Nick Cowan, Oleg Djazovski, Laurent Drissen, Maria Drout, Jean Dupuis, Chris Evans, Nicholas Fantin, Laura Ferrarese, Wes Fraser, Sarah Gallagher, Terry Girard, Robert Gleisinger, Frederic Grandmont, Patrick Hall, Martin Hellmich, Tim Hardy, Paul Harrison, Renee Hlozek, Daryl Haggard, Vincent Henault-Brunet, John Hutchings, Viraja Khatu, JJ Kavelaars, Denis Laurin, Jean-Francois Lavigne, Doug Lisman, Christian Marois, David McCabe, Stanimir Metchev, Thibaud Moutard, Barth Netterfield, Shouleh Nikzad, Nathalie Ouellette, Emily Pass, Laura Parker, John Pazder, Will Percival, Jason Rhodes, Carmelle Robert, Jason Rowe, Ruben Sanchez-Janssen, Greg Sivakoff, Charles Shapiro, Marcin Sawicki, Alan Scott, Ludovic Van Waerbeke, and Kim Venn. CASTOR: A Flagship Canadian Space Telescope. In *Canadian Long Range Plan for Astronony and Astrophysics White Papers*, volume 2020, page 18, October 2019.

[97] Olivier Doré, Christopher Hirata, Yun Wang, David Weinberg, Ivano Baronchelli, Andrew Benson, Peter Capak, Ami Choi, Tim Eifler, Shoubaneh Hemmati, Shirley Ho, Albert Izard, Bhuvnesh Jain, Mike Jarvis, Alina Kiessling, Elisabeth Krause, Elena Massara, Dan Masters, Alex Merson, Hironao Miyatake, Andres Plazas Malagon, Rachel Mandelbaum, Lado Samushia, Chaz Shapiro, Melanie Simet, David Spergel, Harry Teplitz, Michael Troxel, Rachel Bean, James Colbert, Chen He Heinrich, Katrin Heitmann, George Helou, Michael Hudson, Eric Huff, Alexie Leauthaud, Niall MacCrann, Nikhil Padmanabhan, Alice Pisani, Jason Rhodes, Eduardo Rozo, Mike Seiffert, Kendrick Smith, Masahiro Takada, Anja von der Linden, Robert Lupton, Naoki Yoshida, Hao-Yi Wu, and Ying Zu. WFIRST Science Investigation Team "Cosmology with the High Latitude Survey" Annual Report 2017. *arXiv e-prints*, page arXiv:1804.03628, April 2018.

[98] R. Laureijs, J. Amiaux, S. Arduini, J. L. Augueres, J. Brinchmann, R. Cole, M. Cropper, C. Dabin, L. Duvet, A. Ealet, B. Garilli, P. Gondoin, L. Guzzo, J. Hoar, H. Hoekstra, R. Holmes, T. Kitching, T. Maciaszek, Y. Mellier, F. Pasian, W. Percival, J. Rhodes, G. Saavedra Criado, M. Sauvage, R. Scaramella, L. Valenziano, S. Warren, R. Bender, F. Castander, A. Cimatti, O. Le Fèvre, H. Kurki-Suonio, M. Levi, P. Lilje, G. Meylan, R. Nichol, K. Pedersen, V. Popa, R. Rebolo Lopez, H. W. Rix, H. Rottgering, W. Zeilinger, F. Grupp, P. Hudelot, R. Massey, M. Meneghetti,

L. Miller, S. Paltani, S. Paulin-Henriksson, S. Pires, C. Saxton, T. Schrabback, G. Seidel, J. Walsh, N. Aghanim, L. Amendola, J. Bartlett, C. Baccigalupi, J. P. Beaulieu, K. Benabed, J. G. Cuby, D. Elbaz, P. Fosalba, G. Gavazzi, A. Helmi, I. Hook, M. Irwin, J. P. Kneib, M. Kunz, F. Mannucci, L. Moscardini, C. Tao, R. Teyssier, J. Weller, G. Zamorani, M. R. Zapatero Osorio, O. Boulade, J. J. Foumond, A. Di Giorgio, P. Guttridge, A. James, M. Kemp, J. Martignac, A. Spencer, D. Walton, T. Blümchen, C. Bonoli, F. Bortoletto, C. Cerna, L. Corcione, C. Fabron, K. Jahnke, S. Ligori, F. Madrid, L. Martin, G. Morgante, T. Pamplona, E. Prieto, M. Riva, R. Toledo, M. Trifoglio, F. Zerbi, F. Abdalla, M. Douspis, C. Grenet, S. Borgani, R. Bouwens, F. Courbin, J. M. Delouis, P. Dubath, A. Fontana, M. Frailis, A. Grazian, J. Koppenhöfer, O. Mansutti, M. Melchior, M. Mignoli, J. Mohr, C. Neissner, K. Noddle, M. Poncet, M. Scodeggio, S. Serrano, N. Shane, J. L. Starck, C. Surace, A. Taylor, G. Verdoes-Kleijn, C. Vuerli, O. R. Williams, A. Zacchei, B. Altieri, I. Escudero Sanz, R. Kohley, T. Oosterbroek, P. Astier, D. Bacon, S. Bardelli, C. Baugh, F. Bellagamba, C. Benoist, D. Bianchi, A. Biviano, E. Branchini, C. Carbone, V. Cardone, D. Clements, S. Colombi, C. Conselice, G. Cresci, N. Deacon, J. Dunlop, C. Fedeli, F. Fontanot, P. Franzetti, C. Giocoli, J. Garcia-Bellido, J. Gow, A. Heavens, P. Hewett, C. Heymans, A. Holland, Z. Huang, O. Ilbert, B. Joachimi, E. Jennins, E. Kerins, A. Kiessling, D. Kirk, R. Kotak, O. Krause, O. Lahav, F. van Leeuwen, J. Lesgourgues, M. Lombardi, M. Magliocchetti, K. Maguire, E. Majerotto, R. Maoli, F. Marulli, S. Maurogordato, H. McCracken, R. McLure, A. Melchiorri, A. Merson, M. Moresco, M. Nonino, P. Norberg, J. Peacock, R. Pello, M. Penny, V. Pettorino, C. Di Porto, L. Pozzetti, C. Quercellini, M. Radovich, A. Rassat, N. Roche, S. Ronayette, E. Rossetti, B. Sartoris, P. Schneider, E. Semboloni, S. Serjeant, F. Simpson, C. Skordis, G. Smadja, S. Smartt, P. Spano, S. Spiro, M. Sullivan, A. Tilquin, R. Trotta, L. Verde, Y. Wang, G. Williger, G. Zhao, J. Zoubian, and E. Zucca. Euclid Definition Study Report. *arXiv e-prints*, page arXiv:1110.3193, October 2011.

[99] Željko Ivezić, Steven M. Kahn, J. Anthony Tyson, Bob Abel, Emily Acosta, Robyn Allsman, David Alonso, Yusra AlSayyad, Scott F. Anderson, John Andrew, James Roger P. Angel, George Z. Angeli, Reza Ansari, Pierre Antilogus, Constanza Araujo, Robert Armstrong, Kirk T. Arndt, Pierre Astier, Éric Aubourg, Nicole Auza, Tim S. Axelrod, Deborah J. Bard, Jeff D. Barr, Aurelian Barrau, James G. Bartlett, Amanda E. Bauer, Brian J. Bauman, Sylvain Baumont, Ellen Bechtol, Keith Bechtol, Andrew C. Becker, Jacek Becla, Cristina Beldica, Steve Bellavia, Federica B. Bianco, Rahul Biswas, Guillaume Blanc, Jonathan Blazek, Roger D. Blandford, Josh S. Bloom, Joanne Bogart, Tim W. Bond, Michael T. Booth, Anders W. Borgland, Kirk Borne, James F. Bosch, Dominique Boutigny, Craig A. Brackett, Andrew Bradshaw, William Nielsen Brandt, Michael E. Brown, James S. Bullock, Patricia Burchat, David L. Burke, Gianpietro Cagnoli, Daniel Calabrese, Shawn Callahan, Alice L. Callen, Jeffrey L. Carlin, Erin L. Carlson, Srinivasan Chandrasekharan, Glenaver Charles-Emerson, Steve Chesley, Elliott C. Cheu, Hsin-Fang Chiang, James Chiang, Carol Chirino, Derek Chow, David R. Ciardi, Charles F. Claver, Johann Cohen-Tanugi, Joseph J. Cockrum, Rebecca Coles, Andrew J. Connolly, Kem H. Cook, Asantha Cooray, Kevin R. Covey, Chris Cribbs, Wei Cui, Roc Cutri, Philip N.

Daly, Scott F. Daniel, Felipe Daruich, Guillaume Daubard, Greg Daues, William Dawson, Francisco Delgado, Alfred Dellapenna, Robert de Peyster, Miguel de Val-Borro, Seth W. Digel, Peter Doherty, Richard Dubois, Gregory P. Dubois-Felsmann, Josef Durech, Frossie Economou, Tim Eifler, Michael Eracleous, Benjamin L. Emmons, Angelo Fausti Neto, Henry Ferguson, Enrique Figueroa, Merlin Fisher-Levine, Warren Focke, Michael D. Foss, James Frank, Michael D. Freemon, Emmanuel Gangler, Eric Gawiser, John C. Geary, Perry Gee, Marla Geha, Charles J. B. Gessner, Robert R. Gibson, D. Kirk Gilmore, Thomas Glanzman, William Glick, Tatiana Goldina, Daniel A. Goldstein, Iain Goodenow, Melissa L. Graham, William J. Gressler, Philippe Gris, Leanne P. Guy, Augustin Guyonnet, Gunther Haller, Ron Harris, Patrick A. Hascall, Justine Haupt, Fabio Hernandez, Sven Herrmann, Edward Hileman, Joshua Hoblitt, John A. Hodgson, Craig Hogan, James D. Howard, Dajun Huang, Michael E. Huffer, Patrick Ingraham, Walter R. Innes, Suzanne H. Jacoby, Bhuvnesh Jain, Fabrice Jammes, M. James Jee, Tim Jenness, Garrett Jernigan, Darko Jevremović, Kenneth Johns, Anthony S. Johnson, Margaret W. G. Johnson, R. Lynne Jones, Claire Juramy-Gilles, Mario Jurić, Jason S. Kalirai, Nitya J. Kallivayalil, Bryce Kalmbach, Jeffrey P. Kantor, Pierre Karst, Mansi M. Kasliwal, Heather Kelly, Richard Kessler, Veronica Kinnison, David Kirkby, Lloyd Knox, Ivan V. Kotov, Victor L. Krabbendam, K. Simon Krughoff, Petr Kubánek, John Kuczewski, Shri Kulkarni, John Ku, Nadine R. Kurita, Craig S. Lage, Ron Lambert, Travis Lange, J. Brian Langton, Laurent Le Guillou, Deborah Levine, Ming Liang, Kian-Tat Lim, Chris J. Lintott, Kevin E. Long, Margaux Lopez, Paul J. Lotz, Robert H. Lupton, Nate B. Lust, Lauren A. MacArthur, Ashish Mahabal, Rachel Mandelbaum, Thomas W. Markiewicz, Darren S. Marsh, Philip J. Marshall, Stuart Marshall, Morgan May, Robert McKercher, Michelle McQueen, Joshua Meyers, Myriam Migliore, Michelle Miller, David J. Mills, Connor Miraval, Joachim Moeyens, Fred E. Moolekamp, David G. Monet, Marc Moniez, Serge Monkewitz, Christopher Montgomery, Christopher B. Morrison, Fritz Mueller, Gary P. Muller, Freddy Muñoz Arancibia, Douglas R. Neill, Scott P. Newbry, Jean-Yves Nief, Andrei Nomerotski, Martin Nordby, Paul O'Connor, John Oliver, Scot S. Olivier, Knut Olsen, William O'Mullane, Sandra Ortiz, Shawn Osier, Russell E. Owen, Reynald Pain, Paul E. Palecek, John K. Parejko, James B. Parsons, Nathan M. Pease, J. Matt Peterson, John R. Peterson, Donald L. Petravick, M. E. Libby Petrick, Cathy E. Petry, Francesco Pierfederici, Stephen Pietrowicz, Rob Pike, Philip A. Pinto, Raymond Plante, Stephen Plate, Joel P. Plutchak, Paul A. Price, Michael Prouza, Veljko Radeka, Jayadev Rajagopal, Andrew P. Rasmussen, Nicolas Regnault, Kevin A. Reil, David J. Reiss, Michael A. Reuter, Stephen T. Ridgway, Vincent J. Riot, Steve Ritz, Sean Robinson, William Roby, Aaron Roodman, Wayne Rosing, Cecille Roucelle, Matthew R. Rumore, Stefano Russo, Abhijit Saha, Benoit Sassolas, Terry L. Schalk, Pim Schellart, Rafe H. Schindler, Samuel Schmidt, Donald P. Schneider, Michael D. Schneider, William Schoening, German Schumacher, Megan E. Schwamb, Jacques Sebag, Brian Selvy, Glenn H. Sembroski, Lynn G. Seppala, Andrew Serio, Eduardo Serrano, Richard A. Shaw, Ian Shipsey, Jonathan Sick, Nicole Silvestri, Colin T. Slater, J. Allyn Smith, R. Chris Smith, Shahram Sobhani, Christine Soldahl, Lisa Storrie-Lombardi, Edward Stover, Michael A. Strauss, Rachel A. Street,

Christopher W. Stubbs, Ian S. Sullivan, Donald Sweeney, John D. Swinbank, Alexander Szalay, Peter Takacs, Stephen A. Tether, Jon J. Thaler, John Gregg Thayer, Sandrine Thomas, Adam J. Thornton, Vaikunth Thukral, Jeffrey Tice, David E. Trilling, Max Turri, Richard Van Berg, Daniel Vanden Berk, Kurt Vetter, Francoise Virieux, Tomislav Vucina, William Wahl, Lucianne Walkowicz, Brian Walsh, Christopher W. Walter, Daniel L. Wang, Shin-Yawn Wang, Michael Warner, Oliver Wiecha, Beth Willman, Scott E. Winters, David Wittman, Sidney C. Wolff, W. Michael Wood-Vasey, Xiuqin Wu, Bo Xin, Peter Yoachim, and Hu Zhan. LSST: From Science Drivers to Reference Design and Anticipated Data Products. , 873(2):111, March 2019.

[100] Piero Madau. The intergalactic medium, 2000.

[101] Diego Blas, Julien Lesgourgues, and Thomas Tram. The cosmic linear anisotropy solving system (class). part ii: Approximation schemes. *Journal of Cosmology and Astroparticle Physics*, 2011(07):034–034, Jul 2011.

[102] Antony Lewis, Anthony Challinor, and Anthony Lasenby. Efficient computation of cosmic microwave background anisotropies in closed friedmann-robertson-walker models. *The Astrophysical Journal*, 538(2):473–476, Aug 2000.

[103] Ariyeh H. Maller, Daniel H. McIntosh, Neal Katz, and Martin D. Weinberg. The Galaxy Angular Correlation Functions and Power Spectrum from the Two Micron All Sky Survey. , 619(1):147–160, January 2005.

[104] Samuel J. Schmidt, Brice Ménard, Ryan Scranton, Christopher Morrison, and Cameron K. McBride. Recovering redshift distributions with cross-correlations: pushing the boundaries. , 431(4):3307–3318, June 2013.

[105] Mubdi Rahman, Brice Ménard, Ryan Scranton, Samuel J. Schmidt, and Christopher B. Morrison. Clustering-based redshift estimation: comparison to spectroscopic redshifts. , 447(4):3500–3511, March 2015.

[106] L. Wolz, C. Blake, and J. S. B. Wyithe. Determining the hi content of galaxies via intensity mapping cross-correlations. *Monthly Notices of the Royal Astronomical Society*, 470(3):3220?3226, Jun 2017.

[107] Beth Reid, Shirley Ho, Nikhil Padmanabhan, Will J. Percival, Jeremy Tinker, Rita Tojeiro, Martin White, Daniel J. Eisenstein, Claudia Maraston, Ashley J. Ross, Ariel G. Sánchez, David Schlegel, Erin Sheldon, Michael A. Strauss, Daniel Thomas, David Wake, Florian Beutler, Dmitry Bizyaev, Adam S. Bolton, Joel R. Brownstein, Chia-Hsun Chuang, Kyle Dawson, Paul Harding, Francisco-Shu Kitaura, Alexie Leauthaud, Karen Masters, Cameron K. McBride, Surhud More, Matthew D. Olmstead, Daniel Oravetz, Sebastián E. Nuza, Kaike Pan, John Parejko, Janine Pforr, Francisco Prada, Sergio Rodríguez-Torres, Salvador Salazar-Albornoz, Lado Samushia, Donald P. Schneider, Claudia G. Scóccola, Audrey Simmons, and Mariana Vargas-Magana. SDSS-III Baryon Oscillation Spectroscopic Survey Data Release 12: galaxy target selection and large-scale structure catalogues. , 455(2):1553–1573, January 2016.

[108] Ashley J. Ross, Julian Bautista, Rita Tojeiro, Shadab Alam, Stephen Bailey, Etienne Burtin, Johan Comparat, Kyle S. Dawson, Arnaud de Mattia, Hélion du Mas des Bourboux, Héctor Gil-Marín, Jiamin Hou, Hui Kong, Brad W. Lyke, Faizan G. Mohammad, John Moustakas, Eva-Maria Mueller, Adam D. Myers, Will J. Percival, Anand Raichoor, Mehdi Rezaie, Hee-Jong Seo, Alex Smith, Jeremy L. Tinker, Pauline Zarrouk, Cheng Zhao, Gong-Bo Zhao, Dmitry Bizyaev, Jonathan Brinkmann, Joel R. Brownstein, Aurelio Carnero Rosell, Solène Chabanier, Peter D. Choi, Chia-Hsun Chuang, Irene Cruz-Gonzalez, Axel de la Macorra, Sylvain de la Torre, Stephanie Escoffier, Sebastien Fromenteau, Alexandra Higley, Eric Jullo, Jean-Paul Kneib, Jacob N. McLane, Andrea Muñoz-Gutiérrez, Richard Neveux, Jeffrey A. Newman, Christian Nitschelm, Nathalie Palanque-Delabrouille, Romain Paviot, Anthony R. Pullen, Graziano Rossi, Vanina Ruhlmann-Kleider, Donald P. Schneider, Mariana Vargas Magaña, M. Vivek, and Yucheng Zhang. The Completed SDSS-IV extended Baryon Oscillation Spectroscopic Survey: Large-scale structure catalogues for cosmological analysis. , 498(2):2354–2371, October 2020.

[109] Isabelle Pâris, Patrick Petitjean, Nicholas P. Ross, Adam D. Myers, Éric Aubourg, Alina Streblyanska, Stephen Bailey, Éric Armengaud, Nathalie Palanque-Delabrouille, Christophe Yèche, Fred Hamann, Michael A. Strauss, Franco D. Albareti, Jo Bovy, Dmitry Bizyaev, W. Niel Brandt, Marcella Brusa, Johannes Buchner, Johan Comparat, Rupert A. C. Croft, Tom Dwelly, Xiaohui Fan, Andreu Font-Ribera, Jian Ge, Antonis Georgakakis, Patrick B. Hall, Linhua Jiang, Karen Kinemuchi, Elena Malanushenko, Viktor Malanushenko, Richard G. McMahon, Marie-Luise Menzel, Andrea Merloni, Kirpal Nandra, Pasquier Noterdaeme, Daniel Oravetz, Kaike Pan, Matthew M. Pieri, Francisco Prada, Mara Salvato, David J. Schlegel, Donald P. Schneider, Audrey Simmons, Matteo Viel, David H. Weinberg, and Liu Zhu. The Sloan Digital Sky Survey Quasar Catalog: Twelfth data release. , 597:A79, January 2017.

[110] Isabelle Pâris, Patrick Petitjean, Éric Aubourg, Adam D. Myers, Alina Streblyanska, Brad W. Lyke, Scott F. Anderson, Éric Armengaud, Julian Bautista, Michael R. Blanton, Michael Blomqvist, Jonathan Brinkmann, Joel R. Brownstein, William Nielsen Brandt, Étienne Burtin, Kyle Dawson, Sylvain de la Torre, Antonis Georgakakis, Héctor Gil-Marín, Paul J. Green, Patrick B. Hall, Jean-Paul Kneib, Stephanie M. LaMassa, Jean-Marc Le Goff, Chelsea MacLeod, Vivek Mariappan, Ian D. McGreer, Andrea Merloni, Pasquier Noterdaeme, Nathalie Palanque-Delabrouille, Will J. Percival, Ashley J. Ross, Graziano Rossi, Donald P. Schneider, Hee-Jong Seo, Rita Tojeiro, Benjamin A. Weaver, Anne-Marie Weijmans, Christophe Yèche, Pauline Zarrouk, and Gong-Bo Zhao. The Sloan Digital Sky Survey Quasar Catalog: Fourteenth data release. , 613:A51, May 2018.

[111] DESI Collaboration, Amir Aghamousa, Jessica Aguilar, Steve Ahlen, Shadab Alam, Lori E. Allen, Carlos Allende Prieto, James Annis, Stephen Bailey, Christophe Balland, Otger Ballester, Charles Baltay, Lucas Beaufore, Chris Bebek, Timothy C. Beers, Eric F. Bell, José Luis Bernal, Robert Besuner, Florian Beutler, Chris Blake, Hannes Bleuler, Michael Blomqvist, Robert Blum, Adam S. Bolton, Cesar Briceno,

David Brooks, Joel R. Brownstein, Elizabeth Buckley-Geer, Angela Burden, Etienne Burtin, Nicolas G. Busca, Robert N. Cahn, Yan-Chuan Cai, Laia Cardiel-Sas, Raymond G. Carlberg, Pierre-Henri Carton, Ricard Casas, Francisco J. Castander, Jorge L. Cervantes-Cota, Todd M. Claybaugh, Madeline Close, Carl T. Coker, Shaun Cole, Johan Comparat, Andrew P. Cooper, M. C. Cousinou, Martin Crocce, Jean-Gabriel Cuby, Daniel P. Cunningham, Tamara M. Davis, Kyle S. Dawson, Axel de la Macorra, Juan De Vicente, Timothée Delubac, Mark Derwent, Arjun Dey, Govinda Dhungana, Zhejie Ding, Peter Doel, Yutong T. Duan, Anne Ealet, Jerry Edelstein, Sarah Eftekharzadeh, Daniel J. Eisenstein, Ann Elliott, Stéphanie Escoffier, Matthew Evatt, Parker Fagrelius, Xiaohui Fan, Kevin Fanning, Arya Farahi, Jay Farihi, Ginevra Favole, Yu Feng, Enrique Fernandez, Joseph R. Findlay, Douglas P. Finkbeiner, Michael J. Fitzpatrick, Brenna Flaugher, Samuel Flender, Andreu Font-Ribera, Jaime E. Forero-Romero, Pablo Fosalba, Carlos S. Frenk, Michele Fumagalli, Boris T. Gaensicke, Giuseppe Gallo, Juan Garcia-Bellido, Enrique Gaztanaga, Nicola Pietro Gentile Fusillo, Terry Gerard, Irena Gershkovich, Tommaso Giannantonio, Denis Gillet, Guillermo Gonzalez de Rivera, Violeta Gonzalez-Perez, Shelby Gott, Or Graur, Gaston Gutierrez, Julien Guy, Salman Habib, Henry Heetderks, Ian Heetderks, Katrin Heitmann, Wojciech A. Hellwing, David A. Herrera, Shirley Ho, Stephen Holland, Klaus Honscheid, Eric Huff, Timothy A. Hutchinson, Dragan Huterer, Ho Seong Hwang, Joseph Maria Illa Laguna, Yuzo Ishikawa, Dianna Jacobs, Niall Jeffrey, Patrick Jelinsky, Elise Jennings, Linhua Jiang, Jorge Jimenez, Jennifer Johnson, Richard Joyce, Eric Jullo, Stéphanie Juneau, Sami Kama, Armin Karcher, Sonia Karkar, Robert Kehoe, Noble Kennamer, Stephen Kent, Martin Kilbinger, Alex G. Kim, David Kirkby, Theodore Kisner, Ellie Kitanidis, Jean-Paul Kneib, Sergey Koposov, Eve Kovacs, Kazuya Koyama, Anthony Kremin, Richard Kron, Luzius Kronig, Andrea Kueter-Young, Cedric G. Lacey, Robin Lafever, Ofer Lahav, Andrew Lambert, Michael Lampton, Martin Landriau, Dustin Lang, Tod R. Lauer, Jean-Marc Le Goff, Laurent Le Guillou, Auguste Le Van Suu, Jae Hyeon Lee, Su-Jeong Lee, Daniela Leitner, Michael Lesser, Michael E. Levi, Benjamin L'Huillier, Baojiu Li, Ming Liang, Huan Lin, Eric Linder, Sarah R. Loebman, Zarija Lukić, Jun Ma, Niall MacCrann, Christophe Magneville, Laleh Makarem, Marc Manera, Christopher J. Manser, Robert Marshall, Paul Martini, Richard Massey, Thomas Matheson, Jeremy McCauley, Patrick McDonald, Ian D. McGreer, Aaron Meisner, Nigel Metcalfe, Timothy N. Miller, Ramon Miquel, John Moustakas, Adam Myers, Milind Naik, Jeffrey A. Newman, Robert C. Nichol, Andrina Nicola, Luiz Nicolati da Costa, Jundan Nie, Gustavo Niz, Peder Norberg, Brian Nord, Dara Norman, Peter Nugent, Thomas O'Brien, Minji Oh, Knut A. G. Olsen, Cristobal Padilla, Hamsa Padmanabhan, Nikhil Padmanabhan, Nathalie Palanque-Delabrouille, Antonella Palmese, Daniel Pappalardo, Isabelle Pâris, Changbom Park, Anna Patej, John A. Peacock, Hiranya V. Peiris, Xiyan Peng, Will J. Percival, Sandrine Perruchot, Matthew M. Pieri, Richard Pogge, Jennifer E. Pollack, Claire Poppett, Francisco Prada, Abhishek Prakash, Ronald G. Probst, David Rabinowitz, Anand Raichoor, Chang Hee Ree, Alexandre Refregier, Xavier Regal, Beth Reid, Kevin Reil, Mehdi Rezaie, Constance M. Rockosi, Natalie Roe, Samuel Ronayette, Aaron Roodman, Ashley J. Ross, Nicholas P. Ross, Graziano

Rossi, Eduardo Rozo, Vanina Ruhlmann-Kleider, Eli S. Rykoff, Cristiano Sabiu, Lado Samushia, Eusebio Sanchez, Javier Sanchez, David J. Schlegel, Michael Schneider, Michael Schubnell, Aurélia Secroun, Uros Seljak, Hee-Jong Seo, Santiago Serrano, Arman Shafieloo, Huanyuan Shan, Ray Sharples, Michael J. Sholl, William V. Shourt, Joseph H. Silber, David R. Silva, Martin M. Sirk, Anze Slosar, Alex Smith, George F. Smoot, Debopam Som, Yong-Seon Song, David Sprayberry, Ryan Staten, Andy Stefanik, Gregory Tarle, Suk Sien Tie, Jeremy L. Tinker, Rita Tojeiro, Francisco Valdes, Octavio Valenzuela, Monica Valluri, Mariana Vargas-Magana, Licia Verde, Alistair R. Walker, Jiali Wang, Yuting Wang, Benjamin A. Weaver, Curtis Weaverdyck, Risa H. Wechsler, David H. Weinberg, Martin White, Qian Yang, Christophe Yeche, Tianmeng Zhang, Gong-Bo Zhao, Yi Zheng, Xu Zhou, Zhimin Zhou, Yaling Zhu, Hu Zou, and Ying Zu. The desi experiment part i: Science,targeting, and survey design, 2016.

[112] Alison L. Coil, Jeffrey A. Newman, Nick Kaiser, Marc Davis, Chung-Pei Ma, Dale D. Kocevski, and David C. Koo. Evolution and Color Dependence of the Galaxy Angular Correlation Function: 350,000 Galaxies in 5 Square Degrees. , 617(2):765–781, December 2004.

[113] Patrick Morrissey, David Schiminovich, Tom A. Barlow, D. Christopher Martin, Brian Blakkolb, Tim Conrow, Brian Cooke, Kerry Erickson, James Fanson, Peter G. Friedman, Robert Grange, Patrick N. Jelinsky, Siu-Chun Lee, Dankai Liu, Alan Mazer, Ryan McLean, Bruno Milliard, David Randall, Wes Schmitigal, Amit Sen, Oswald H. W. Siegmund, Frank Surber, Arthur Vaughan, Maurice Viton, Barry Y. Welsh, Luciana Bianchi, Yong-Ik Byun, Jose Donas, Karl Forster, Timothy M. Heckman, Young-Wook Lee, Barry F. Madore, Roger F. Malina, Susan G. Neff, R. Michael Rich, Todd Small, Alex S. Szalay, and Ted K. Wyder. The On-Orbit Performance of the Galaxy Evolution Explorer. , 619(1):L7–L10, January 2005.

[114] Benjamin P. Moster, Rachel S. Somerville, Jeffrey A. Newman, and Hans-Walter Rix. A cosmic variance cookbook. *The Astrophysical Journal*, 731(2):113, Mar 2011.

[115] Yi-Kuan Chiang, Ryu Makiya, Brice Ménard, and Eiichiro Komatsu. The Cosmic Thermal History Probed by Sunyaev-Zeldovich Effect Tomography. , 902(1):56, October 2020.

[116] V. Scottez, A. Benoit-Lévy, J. Coupon, O. Ilbert, and Y. Mellier. Testing the accuracy of clustering redshifts with simulations. , 474(3):3921–3930, March 2018.

[117] Daniel Foreman-Mackey, David W. Hogg, Dustin Lang, and Jonathan Goodman. emcee: The mcmc hammer. *Publications of the Astronomical Society of the Pacific*, 125(925):306?312, Mar 2013.

[118] Steven L. Finkelstein, Casey Papovich, Brett Salmon, Kristian Finlator, Mark Dickinson, Henry C. Ferguson, Mauro Giavalisco, Anton M. Koekemoer, Naveen A. Reddy, Robert Bassett, Christopher J. Conselice, James S. Dunlop, S. M. Faber, Norman A. Grogin, Nimish P. Hathi, Dale D. Kocevski, Kamson Lai, Kyoung-Soo Lee, Ross J. McLure, Bahram Mobasher, and Jeffrey A. Newman. Candels: The Evolution of Galaxy Rest-frame Ultraviolet Colors from z = 8 to 4. , 756(2):164, September 2012.

[119] Brian Siana, Harry I. Teplitz, Henry C. Ferguson, Thomas M. Brown, Mauro Giavalisco, Mark Dickinson, Ranga-Ram Chary, Duilia F. de Mello, Christopher J. Conselice, Carrie R. Bridge, Jonathan P. Gardner, James W. Colbert, and Claudia Scarlata. A Deep Hubble Space Telescope Search for Escaping Lyman Continuum Flux at z ~1.3: Evidence for an Evolving Ionizing Emissivity. , 723(1):241–250, November 2010.

[120] Brian Siana, Alice E. Shapley, Kristin R. Kulas, Daniel B. Nestor, Charles C. Steidel, Harry I. Teplitz, Anahita Alavi, Thomas M. Brown, Christopher J. Conselice, Henry C. Ferguson, Mark Dickinson, Mauro Giavalisco, James W. Colbert, Carrie R. Bridge, Jonathan P. Gardner, and Duilia F. de Mello. A Deep Hubble Space Telescope and Keck Search for Definitive Identification of Lyman Continuum Emitters at z~3.1. , 804(1):17, May 2015.

[121] Nickolay Y. Gnedin, Andrey V. Kravtsov, and Hsiao-Wen Chen. Escape of Ionizing Radiation from High-Redshift Galaxies. , 672(2):765–775, January 2008.

[122] John H. Wise and Renyue Cen. Ionizing Photon Escape Fractions From High-Redshift Dwarf Galaxies. , 693(1):984–999, March 2009.

[123] Lauren Anderson, F. Governato, M. Karcher, T. Quinn, and J. Wadsley. The little Galaxies that could (reionize the universe): predicting faint end slopes & escape fractions at z¿4. , 468(4):4077–4092, July 2017.

[124] Jordi Miralda-Escudé, Martin Haehnelt, and Martin J. Rees. Reionization of the Inhomogeneous Universe. , 530(1):1–16, February 2000.

[125] Akio K. Inoue, Ikkoh Shimizu, Ikuru Iwata, and Masayuki Tanaka. An updated analytic model for attenuation by the intergalactic medium. , 442(2):1805–1820, August 2014.

[126] Kalevi Mattila, Kimmo Lehtinen, Petri Väisänen, Gerhard von Appen-Schnur, and Christoph Leinert. Spectrophotometric measurement of the Extragalacic Background Light. In Richard J. Tuffs and Cristina C. Popescu, editors, *The Spectral Energy Distribution of Galaxies - SED 2011*, volume 284 of *IAU Symposium*, pages 429–436, August 2012.

[127] D. Spergel, N. Gehrels, C. Baltay, D. Bennett, J. Breckinridge, M. Donahue, A. Dressler, B. S. Gaudi, T. Greene, O. Guyon, C. Hirata, J. Kalirai, N. J. Kasdin, B. Macintosh, W. Moos, S. Perlmutter, M. Postman, B. Rauscher, J. Rhodes, Y. Wang, D. Weinberg, D. Benford, M. Hudson, W. S. Jeong, Y. Mellier, W. Traub, T. Yamada, P. Capak, J. Colbert, D. Masters, M. Penny, D. Savransky, D. Stern, N. Zimmerman, R. Barry, L. Bartusek, K. Carpenter, E. Cheng, D. Content, F. Dekens, R. Demers, K. Grady, C. Jackson, G. Kuan, J. Kruk, M. Melton, B. Nemati, B. Parvin, I. Poberezhskiy, C. Peddie, J. Ruffa, J. K. Wallace, A. Whipple, E. Wollack, and F. Zhao. Wide-field infrarred survey telescope-astrophysics focused telescope assets wfirst-afta 2015 report, 2015.

[128] Akira Konno, Masami Ouchi, Kimihiko Nakajima, Florent Duval, Haruka Kusakabe, Yoshiaki Ono, and Kazuhiro Shimasaku. Bright and Faint Ends of Lyα Luminosity Functions at z = 2 Determined by the Subaru Survey: Implications for AGNs, Magnification Bias, and ISM H I Evolution. , 823(1):20, May 2016.

[129] Alison L. Coil, Antonis Georgakakis, Jeffrey A. Newman, Michael C. Cooper, Darren Croton, Marc Davis, David C. Koo, Elise S. Laird, Kirpal Nandra, Benjamin J. Weiner, and et al. Aegis: The clustering of x-ray active galactic nucleus relative to galaxies atz 1. *The Astrophysical Journal*, 701(2):1484–1499, Jul 2009.

[130] Ravi K. Sheth and Giuseppe Tormen. Large-scale bias and the peak background split. *Monthly Notices of the Royal Astronomical Society*, 308(1):119–126, Sep 1999.

[131] Xiaohui Fan, Michael A. Strauss, Robert H. Becker, Richard L. White, James E. Gunn, Gillian R. Knapp, Gordon T. Richards, Donald P. Schneider, J. Brinkmann, and Masataka Fukugita. Constraining the Evolution of the Ionizing Background and the Epoch of Reionization with z˜6 Quasars. II. A Sample of 19 Quasars. , 132(1):117–136, July 2006.

[132] Girish Kulkarni, Laura C. Keating, Martin G. Haehnelt, Sarah E. I. Bosman, Ewald Puchwein, Jonathan Chardin, and Dominique Aubert. Large Ly α opacity fluctuations and low CMB τ in models of late reionization with large islands of neutral hydrogen extending to z ¡ 5.5. , 485(1):L24–L28, May 2019.

[133] Laura C. Keating, Lewis H. Weinberger, Girish Kulkarni, Martin G. Haehnelt, Jonathan Chardin, and Dominique Aubert. Long troughs in the Lyman-α forest below redshift 6 due to islands of neutral hydrogen. , 491(2):1736–1745, January 2020.

[134] Fahad Nasir and Anson D'Aloisio. Observing the tail of reionization: neutral islands in the z = 5.5 Lyman-α forest. , 494(3):3080–3094, May 2020.

[135] Kamson Lai, Jia-Sheng Huang, Giovanni Fazio, Eric Gawiser, Robin Ciardullo, Maaike Damen, Marijn Franx, Caryl Gronwall, Ivo Labbe, Georgios Magdis, and Pieter van Dokkum. Spitzer Constraints on the Stellar Populations of Lyα-Emitting Galaxies at z = 3.1. , 674(1):70–74, February 2008.

[136] G. Bruzual and S. Charlot. Stellar population synthesis at the resolution of 2003. , 344(4):1000–1028, October 2003.

[137] The LUVOIR Team. The LUVOIR Mission Concept Study Final Report. *arXiv e-prints*, page arXiv:1912.06219, December 2019.

[138] George D. Becker and James S. Bolton. New measurements of the ionizing ultraviolet background over 2 ¡ z ¡ 5 and implications for hydrogen reionization. , 436(2):1023–1039, December 2013.

[139] S. Perlmutter, G. Aldering, G. Goldhaber, R. A. Knop, P. Nugent, P. G. Castro, S. Deustua, S. Fabbro, A. Goobar, D. E. Groom, I. M. Hook, A. G. Kim, M. Y. Kim, J. C. Lee, N. J. Nunes, R. Pain, C. R. Pennypacker, R. Quimby, C. Lidman, R. S. Ellis, M. Irwin, R. G. McMahon, P. Ruiz-Lapuente, N. Walton, B. Schaefer, B. J.

Boyle, A. V. Filippenko, T. Matheson, A. S. Fruchter, N. Panagia, H. J. M. Newberg, W. J. Couch, and The Supernova Cosmology Project. Measurements of Ω and Λ from 42 High-Redshift Supernovae. , 517(2):565–586, June 1999.

[140] N. Aghanim, Y. Akrami, M. Ashdown, J. Aumont, C. Baccigalupi, M. Ballardini, A. J. Banday, R. B. Barreiro, N. Bartolo, and et al. Planck 2018 results. *Astronomy Astrophysics*, 641:A6, Sep 2020.

[141] Yun Wang. Dark energy constraints from baryon acoustic oscillations. *The Astrophysical Journal*, 647(1):1–7, Aug 2006.

[142] Baojiu Li and Kazuya Koyama. *Modified Gravity*. WORLD SCIENTIFIC, 2019.

[143] M.A. Troxel, N. MacCrann, J. Zuntz, T.F. Eifler, E. Krause, S. Dodelson, D. Gruen, J. Blazek, O. Friedrich, S. Samuroff, and et al. Dark energy survey year 1 results: Cosmological constraints from cosmic shear. *Physical Review D*, 98(4), Aug 2018.

[144] Alireza Hojjati, Levon Pogosian, and Gong-Bo Zhao. Testing gravity with camb and cosmomc. *Journal of Cosmology and Astroparticle Physics*, 2011(08):005–005, Aug 2011.

[145] Simone Peirone, Kazuya Koyama, Levon Pogosian, Marco Raveri, and Alessandra Silvestri. Large-scale structure phenomenology of viable horndeski theories. *Physical Review D*, 97(4), Feb 2018.

[146] A. Mantz, S. W. Allen, H. Ebeling, and D. Rapetti. New constraints on dark energy from the observed growth of the most X-ray luminous galaxy clusters. , 387(3):1179–1192, July 2008.

[147] David Rapetti, Steven W. Allen, and Adam Mantz. The prospects for constraining dark energy with future x-ray cluster gas mass fraction measurements. *Monthly Notices of the Royal Astronomical Society*, 388(3):1265–1278, Aug 2008.

[148] C.D. Kreisch and E. Komatsu. Cosmological constraints on horndeski gravity in light of gw170817. *Journal of Cosmology and Astroparticle Physics*, 2018(12):030–030, Dec 2018.

[149] A Spurio Mancini, F Köhlinger, B Joachimi, V Pettorino, B M Schäfer, R Reischke, E van Uitert, S Brieden, M Archidiacono, and J Lesgourgues. KiDS GAMA: constraints on horndeski gravity from combined large-scale structure probes. *Monthly Notices of the Royal Astronomical Society*, 490(2):2155–2177, sep 2019.

[150] Johannes Noller and Andrina Nicola. Cosmological parameter constraints for horndeski scalar-tensor gravity. *Physical Review D*, 99(10), May 2019.

[151] T. Baker, E. Bellini, P. G. Ferreira, M. Lagos, J. Noller, and I. Sawicki. Strong Constraints on Cosmological Gravity from GW170817 and GRB 170817A. , 119(25):251301, December 2017.

[152] Shun Arai and Atsushi Nishizawa. Generalized framework for testing gravity with gravitational-wave propagation. II. Constraints on Horndeski theory. , 97(10):104038, May 2018.

[153] Željko Ivezić, Steven M. Kahn, J. Anthony Tyson, Bob Abel, Emily Acosta, Robyn Allsman, David Alonso, Yusra AlSayyad, Scott F. Anderson, John Andrew, James Roger P. Angel, George Z. Angeli, Reza Ansari, Pierre Antilogus, Constanza Araujo, Robert Armstrong, Kirk T. Arndt, Pierre Astier, Éric Aubourg, Nicole Auza, Tim S. Axelrod, Deborah J. Bard, Jeff D. Barr, Aurelian Barrau, James G. Bartlett, Amanda E. Bauer, Brian J. Bauman, Sylvain Baumont, Ellen Bechtol, Keith Bechtol, Andrew C. Becker, Jacek Becla, Cristina Beldica, Steve Bellavia, Federica B. Bianco, Rahul Biswas, Guillaume Blanc, Jonathan Blazek, Roger D. Blandford, Josh S. Bloom, Joanne Bogart, Tim W. Bond, Michael T. Booth, Anders W. Borgland, Kirk Borne, James F. Bosch, Dominique Boutigny, Craig A. Brackett, Andrew Bradshaw, William Nielsen Brandt, Michael E. Brown, James S. Bullock, Patricia Burchat, David L. Burke, Gianpietro Cagnoli, Daniel Calabrese, Shawn Callahan, Alice L. Callen, Jeffrey L. Carlin, Erin L. Carlson, Srinivasan Chandrasekharan, Glenaver Charles-Emerson, Steve Chesley, Elliott C. Cheu, Hsin-Fang Chiang, James Chiang, Carol Chirino, Derek Chow, David R. Ciardi, Charles F. Claver, Johann Cohen-Tanugi, Joseph J. Cockrum, Rebecca Coles, Andrew J. Connolly, Kem H. Cook, Asantha Cooray, Kevin R. Covey, Chris Cribbs, Wei Cui, Roc Cutri, Philip N. Daly, Scott F. Daniel, Felipe Daruich, Guillaume Daubard, Greg Daues, William Dawson, Francisco Delgado, Alfred Dellapenna, Robert de Peyster, Miguel de Val-Borro, Seth W. Digel, Peter Doherty, Richard Dubois, Gregory P. Dubois-Felsmann, Josef Durech, Frossie Economou, Tim Eifler, Michael Eracleous, Benjamin L. Emmons, Angelo Fausti Neto, Henry Ferguson, Enrique Figueroa, Merlin Fisher-Levine, Warren Focke, Michael D. Foss, James Frank, Michael D. Freemon, Emmanuel Gangler, Eric Gawiser, John C. Geary, Perry Gee, Marla Geha, Charles J. B. Gessner, Robert R. Gibson, D. Kirk Gilmore, Thomas Glanzman, William Glick, Tatiana Goldina, Daniel A. Goldstein, Iain Goodenow, Melissa L. Graham, William J. Gressler, Philippe Gris, Leanne P. Guy, Augustin Guyonnet, Gunther Haller, Ron Harris, Patrick A. Hascall, Justine Haupt, Fabio Hernandez, Sven Herrmann, Edward Hileman, Joshua Hoblitt, John A. Hodgson, Craig Hogan, James D. Howard, Dajun Huang, Michael E. Huffer, Patrick Ingraham, Walter R. Innes, Suzanne H. Jacoby, Bhuvnesh Jain, Fabrice Jammes, M. James Jee, Tim Jenness, Garrett Jernigan, Darko Jevremović, Kenneth Johns, Anthony S. Johnson, Margaret W. G. Johnson, R. Lynne Jones, Claire Juramy-Gilles, Mario Jurić, Jason S. Kalirai, Nitya J. Kallivayalil, Bryce Kalmbach, Jeffrey P. Kantor, Pierre Karst, Mansi M. Kasliwal, Heather Kelly, Richard Kessler, Veronica Kinnison, David Kirkby, Lloyd Knox, Ivan V. Kotov, Victor L. Krabbendam, K. Simon Krughoff, Petr Kubánek, John Kuczewski, Shri Kulkarni, John Ku, Nadine R. Kurita, Craig S. Lage, Ron Lambert, Travis Lange, J. Brian Langton, Laurent Le Guillou, Deborah Levine, Ming Liang, Kian-Tat Lim, Chris J. Lintott, Kevin E. Long, Margaux Lopez, Paul J. Lotz, Robert H. Lupton, Nate B. Lust, Lauren A. MacArthur, Ashish Mahabal, Rachel Mandelbaum, Thomas W. Markiewicz, Darren S. Marsh, Philip J. Marshall, Stuart Marshall, Morgan May, Robert McKercher, Michelle McQueen, Joshua Meyers, Myriam Migliore, Michelle Miller, David J. Mills, Connor Miraval, Joachim Moeyens, Fred E. Moolekamp, David G. Monet, Marc Moniez, Serge Monkewitz, Christopher Montgomery, Christopher B. Morrison, Fritz

Mueller, Gary P. Muller, Freddy Muñoz Arancibia, Douglas R. Neill, Scott P. Newbry, Jean-Yves Nief, Andrei Nomerotski, Martin Nordby, Paul O'Connor, John Oliver, Scot S. Olivier, Knut Olsen, William O'Mullane, Sandra Ortiz, Shawn Osier, Russell E. Owen, Reynald Pain, Paul E. Palecek, John K. Parejko, James B. Parsons, Nathan M. Pease, J. Matt Peterson, John R. Peterson, Donald L. Petravick, M. E. Libby Petrick, Cathy E. Petry, Francesco Pierfederici, Stephen Pietrowicz, Rob Pike, Philip A. Pinto, Raymond Plante, Stephen Plate, Joel P. Plutchak, Paul A. Price, Michael Prouza, Veljko Radeka, Jayadev Rajagopal, Andrew P. Rasmussen, Nicolas Regnault, Kevin A. Reil, David J. Reiss, Michael A. Reuter, Stephen T. Ridgway, Vincent J. Riot, Steve Ritz, Sean Robinson, William Roby, Aaron Roodman, Wayne Rosing, Cecille Roucelle, Matthew R. Rumore, Stefano Russo, Abhijit Saha, Benoit Sassolas, Terry L. Schalk, Pim Schellart, Rafe H. Schindler, Samuel Schmidt, Donald P. Schneider, Michael D. Schneider, William Schoening, German Schumacher, Megan E. Schwamb, Jacques Sebag, Brian Selvy, Glenn H. Sembroski, Lynn G. Seppala, Andrew Serio, Eduardo Serrano, Richard A. Shaw, Ian Shipsey, Jonathan Sick, Nicole Silvestri, Colin T. Slater, J. Allyn Smith, R. Chris Smith, Shahram Sobhani, Christine Soldahl, Lisa Storrie-Lombardi, Edward Stover, Michael A. Strauss, Rachel A. Street, Christopher W. Stubbs, Ian S. Sullivan, Donald Sweeney, John D. Swinbank, Alexander Szalay, Peter Takacs, Stephen A. Tether, Jon J. Thaler, John Gregg Thayer, Sandrine Thomas, Adam J. Thornton, Vaikunth Thukral, Jeffrey Tice, David E. Trilling, Max Turri, Richard Van Berg, Daniel Vanden Berk, Kurt Vetter, Francoise Virieux, Tomislav Vucina, William Wahl, Lucianne Walkowicz, Brian Walsh, Christopher W. Walter, Daniel L. Wang, Shin-Yawn Wang, Michael Warner, Oliver Wiecha, Beth Willman, Scott E. Winters, David Wittman, Sidney C. Wolff, W. Michael Wood-Vasey, Xiuqin Wu, Bo Xin, Peter Yoachim, and Hu Zhan. LSST: From Science Drivers to Reference Design and Anticipated Data Products. , 873(2):111, March 2019.

[154] D. Spergel, N. Gehrels, C. Baltay, D. Bennett, J. Breckinridge, M. Donahue, A. Dressler, B. S. Gaudi, T. Greene, O. Guyon, C. Hirata, J. Kalirai, N. J. Kasdin, B. Macintosh, W. Moos, S. Perlmutter, M. Postman, B. Rauscher, J. Rhodes, Y. Wang, D. Weinberg, D. Benford, M. Hudson, W. S. Jeong, Y. Mellier, W. Traub, T. Yamada, P. Capak, J. Colbert, D. Masters, M. Penny, D. Savransky, D. Stern, N. Zimmerman, R. Barry, L. Bartusek, K. Carpenter, E. Cheng, D. Content, F. Dekens, R. Demers, K. Grady, C. Jackson, G. Kuan, J. Kruk, M. Melton, B. Nemati, B. Parvin, I. Poberezhskiy, C. Peddie, J. Ruffa, J. K. Wallace, A. Whipple, E. Wollack, and F. Zhao. Wide-Field InfrarRed Survey Telescope-Astrophysics Focused Telescope Assets WFIRST-AFTA 2015 Report. *arXiv e-prints*, page arXiv:1503.03757, March 2015.

[155] R. Laureijs, J. Amiaux, S. Arduini, J. L. Augueres, J. Brinchmann, R. Cole, M. Cropper, C. Dabin, L. Duvet, A. Ealet, B. Garilli, P. Gondoin, L. Guzzo, J. Hoar, H. Hoekstra, R. Holmes, T. Kitching, T. Maciaszek, Y. Mellier, F. Pasian, W. Percival, J. Rhodes, G. Saavedra Criado, M. Sauvage, R. Scaramella, L. Valenziano, S. Warren, R. Bender, F. Castander, A. Cimatti, O. Le Fèvre, H. Kurki-Suonio, M. Levi, P. Lilje, G. Meylan, R. Nichol, K. Pedersen, V. Popa, R. Rebolo Lopez, H. W. Rix, H. Rottgering, W. Zeilinger, F. Grupp, P. Hudelot, R. Massey, M. Meneghetti,

L. Miller, S. Paltani, S. Paulin-Henriksson, S. Pires, C. Saxton, T. Schrabback, G. Seidel, J. Walsh, N. Aghanim, L. Amendola, J. Bartlett, C. Baccigalupi, J. P. Beaulieu, K. Benabed, J. G. Cuby, D. Elbaz, P. Fosalba, G. Gavazzi, A. Helmi, I. Hook, M. Irwin, J. P. Kneib, M. Kunz, F. Mannucci, L. Moscardini, C. Tao, R. Teyssier, J. Weller, G. Zamorani, M. R. Zapatero Osorio, O. Boulade, J. J. Foumond, A. Di Giorgio, P. Guttridge, A. James, M. Kemp, J. Martignac, A. Spencer, D. Walton, T. Blümchen, C. Bonoli, F. Bortoletto, C. Cerna, L. Corcione, C. Fabron, K. Jahnke, S. Ligori, F. Madrid, L. Martin, G. Morgante, T. Pamplona, E. Prieto, M. Riva, R. Toledo, M. Trifoglio, F. Zerbi, F. Abdalla, M. Douspis, C. Grenet, S. Borgani, R. Bouwens, F. Courbin, J. M. Delouis, P. Dubath, A. Fontana, M. Frailis, A. Grazian, J. Koppenhöfer, O. Mansutti, M. Melchior, M. Mignoli, J. Mohr, C. Neissner, K. Noddle, M. Poncet, M. Scodeggio, S. Serrano, N. Shane, J. L. Starck, C. Surace, A. Taylor, G. Verdoes-Kleijn, C. Vuerli, O. R. Williams, A. Zacchei, B. Altieri, I. Escudero Sanz, R. Kohley, T. Oosterbroek, P. Astier, D. Bacon, S. Bardelli, C. Baugh, F. Bellagamba, C. Benoist, D. Bianchi, A. Biviano, E. Branchini, C. Carbone, V. Cardone, D. Clements, S. Colombi, C. Conselice, G. Cresci, N. Deacon, J. Dunlop, C. Fedeli, F. Fontanot, P. Franzetti, C. Giocoli, J. Garcia-Bellido, J. Gow, A. Heavens, P. Hewett, C. Heymans, A. Holland, Z. Huang, O. Ilbert, B. Joachimi, E. Jennins, E. Kerins, A. Kiessling, D. Kirk, R. Kotak, O. Krause, O. Lahav, F. van Leeuwen, J. Lesgourgues, M. Lombardi, M. Magliocchetti, K. Maguire, E. Majerotto, R. Maoli, F. Marulli, S. Maurogordato, H. McCracken, R. McLure, A. Melchiorri, A. Merson, M. Moresco, M. Nonino, P. Norberg, J. Peacock, R. Pello, M. Penny, V. Pettorino, C. Di Porto, L. Pozzetti, C. Quercellini, M. Radovich, A. Rassat, N. Roche, S. Ronayette, E. Rossetti, B. Sartoris, P. Schneider, E. Semboloni, S. Serjeant, F. Simpson, C. Skordis, G. Smadja, S. Smartt, P. Spano, S. Spiro, M. Sullivan, A. Tilquin, R. Trotta, L. Verde, Y. Wang, G. Williger, G. Zhao, J. Zoubian, and E. Zucca. Euclid Definition Study Report. *arXiv e-prints*, page arXiv:1110.3193, October 2011.

[156] Cyril Creque-Sarbinowski and Marc Kamionkowski. Searching for decaying and annihilating dark matter with line intensity mapping. *Physical Review D*, 98(6), Sep 2018.

[157] Anthony R. Pullen, Olivier Doré , and Jamie Bock. INTENSITY MAPPING ACROSS COSMIC TIMES WITH THE ly LINE. *The Astrophysical Journal*, 786(2):111, apr 2014.

[158] David R. DeBoer, Aaron R. Parsons, James E. Aguirre, Paul Alexander, Zaki S. Ali, Adam P. Beardsley, Gianni Bernardi, Judd D. Bowman, Richard F. Bradley, Chris L. Carilli, and et al. Hydrogen epoch of reionization array (hera). *Publications of the Astronomical Society of the Pacific*, 129(974):045001, Mar 2017.

[159] Peng-Ju Wu and Xin Zhang. Prospects for measuring dark energy with 21 cm intensity mapping experiments, 2021.

[160] M. Righi, C. Hernández-Monteagudo, and R. A. Sunyaev. Carbon monoxide line emission as a cmb foreground: tomography of the star-forming universe with different spectral resolutions. *Astronomy Astrophysics*, 489(2):489–504, Jul 2008.

[161] Tony Y. Li, Risa H. Wechsler, Kiruthika Devaraj, and Sarah E. Church. Connecting co intensity mapping to molecular gas and star formation in the epoch of galaxy assembly. *The Astrophysical Journal*, 817(2):169, Jan 2016.

[162] José Fonseca, Marta B. Silva, Mário G. Santos, and Asantha Cooray. Cosmology with intensity mapping techniques using atomic and molecular lines. *Monthly Notices of the Royal Astronomical Society*, 464(2):1948–1965, Sep 2016.

[163] Hamsa Padmanabhan. Constraining the co intensity mapping power spectrum at intermediate redshifts. *Monthly Notices of the Royal Astronomical Society*, 475(2):1477–1484, Dec 2017.

[164] B. Yue, A. Ferrara, A. Pallottini, S. Gallerani, and L. Vallini. Intensity mapping of [cii] emission from early galaxies. *Monthly Notices of the Royal Astronomical Society*, 450(4):3829–3839, May 2015.

[165] Marta B. Silva, Mário G. santos, Asantha Cooray, and Yan Gong. Prospects for detecting cii emission during the epoch of reionization, 2015.

[166] Yan Gong, Asantha Cooray, Marta Silva, Mario G. Santos, James Bock, C. Matt Bradford, and Michael Zemcov. Intensity mapping of the [c ii] fine structure line during the epoch of reionization. *The Astrophysical Journal*, 745(1):49, Dec 2011.

[167] Marta B. Silva, Mario G. Santos, Yan Gong, Asantha Cooray, and James Bock. Intensity mapping of ly emission during the epoch of reionization. *The Astrophysical Journal*, 763(2):132, Jan 2013.

[168] Marta B. Silva, Saleem Zaroubi, Robin Kooistra, and Asantha Cooray. Tomographic intensity mapping versus galaxy surveys: Observing the universe in h-alpha emission with new generation instruments, 2017.

[169] Yan Gong, Asantha Cooray, Marta B. Silva, Michael Zemcov, Chang Feng, Mario G. Santos, Olivier Dore, and Xuelei Chen. Intensity Mapping of Hα, Hβ, [OII], and [OIII] Lines at z ¡ 5. , 835(2):273, February 2017.

[170] Garrett K. Keating, Daniel P. Marrone, Geoffrey C. Bower, Erik Leitch, John E. Carlstrom, and David R. DeBoer. COPSS II: The Molecular Gas Content of Ten Million Cubic Megaparsecs at Redshift z $\sim$ 3. , 830(1):34, October 2016.

[171] Garrett K. Keating, Daniel P. Marrone, Geoffrey C. Bower, and Ryan P. Keenan. An Intensity Mapping Detection of Aggregate CO Line Emission at 3 mm. , 901(2):141, October 2020.

[172] Patrick C. Breysse, Shengqi Yang, Rachel S. Somerville, Anthony R. Pullen, Gergö Popping, and Abhishek S. Maniyar. On estimating the cosmic molecular gas density from co line intensity mapping observations, 2021.

[173] Paul T. P. Ho, Pablo Altamirano, Chia-Hao Chang, Shu-Hao Chang, Su-Wei Chang, Chung-Cheng Chen, Ke-Jung Chen, Ming-Tang Chen, Chih-Chiang Han, West M. Ho, and et al. The yuan-tseh lee array for microwave background anisotropy. *The Astrophysical Journal*, 694(2):1610–1618, Mar 2009.

[174] A. T. Crites, J. J. Bock, C. M. Bradford, T. C. Chang, A. R. Cooray, L. Duband, Y. Gong, S. Hailey-Dunsheath, J. Hunacek, P. M. Koch, C. T. Li, R. C. O'Brient, T. Prouve, E. Shirokoff, M. B. Silva, Z. Staniszewski, B. Uzgil, and M. Zemcov. The TIME-Pilot intensity mapping experiment. In Wayne S. Holland and Jonas Zmuidzinas, editors, *Millimeter, Submillimeter, and Far-Infrared Detectors and Instrumentation for Astronomy VII*, volume 9153 of *Society of Photo-Optical Instrumentation Engineers (SPIE) Conference Series*, page 91531W, August 2014.

[175] P. Ade, M. Aravena, E. Barria, A. Beelen, A. Benoit, M. Béthermin, J. Bounmy, O. Bourrion, G. Bres, and et al. A wide field-of-view low-resolution spectrometer at apex: Instrument design and scientific forecast. *Astronomy Astrophysics*, 642:A60, Oct 2020.

[176] K. S. Karkare, P. S. Barry, C. M. Bradford, S. Chapman, S. Doyle, J. Glenn, S. Gordon, S. Hailey-Dunsheath, R. M. J. Janssen, A. Kovács, and et al. Full-array noise performance of deployment-grade superspec mm-wave on-chip spectrometers. *Journal of Low Temperature Physics*, 199(3-4):849–857, Feb 2020.

[177] Miguel Zumalacárregui, Emilio Bellini, Ignacy Sawicki, Julien Lesgourgues, and Pedro G. Ferreira. hi class: Horndeski in the cosmic linear anisotropy solving system. *Journal of Cosmology and Astroparticle Physics*, 2017(08):019–019, Aug 2017.

[178] Emilio Bellini, Ignacy Sawicki, and Miguel Zumalacárregui. hi class background evolution, initial conditions and approximation schemes. *Journal of Cosmology and Astroparticle Physics*, 2020(02):008–008, Feb 2020.

[179] Jacques Delabrouille, Maximilian H. Abitbol, Nabila Aghanim, Yacine Ali-Haimoud, David Alonso, Marcelo Alvarez, Anthony J. Banday, James G. Bartlett, Jochem Baselmans, Kaustuv Basu, Nicholas Battaglia, Jose Ramon Bermejo Climent, Jose L. Bernal, Matthieu Béthermin, Boris Bolliet, Matteo Bonato, François R. Bouchet, Patrick C. Breysse, Carlo Burigana, Zhen-Yi Cai, Jens Chluba, Eugene Churazov, Helmut Dannerbauer, Paolo De Bernardis, Gianfranco De Zotti, Eleonora Di Valentino, Emanuela Dimastrogiovanni, Akira Endo, Jens Erler, Simone Ferraro, Fabio Finelli, Dale Fixsen, Shaul Hanany, Luke Hart, Carlos Hernandez-Monteagudo, J. Colin Hill, Selim C. Hotinli, Kenichi Karatsu, Kirit Karkare, Garrett K. Keating, Ildar Khabibullin, Alan Kogut, Kazunori Kohri, Ely D. Kovetz, Guilaine Lagache, Julien Lesgourgues, Mathew Madhavacheril, Bruno Maffei, Nazzareno Mandolesi, Carlos Martins, Silvia Masi, John Mather, Jean-Baptiste Melin, Azadeh Moradinezhad Dizgah, Tony Mroczkowski, Suvodip Mukherjee, Daisuke Nagai, Mattia Negrello, Nathalie Palanque-Delabrouille, Daniela Paoletti, Subodh P. Patil, Francesco Piacentini, Srinivasan Raghunathan, Andrea Ravenni, Mathieu Remazeilles, Vincent Revéret, Louis Rodriguez, Aditya Rotti, Jose-Alberto Rubino Martin, Jack Sayers, Douglas Scott, Joseph Silk, Marta Silva, Tarun Souradeep, Naonori Sugiyama, Rashid Sunyaev, Eric R. Switzer, Andrea Tartari, Tiziana Trombetti, and Inigo Zubeldia. Microwave Spectro-Polarimetry of Matter and Radiation across Space and Time. *arXiv e-prints*, page arXiv:1909.01591, September 2019.

[180] José Luis Bernal and Ely D. Kovetz. Line-intensity mapping: Theory review, 2022.

[181] A. J. S. Hamilton. Linear redshift distortions: A review. In *Astrophysics and Space Science Library*, pages 185–275. Springer Netherlands, 1998.

[182] Dongwoo T. Chung, Marco P. Viero, Sarah E. Church, Risa H. Wechsler, Marcelo A. Alvarez, J. Richard Bond, Patrick C. Breysse, Kieran A. Cleary, Hans K. Eriksen, Marie K. Foss, and et al. Cross-correlating carbon monoxide line-intensity maps with spectroscopic and photometric galaxy surveys. *The Astrophysical Journal*, 872(2):186, Feb 2019.

[183] Atsushi Taruya, Takahiro Nishimichi, and Shun Saito. Baryon acoustic oscillations in 2d: Modeling redshift-space power spectrum from perturbation theory. *Physical Review D*, 82(6), sep 2010.

[184] BICEP2 Collaboration, Keck Array Collaboration, SPIDER Collaboration, P. A. R. Ade, R. W. Aikin, M. Amiri, D. Barkats, S. J. Benton, C. A. Bischoff, J. J. Bock, J. A. Bonetti, J. A. Brevik, I. Buder, E. Bullock, G. Chattopadhyay, G. Davis, P. K. Day, C. D. Dowell, L. Duband, J. P. Filippini, S. Fliescher, S. R. Golwala, M. Halpern, M. Hasselfield, S. R. Hildebrandt, G. C. Hilton, V. Hristov, H. Hui, K. D. Irwin, W. C. Jones, K. S. Karkare, J. P. Kaufman, B. G. Keating, S. Kefeli, S. A. Kernasovskiy, J. M. Kovac, C. L. Kuo, H. G. LeDuc, E. M. Leitch, N. Llombart, M. Lueker, P. Mason, K. Megerian, L. Moncelsi, C. B. Netterfield, H. T. Nguyen, R. O'Brient, IV Ogburn, R. W., A. Orlando, C. Pryke, A. S. Rahlin, C. D. Reintsema, S. Richter, M. C. Runyan, R. Schwarz, C. D. Sheehy, Z. K. Staniszewski, R. V. Sudiwala, G. P. Teply, J. E. Tolan, A. Trangsrud, R. S. Tucker, A. D. Turner, A. G. Vieregg, A. Weber, D. V. Wiebe, P. Wilson, C. L. Wong, K. W. Yoon, and J. Zmuidzinas. Antenna-coupled TES Bolometers Used in BICEP2, Keck Array, and Spider. , 812(2):176, October 2015.

[185] A. Nadolski, J. D. Vieira, J. A. Sobrin, A. M. Kofman, P. A. R. Ade, Z. Ahmed, A. J. Anderson, J. S. Avva, R. Basu Thakur, A. N. Bender, B. A. Benson, L. Bryant, J. E. Carlstrom, F. W. Carter, T. W. Cecil, C. L. Chang, J. R. Cheshire, G. E. Chesmore, J. F. Cliche, A. Cukierman, T. de Haan, M. Dierickx, J. Ding, D. Dutcher, W. Everett, J. Farwick, K. R. Ferguson, L. Florez, A. Foster, J. Fu, J. Gallicchio, A. E. Gambrel, R. W. Gardner, J. C. Groh, S. Guns, R. Guyser, N. W. Halverson, A. H. Harke-Hosemann, N. L. Harrington, R. J. Harris, J. W. Henning, W. L. Holzapfel, D. Howe, N. Huang, K. D. Irwin, O. Jeong, M. Jonas, A. Jones, M. Korman, J. Kovac, D. L. Kubik, S. Kuhlmann, C. L. Kuo, A. T. Lee, A. E. Lowitz, J. McMahon, J. Meier, S. S. Meyer, D. Michalik, J. Montgomery, T. Natoli, H. Nguyen, G. I. Noble, V. Novosad, S. Padin, Z. Pan, P. Paschos, J. Pearson, C. M. Posada, W. Quan, A. Rahlin, D. Riebel, J. E. Ruhl, J. T. Sayre, E. Shirokoff, G. Smecher, A. A. Stark, J. Stephen, K. T. Story, A. Suzuki, C. Tandoi, K. L. Thompson, C. Tucker, K. Vanderlinde, G. Wang, N. Whitehorn, V. Yefremenko, K. W. Yoon, and M. R. Young. Broadband, millimeter-wave antireflection coatings for large-format, cryogenic aluminum oxide optics. , 59(10):3285, April 2020.

[186] E. Shirokoff, P. S. Barry, C. M. Bradford, G. Chattopadhyay, P. Day, S. Doyle, S. Hailey-Dunsheath, M. I. Hollister, A. Kovács, C. McKenney, H. G. Leduc, N. Llombart, D. P. Marrone, P. Mauskopf, R. O'Brient, S. Padin, T. Reck, L. J. Swenson,

and J. Zmuidzinas. MKID development for SuperSpec: an on-chip, mm-wave, filter-bank spectrometer. In Wayne S. Holland and Jonas Zmuidzinas, editors, *Millimeter, Submillimeter, and Far-Infrared Detectors and Instrumentation for Astronomy VI*, volume 8452 of *Society of Photo-Optical Instrumentation Engineers (SPIE) Conference Series*, page 84520R, September 2012.

[187] Kevork N. Abazajian, Peter Adshead, Zeeshan Ahmed, Steven W. Allen, David Alonso, Kam S. Arnold, Carlo Baccigalupi, James G. Bartlett, Nicholas Battaglia, Bradford A. Benson, Colin A. Bischoff, Julian Borrill, Victor Buza, Erminia Calabrese, Robert Caldwell, John E. Carlstrom, Clarence L. Chang, Thomas M. Crawford, Francis-Yan Cyr-Racine, Francesco De Bernardis, Tijmen de Haan, Sperello di Serego Alighieri, Joanna Dunkley, Cora Dvorkin, Josquin Errard, Giulio Fabbian, Stephen Feeney, Simone Ferraro, Jeffrey P. Filippini, Raphael Flauger, George M. Fuller, Vera Gluscevic, Daniel Green, Daniel Grin, Evan Grohs, Jason W. Henning, J. Colin Hill, Renee Hlozek, Gilbert Holder, William Holzapfel, Wayne Hu, Kevin M. Huffenberger, Reijo Keskitalo, Lloyd Knox, Arthur Kosowsky, John Kovac, Ely D. Kovetz, Chao-Lin Kuo, Akito Kusaka, Maude Le Jeune, Adrian T. Lee, Marc Lilley, Marilena Loverde, Mathew S. Madhavacheril, Adam Mantz, David J. E. Marsh, Jeffrey McMahon, Pieter Daniel Meerburg, Joel Meyers, Amber D. Miller, Julian B. Munoz, Ho Nam Nguyen, Michael D. Niemack, Marco Peloso, Julien Peloton, Levon Pogosian, Clement Pryke, Marco Raveri, Christian L. Reichardt, Graca Rocha, Aditya Rotti, Emmanuel Schaan, Marcel M. Schmittfull, Douglas Scott, Neelima Sehgal, Sarah Shandera, Blake D. Sherwin, Tristan L. Smith, Lorenzo Sorbo, Glenn D. Starkman, Kyle T. Story, Alexander van Engelen, Joaquin D. Vieira, Scott Watson, Nathan Whitehorn, and W. L. Kimmy Wu. CMB-S4 Science Book, First Edition. *arXiv e-prints*, page arXiv:1610.02743, October 2016.

[188] P. A. R. Ade, Z. Ahmed, R. W. Aikin, K. D. Alexander, D. Barkats, S. J. Benton, C. A. Bischoff, J. J. Bock, R. Bowens-Rubin, J. A. Brevik, I. Buder, E. Bullock, V. Buza, J. Connors, J. Cornelison, B. P. Crill, M. Crumrine, M. Dierickx, L. Duband, C. Dvorkin, J. P. Filippini, S. Fliescher, J. Grayson, G. Hall, M. Halpern, S. Harrison, S. R. Hildebrandt, G. C. Hilton, H. Hui, K. D. Irwin, J. Kang, K. S. Karkare, E. Karpel, J. P. Kaufman, B. G. Keating, S. Kefeli, S. A. Kernasovskiy, J. M. Kovac, C. L. Kuo, N. A. Larsen, K. Lau, E. M. Leitch, M. Lueker, K. G. Megerian, L. Moncelsi, T. Namikawa, C. B. Netterfield, H. T. Nguyen, R. O'Brient, R. W. Ogburn, S. Palladino, C. Pryke, B. Racine, S. Richter, A. Schillaci, R. Schwarz, C. D. Sheehy, A. Soliman, T. St. Germaine, Z. K. Staniszewski, B. Steinbach, R. V. Sudiwala, G. P. Teply, K. L. Thompson, J. E. Tolan, C. Tucker, A. D. Turner, C. Umiltà, A. G. Vieregg, A. Wandui, A. C. Weber, D. V. Wiebe, J. Willmert, C. L. Wong, W. L. K. Wu, H. Yang, K. W. Yoon, and C. Zhang and. Constraints on primordial gravitational waves using planck , wmap, and new bicep2/keck observations through the 2015 season. *Physical Review Letters*, 121(22), nov 2018.

[189] Patrick C. Breysse, Ely D. Kovetz, and Marc Kamionkowski. Masking line foregrounds in intensity-mapping surveys. , 452(4):3408–3418, October 2015.

[190] G. Sun, L. Moncelsi, M. P. Viero, M. B. Silva, J. Bock, C. M. Bradford, T. C. Chang,

Y. T. Cheng, A. R. Cooray, A. Crites, S. Hailey-Dunsheath, B. Uzgil, J. R. Hunacek, and M. Zemcov. A Foreground Masking Strategy for [C II] Intensity Mapping Experiments Using Galaxies Selected by Stellar Mass and Redshift. , 856(2):107, April 2018.

[191] Andreas Albrecht, Gary Bernstein, Robert Cahn, Wendy L. Freedman, Jacqueline Hewitt, Wayne Hu, John Huth, Marc Kamionkowski, Edward W. Kolb, Lloyd Knox, John C. Mather, Suzanne Staggs, and Nicholas B. Suntzeff. Report of the Dark Energy Task Force. *arXiv e-prints*, pages astro–ph/0609591, September 2006.

[192] R. E. Smith, J. A. Peacock, A. Jenkins, S. D. M. White, C. S. Frenk, F. R. Pearce, P. A. Thomas, G. Efstathiou, and H. M. P. Couchman. Stable clustering, the halo model and non-linear cosmological power spectra. , 341(4):1311–1332, June 2003.

[193] J. Einasto, L. J. Liivamägi, I. Suhhonenko, and M. Einasto. The biasing phenomenon. , 630:A62, October 2019.

[194] L. Samushia, W. J. Percival, and A. Raccanelli. Interpreting large-scale redshift-space distortion measurements. *Monthly Notices of the Royal Astronomical Society*, 420(3):2102–2119, jan 2012.

[195] DESI Collaboration, Amir Aghamousa, Jessica Aguilar, Steve Ahlen, Shadab Alam, Lori E. Allen, Carlos Allende Prieto, James Annis, Stephen Bailey, Christophe Balland, Otger Ballester, Charles Baltay, Lucas Beaufore, Chris Bebek, Timothy C. Beers, Eric F. Bell, José Luis Bernal, Robert Besuner, Florian Beutler, Chris Blake, Hannes Bleuler, Michael Blomqvist, Robert Blum, Adam S. Bolton, Cesar Briceno, David Brooks, Joel R. Brownstein, Elizabeth Buckley-Geer, Angela Burden, Etienne Burtin, Nicolas G. Busca, Robert N. Cahn, Yan-Chuan Cai, Laia Cardiel-Sas, Raymond G. Carlberg, Pierre-Henri Carton, Ricard Casas, Francisco J. Castander, Jorge L. Cervantes-Cota, Todd M. Claybaugh, Madeline Close, Carl T. Coker, Shaun Cole, Johan Comparat, Andrew P. Cooper, M. C. Cousinou, Martin Crocce, Jean-Gabriel Cuby, Daniel P. Cunningham, Tamara M. Davis, Kyle S. Dawson, Axel de la Macorra, Juan De Vicente, Timothée Delubac, Mark Derwent, Arjun Dey, Govinda Dhungana, Zhejie Ding, Peter Doel, Yutong T. Duan, Anne Ealet, Jerry Edelstein, Sarah Eftekharzadeh, Daniel J. Eisenstein, Ann Elliott, Stéphanie Escoffier, Matthew Evatt, Parker Fagrelius, Xiaohui Fan, Kevin Fanning, Arya Farahi, Jay Farihi, Ginevra Favole, Yu Feng, Enrique Fernandez, Joseph R. Findlay, Douglas P. Finkbeiner, Michael J. Fitzpatrick, Brenna Flaugher, Samuel Flender, Andreu Font-Ribera, Jaime E. Forero-Romero, Pablo Fosalba, Carlos S. Frenk, Michele Fumagalli, Boris T. Gaensicke, Giuseppe Gallo, Juan Garcia-Bellido, Enrique Gaztanaga, Nicola Pietro Gentile Fusillo, Terry Gerard, Irena Gershkovich, Tommaso Giannantonio, Denis Gillet, Guillermo Gonzalez-de-Rivera, Violeta Gonzalez-Perez, Shelby Gott, Or Graur, Gaston Gutierrez, Julien Guy, Salman Habib, Henry Heetderks, Ian Heetderks, Katrin Heitmann, Wojciech A. Hellwing, David A. Herrera, Shirley Ho, Stephen Holland, Klaus Honscheid, Eric Huff, Timothy A. Hutchinson, Dragan Huterer, Ho Seong Hwang, Joseph Maria Illa Laguna, Yuzo Ishikawa, Dianna Jacobs, Niall Jeffrey, Patrick Jelinsky, Elise Jennings, Linhua Jiang, Jorge Jimenez, Jennifer

Johnson, Richard Joyce, Eric Jullo, Stéphanie Juneau, Sami Kama, Armin Karcher, Sonia Karkar, Robert Kehoe, Noble Kennamer, Stephen Kent, Martin Kilbinger, Alex G. Kim, David Kirkby, Theodore Kisner, Ellie Kitanidis, Jean-Paul Kneib, Sergey Koposov, Eve Kovacs, Kazuya Koyama, Anthony Kremin, Richard Kron, Luzius Kronig, Andrea Kueter-Young, Cedric G. Lacey, Robin Lafever, Ofer Lahav, Andrew Lambert, Michael Lampton, Martin Landriau, Dustin Lang, Tod R. Lauer, Jean-Marc Le Goff, Laurent Le Guillou, Auguste Le Van Suu, Jae Hyeon Lee, Su-Jeong Lee, Daniela Leitner, Michael Lesser, Michael E. Levi, Benjamin L'Huillier, Baojiu Li, Ming Liang, Huan Lin, Eric Linder, Sarah R. Loebman, Zarija Lukić, Jun Ma, Niall MacCrann, Christophe Magneville, Laleh Makarem, Marc Manera, Christopher J. Manser, Robert Marshall, Paul Martini, Richard Massey, Thomas Matheson, Jeremy McCauley, Patrick McDonald, Ian D. McGreer, Aaron Meisner, Nigel Metcalfe, Timothy N. Miller, Ramon Miquel, John Moustakas, Adam Myers, Milind Naik, Jeffrey A. Newman, Robert C. Nichol, Andrina Nicola, Luiz Nicolati da Costa, Jundan Nie, Gustavo Niz, Peder Norberg, Brian Nord, Dara Norman, Peter Nugent, Thomas O'Brien, Minji Oh, Knut A. G. Olsen, Cristobal Padilla, Hamsa Padmanabhan, Nikhil Padmanabhan, Nathalie Palanque-Delabrouille, Antonella Palmese, Daniel Pappalardo, Isabelle Pâris, Changbom Park, Anna Patej, John A. Peacock, Hiranya V. Peiris, Xiyan Peng, Will J. Percival, Sandrine Perruchot, Matthew M. Pieri, Richard Pogge, Jennifer E. Pollack, Claire Poppett, Francisco Prada, Abhishek Prakash, Ronald G. Probst, David Rabinowitz, Anand Raichoor, Chang Hee Ree, Alexandre Refregier, Xavier Regal, Beth Reid, Kevin Reil, Mehdi Rezaie, Constance M. Rockosi, Natalie Roe, Samuel Ronayette, Aaron Roodman, Ashley J. Ross, Nicholas P. Ross, Graziano Rossi, Eduardo Rozo, Vanina Ruhlmann-Kleider, Eli S. Rykoff, Cristiano Sabiu, Lado Samushia, Eusebio Sanchez, Javier Sanchez, David J. Schlegel, Michael Schneider, Michael Schubnell, Aurélia Secroun, Uros Seljak, Hee-Jong Seo, Santiago Serrano, Arman Shafieloo, Huanyuan Shan, Ray Sharples, Michael J. Sholl, William V. Shourt, Joseph H. Silber, David R. Silva, Martin M. Sirk, Anze Slosar, Alex Smith, George F. Smoot, Debopam Som, Yong-Seon Song, David Sprayberry, Ryan Staten, Andy Stefanik, Gregory Tarle, Suk Sien Tie, Jeremy L. Tinker, Rita Tojeiro, Francisco Valdes, Octavio Valenzuela, Monica Valluri, Mariana Vargas-Magana, Licia Verde, Alistair R. Walker, Jiali Wang, Yuting Wang, Benjamin A. Weaver, Curtis Weaverdyck, Risa H. Wechsler, David H. Weinberg, Martin White, Qian Yang, Christophe Yeche, Tianmeng Zhang, Gong-Bo Zhao, Yi Zheng, Xu Zhou, Zhimin Zhou, Yaling Zhu, Hu Zou, and Ying Zu. The DESI Experiment Part I: Science,Targeting, and Survey Design. *arXiv e-prints*, page arXiv:1611.00036, October 2016.

[196] Abhishek S. Maniyar, Emmanuel Schaan, and Anthony R. Pullen. New probe of the high-redshift Universe: Nulling CMB lensing with interloper-free line intensity mapping pair lensing. , 105(8):083509, April 2022.

[197] A. Pourtsidou and R. Benton Metcalf. Gravitational lensing of cosmological 21 cm emission. , 448(3):2368–2383, April 2015.

[198] Rachel S. Somerville and Joel R. Primack. Semi-analytic modelling of galaxy formation: the local Universe. , 310(4):1087–1110, December 1999.

[199] Karen P. Olsen, Thomas R. Greve, Desika Narayanan, Robert Thompson, Sune Toft, and Christian Brinch. Simulator of Galaxy Millimeter/Submillimeter Emission (SíGAME): The [C ii]-SFR Relationship of Massive z = 2 Main Sequence Galaxies. , 814(1):76, November 2015.

[200] Scott Paine. The am atmospheric model (12.0)., 2022.